
Regimes of photospheric radius expansion driven by high luminosities in Type I X-ray bursts

Simon Guichandut

Department of Physics
McGill University
Montreal, Quebec
January 15, 2021

A thesis submitted to McGill University in partial fulfillment
of the requirements of the degree of Master of Science

© Simon Guichandut 2020

Acknowledgements

The work presented in this thesis has been performed in the context of a Master's degree, partly funded by a scholarship from the Fonds de recherche du Québec – Nature et Technologies (FRQNT). Thank you to my advisor, Andrew Cumming, for giving me this opportunity and introducing me to this fascinating research field, for guidance throughout this project and help in the preparation of this manuscript. Thank you to J. R. Fuentes and Vanessa Graber for many helpful discussions and advice over the last two years. Thank you to Nevin Weinberg, Anna Watts, Laurens Keek and others for useful conversations during a scientific meeting in Leiden in June 2019. Thank you to Zhaosheng Li and Michael Zamfir for sharing results of preliminary calculations. Finally, thank you the professors and coordinators of the McGill Space Institute for fostering a welcoming and motivating research environment.

Merci à ma mère, sans qui je ne serais pas ici, et à Julien, Marie Anne, Laurence, Laura et au reste de ma famille pour leur soutien et encouragements au cours des derniers mois.

Abstract

Type I X-ray bursts are thermonuclear runaway events occurring on the surface of accreting neutron stars that result in bright X-ray flashes. These events can produce luminosities so high that hydrostatic balance is lifted and the star's photosphere expands drastically, from tens to thousands of kilometres. Using steady-state equations of general relativistic radiation hydrodynamics, we calculate solutions of expanded, hydrostatic, envelopes as well as super-Eddington winds. We construct a grid of models which can be used to interpret X-ray observations of bursts, and as an outer boundary for time-dependent simulations of the neutron star burning layer. Our results show that observations of small photospheres likely point to static envelopes rather than winds, that the neutron star radius can easily be over-estimated when deduced from burst spectra, and that steady-state models in general are not applicable in the early stages of the burst. The theoretical framework that we derive and numerical methods that we propose can also be used in other astrophysical applications, such as classical novae.

Abrégé

Les sursauts rayons X de type I sont des réactions thermonucléaires prenant place sur la surface d'étoiles à neutrons produisant de puissants éclats lumineux. Ces événements peuvent produire des luminosités si grandes que l'équilibre hydrostatique à la surface de l'étoile est rompu, provoquant une expansion de sa photosphère jusqu'à des dizaines, voire des milliers de kilomètres. En utilisant des équations stationnaires d'hydrodynamique radiative relativiste, nous calculons des solutions d'enveloppes hydrostatiques étendues et de vents super-Eddington. Nous construisons une grille de modèles qui peuvent être utilisés pour interpréter des observations de sursauts rayons X, ainsi qu'en tant que condition frontière pour des simulations de l'évolution temporelle de la couche enflammée de l'étoile à neutrons. Nos résultats démontrent que les observations de petites photosphères suggèrent la présence d'enveloppes statiques plutôt que de vents, que le rayon de l'étoile peut facilement être surestimé lorsque déterminé à partir du spectre des sursauts rayons X, et que les modèles stationnaires en général ne sont pas appropriés pour décrire l'évolution initiale du sursaut. Le cadre théorique que nous dérivons et les méthodes numériques que nous proposons peuvent également être utilisés pour d'autres problèmes en astrophysique, tels que les novæ.

Contents

Acknowledgements	i
Abstract	ii
Abrégé	iii
1 Introduction	1
1.1 Neutron Stars	1
1.2 Type I X-ray bursts	2
1.3 Open questions	4
1.4 Basic theory and previous theoretical work	9
1.5 Outline	12
2 Prior on radiation hydrodynamics	14
2.1 General relativity	15
2.2 Stress-energy tensors	17
2.3 Hydrodynamics equations	21
2.4 Equation of state	25
2.5 Structure equations	27
3 Winds	31
3.1 The critical point	32
3.2 Numerical integration and boundary conditions	33

3.3	Root-finding	37
3.4	Dependence of the wind models on \dot{M}	41
3.5	Photospheric radii and spectral shifts	44
4	Expanded envelopes	48
4.1	Numerical integration and boundary conditions	50
4.2	Dependence of the envelope models on r_{ph}	54
4.3	Compact envelopes and touchdown radius	58
5	The stationary solution space	61
5.1	Profiles	61
5.2	Base luminosity	64
5.3	On the definition of the photosphere	69
6	Summary and conclusions	71
Appendices		
Appendix A Index of constants, variables and parameters		76
Appendix B Wind parameter spaces		79
Appendix C Analytical Newtonian envelopes		82
Appendix D Additional derivations		84
References		97

List of Figures

1.2.1 Type I X-ray burst light curve	3
1.2.2 <i>NICER</i> PRE burst light curve	5
1.3.1 Burst spectra fit residuals showing spectral lines	7
1.5.1 Diagram of PRE burst expansion regimes	13
3.3.1 B.C. errors on the $\log \dot{M} = 18.5$ wind parameter space	38
3.3.2 Roots of wind models	40
3.3.3 Velocity at infinity of wind models	41
3.4.1 Wind radial profiles	42
3.4.2 Wind local to critical luminosity ratios	43
3.4.3 Wind temperature-density profiles	45
3.5.1 Photospheres of winds in different neutron stars	46
3.5.2 Wind spectral shifts	47
4.1.1 Demonstration of the numerical method for envelopes	53
4.2.1 Envelope radial profiles	55
4.2.2 Envelope temperature-density profiles	56
4.2.3 Envelope radiative to adiabatic gradient ratios	57
4.2.4 Envelope luminosities	58
4.3.1 Touchdown radius based on the observables	60
5.1.1 Radial profiles of winds and envelopes	62
5.1.2 Temperature-density profiles of winds and envelopes	63
5.2.1 Solution space for the base luminosity	65

5.2.2 Mass stored in envelopes and winds	68
5.3.1 Optical depth parameter in the envelope models	70

List of Tables

1.1 Previous work on burst super-Eddington winds	12
3.1 Locations and conditions in the wind model	37
6.1 Future work	74
A.1 Physical constants	76
A.2 Variables	77
A.3 Parameters	78

Chapter 1

Introduction

1.1 Neutron Stars

Neutron stars are some of the most interesting and exotic objects in the Universe. With a mass slightly larger than that of the Sun packed into the size of a city, they are made up of matter denser than anything that can be found on Earth. As such, they provide a unique way to probe dense matter physics, even from thousands of light years away. Indeed, these stars have been observed in both radio and X-rays since the 1960's [Hewish et al., 1968, Shklovsky, 1967]. These observations have led to constraints on parameters such as surface temperature, atmospheric composition and spin frequency of these stars. However, much is still not well understood about neutron stars. Most notably, the dense matter equation of state is still unknown. A lot of work, both theoretical and observational, is dedicated to finding masses and radii of neutron stars in order to constrain this equation of state.

We now live in a golden age of neutron star astronomy, with the detection of double neutron star mergers with gravitational waves [Abbott et al., 2017], the launch of modern X-ray observatories designed to study neutron stars and, as a result, the first reliable neutron star radius measurements [Gendreau and Arzoumanian, 2017, Miller et al., 2019]. On the theoretical

side, there is still room for improvement in the physical models that describe various phenomena happening in neutron stars. One astrophysical system where we can study neutron stars are X-ray binaries, where a neutron star accretes from a companion star. Accreted H/He fuel periodically burns on the neutron star surface, making the neutron star very bright, and giving an opportunity to study the neutron star directly. These systems are the focus of this thesis, where we study the ejection of matter in bright thermonuclear bursts.

1.2 Type I X-ray bursts

Neutron stars are sometimes found in binary systems where they orbit another star with a period of hours to days [Lewin et al., 1993]. In this configuration, when the companion star begins expanding as it goes through its main sequence evolution, it is possible for its outer layers to escape its surface and funnel onto the surface of the neutron star in a process called *accretion*. As matter builds up on top of the neutron star crust, it eventually reaches a critical pressure where helium quickly fuses via the triple- α process. The star cannot compensate for this sudden release of heat by cooling, thus creating a thermonuclear runaway, which quickly spreads through the accreted matter ocean and burns most of the hydrogen and helium. This event results in the neutron star shining brightly in X-rays for seconds to minutes. This X-ray flash is referred to as a *Type I X-ray burst*, or *burst* for short. A typical burst light curve is shown in Fig. 1.2.1.

Some bursts reach luminosities so high that radiation pressure starts to push some of the accreted material outward, making the star temporarily appear bigger and colder due to the expansion of the photosphere. These *photospheric radius expansion* (PRE) bursts are observed as near blackbodies with a temperature of ~ 1 keV at the burst peak, and $\sim 1 - 5$ keV when the photosphere touches back down to the surface. The light curve shown in

the top panel of Fig. 1.2.1 is from such a PRE burst, with the bottom two panels showing best fit values for the blackbody temperature and emitting radius. The PRE phase of the burst is marked by the concurrent drop in temperature and jump in radius.

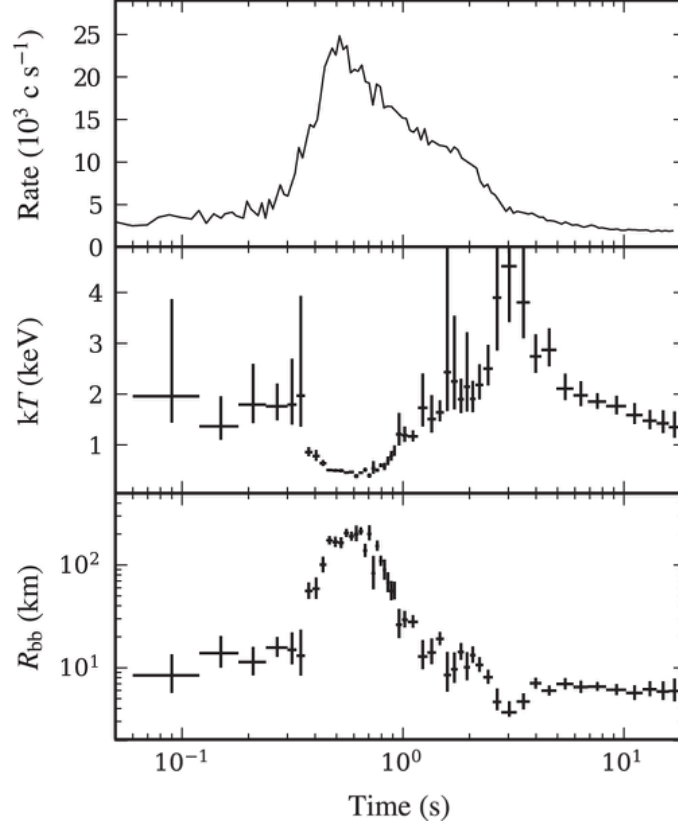


Figure 1.2.1 – Light curve (top panel) and blackbody fits (middle and bottom panels) from a Type I X-ray burst in the low-mass X-ray binary 4U 1820-30, observed by *NICER* in august 2017. Adapted from Keek et al. [2018].

A large number of type I X-ray bursts have been observed from a multitude of systems since their discovery in 1976 [Grindlay et al., 1976]. More than a thousand bursts have been observed by the Rossi X-ray Timing Explorer (RXTE) alone [Galloway et al., 2008]. In this catalogue, 35 of the 48 bursting sources have had PRE bursts observed. An intriguing puzzle

is the fact that there are seemingly two categories of radius expansion. In most cases, the photosphere only expands to tens of kilometres above the stellar surface. In the rare *superexpansion* bursts, the photosphere surpasses a thousand kilometres in radius [in 't Zand and Weinberg, 2010]. It has been suggested that the second case could be caused by the wind-driven ejection of a geometrically thin shell which remains optically thick until it has expanded and cooled enough at large radii. This raises questions about the timescales of the expansion, and the manner in which the initially hydrostatic envelope can transition into a fully outflowing wind.

The burst shown in Fig. 1.2.1, which occurred in August 2017 in the low-mass X-ray binary 4U 1820-30, marked an important moment in the field of Type I X-ray bursts as it was the first PRE burst observed by the *Neutron Star Interior Composition Explorer* (*NICER*), an X-ray observatory on the International Space Station that was launched in 2017 [Gendreau and Arzoumanian, 2017]. *NICER*'s principal objective is to constrain the dense matter equation of state by obtaining mass and radius measurements of neutron stars. To accomplish this goal, *NICER* needs a wide spectral range, especially in the soft (<1 keV) band. This makes *NICER* the best tool yet to observe PRE bursts, as it can track the whole evolution of the photospheric radius [Keek et al., 2018]. Indeed, previous X-ray instruments that had no soft response would observe an artificial dip in total luminosity, as the blackbody temperature would exit their spectral range. This contrast between *NICER* and previous telescopes can be seen in figure 1.2.2.

1.3 Open questions

There has been, in the past few years, a renewed interest in theoretical models of the outflows driving the PRE phase, marked for example by the works of Yu and Weinberg [2018] and Herrera et al. [2020]. These have certainly been motivated in large part by the arrival of *NICER*, and the opportunity

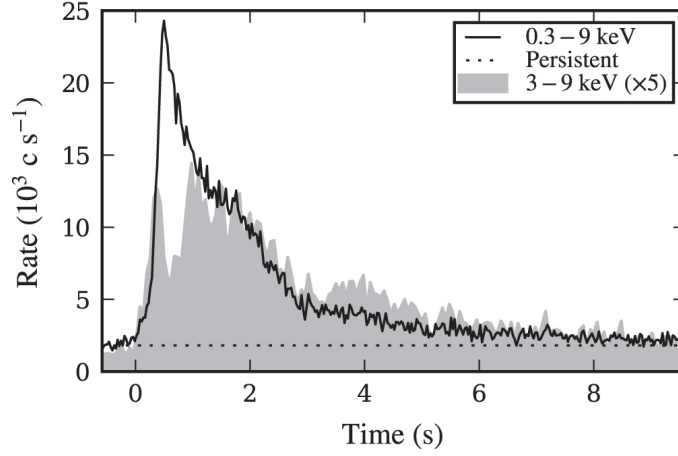


Figure 1.2.2 – Light curve from a Type I X-ray burst in 4U 1820-30 considering different spectral ranges of observation. The solid line shows the count rate in the *NICER* spectral range, while the gray shaded area shows the count rate (scaled up by a factor of 5) for instruments with no soft X-ray response. The dotted line shows the count rate for the persistent (pre-burst) emission. Adapted from Keek et al. [2018].

for theorists and observers to work together to answer a number of open questions regarding Type I X-ray bursts. We highlight two of these major open questions here.

1. Can heavy elements produced in the nuclear reaction networks at the onset of the burst be ejected during the subsequent outflows?

Type I X-ray bursts are a unique environment for nuclear burning, as helium is being burned with a large number of protons from ionized hydrogen present. Via the rapid proton capture (rp) process, many heavy elements, even far beyond the iron group, are produced in a short time frame [Schatz et al., 1999]. There has recently been mounting observational evidence, in the form of spectral edges and lines within Type I X-ray burst spectra [in 't Zand and Weinberg, 2010, Kajava et al., 2017, Strohmayer et al., 2019], that heavy elements such as iron and nickel are present at the photosphere during

the expansion phase. This suggests that nuclear ashes are somehow dredged up, possibly via convection, and subsequently lifted up during the expansion. If a wind is driving the expansion, it is possible that these heavy elements are completely ejected from the star and deposited into the accretion disk, or even into the interstellar medium.

The conditions and manner in which these ashes can be lifted is not well understood, and neither is the expected observational signature of heavy elements if they are truly present in the outflow. However, recent results from *NICER* data and presented in Strohmayer et al. [2019] show some promise for the latter. In the days following the burst from 4U 1820-30, shown in Fig. 1.2.1 and 1.2.2, three more bursts exhibiting a PRE phase were observed. Among these four, blackbody fits of the spectra revealed that two of the bursts had expansion phases with a photosphere of ~ 100 km, while the other two had weaker expansion, with a photosphere of ~ 75 km. By co-adding spectra of the bursts within each pair and fitting these with an absorbed blackbody model, it became clear that the bursts had spectral lines in their spectra, of both emission and absorption nature. This can be seen in Fig. 1.3.1. Further, the spectral shift between the two pairs is the same for each line, with weaker burst lines appearing *redshifted* compared to the strong bursts by a factor of 1.046. This is consistent with the lines being produced in a wind. Indeed, the lines in the weaker bursts should be produced closer to the neutron star, and thus have stronger redshift. On top of this effect, wind models, which we will discuss in the next section, show that stronger bursts have larger wind velocities, which means the lines are more *blueshifted*. Strohmayer et al. [2019] argue that both of these effects work together to create the spectral shifts seen in Fig. 1.3.1. While this represents a convincing argument for the existence of both burst-driven winds and heavy element ejection, it suffers from a lack of theoretical models of such winds, especially ones which include a heterogeneous gas composition with heavy materials, which are required to provide values for the emission

radii and velocities of these lines.

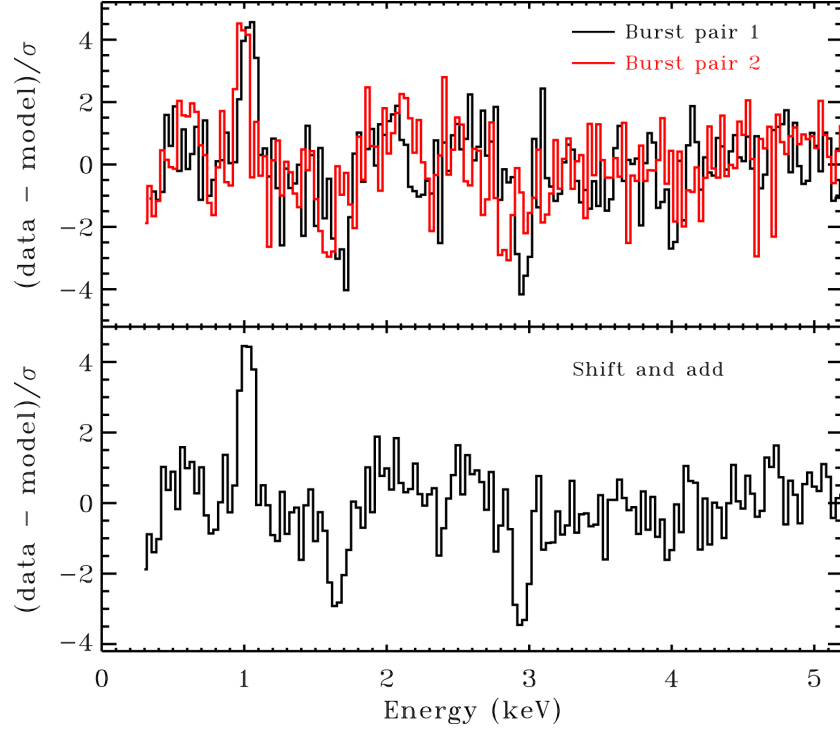


Figure 1.3.1 – Fit residuals of the absorbed blackbody model for the stronger (pair 1) and weaker (pair 2) bursts. In the bottom panel, the residuals are added after the pair 2 residuals have been shifted by the best fitting line ratio of 1.046. From Strohmayer et al. [2019].

2. What is the time-dependent evolution of the photosphere during the PRE phase, and how does it vary from burst to burst?

This question is especially relevant now with the availability of *NICER* data, which allows us to track the temperature throughout the expansion phase, and determine the emission radius with blackbody fits, as shown in Fig. 1.2.1. An important way in which this has been used is to label the peak of the blackbody temperature curve, after the expansion phase, as the *touchdown* point, i.e the moment where the atmosphere collapses back down

to the surface and the photosphere (which still presumably emits as a blackbody) is equal to the neutron star radius. For example in Fig. 1.2.1, the touchdown point is at 30s. Using this and independent measurements of the neutron star mass, M - R constraints have been placed on the neutron star equation of state [Özel and Freire, 2016].

It is not clear however if this method is truly valid, as the systematics of the photosphere’s evolution and touchdown point are not well understood, as was first pointed out by Steiner et al. [2010]. A possible scenario in which the touchdown interpretation would be incorrect is one in which the atmosphere does not collapse to the surface right after the main expansion phase, but rather remains slightly expanded above the surface, sustained by a still substantial burning layer flux. It would then slowly fall back down to the surface as the neutron star cools. The true touchdown point could therefore be much later than the PRE phase, far into the tail of the burst light curve, at which point the emission might no longer be a blackbody. Therefore, more work needs to be done to model the evolution of the photosphere, and how it relates to the observables, e.g., the total luminosity and effective temperature of the spectra, as a function of time.

Another reason it is important to understand these systematics is that PRE bursts are often used as standard candles to determine the distance to neutron stars. This is done by assuming that the luminosity at the photosphere is the critical luminosity, which we will introduce in the next section, and relating it to the peak flux seen at the telescope by a factor $4\pi d^2$, assuming spherical emission [Galloway et al., 2008], where d is the distance to the star. While it has been shown, using sources with independently constrained distances, that many PRE bursts were indeed good standard candles (e.g. by Kuulkers et al. [2003]), significant deviations in some sources indicate that the assumptions do not always hold.

1.4 Basic theory and previous theoretical work

For a burst to exhibit PRE, a high enough luminosity must be attained in order to break hydrostatic equilibrium. The critical luminosity can be found by equating gravity and radiation pressure. Far from the star, where temperatures are low enough that the opacity is from Thomson scattering, this leads to the classical *Eddington luminosity*,

$$L_{\text{Edd}} = \frac{4\pi GMc}{\kappa_0}, \quad (1.4.1)$$

where M is the mass of the star and $\kappa_0 = 0.2(1 + X) \text{ g cm}^{-2}$ is the constant electron scattering opacity, where X is the hydrogen fraction.

Close to the star, at a distance r from the center, this changes in two ways. If we consider general relativity, then the local effective gravity is increased over the Newtonian value by a factor related to the space-time metric we choose to use. We will consider the Schwarzschild metric, which describes the space-time surrounding a central non-rotating object. Also, in general, radiation interacts with the gas in ways that depend on both its density ρ and temperature T . This must be reflected by a non-constant opacity. The *local critical luminosity* is therefore

$$L_{\text{cr}} = \frac{4\pi GMc}{\kappa(\rho, T)} \left(1 - \frac{2GM}{rc^2}\right)^{-1/2}. \quad (1.4.2)$$

At large radii, the temperature and density are small and the opacity goes to the constant κ_0 , such that $L_{\text{cr}} \rightarrow L_{\text{Edd}}$. General relativity also has the effect of differentiating the observed luminosity between different observers. If the local luminosity is L , the luminosity seen by an observer at infinity is

$$L^\infty = L \left(1 - \frac{2GM}{rc^2}\right). \quad (1.4.3)$$

There are two metric terms here, one for time dilation which makes photons

come out at a slower rate, and another for redshift, which lowers the total energy of the radiation field.

The temperature dependence of the opacity is significant in the context of bursts, since at high temperatures, when electrons reach relativistic velocities and photon collisions become subject to inelastic Compton scattering, the electron scattering opacity is drastically reduced. Paczynski [1983] gives the following interpolation formula

$$\kappa(T) = \kappa_0 \left[1 + \left(\frac{T}{4.5 \times 10^8 \text{ K}} \right)^{0.86} \right]^{-1}, \quad (1.4.4)$$

based on tabulated values of Buchler and Yueh [1976]. In bursts, temperatures of over 10^9 K are readily attained. This creates a situation where the luminosity can be very high, even *super-Eddington* (referring to Eq. 1.4.1), while at the same time being *sub-critical* (referring to Eq. 1.4.2). The atmosphere can still expand, even in the sub-Eddington case, because any luminosity causes an outward radiation pressure which reduces the effective gravity

$$g_{\text{eff}} = g \left(1 - \frac{L}{L_{\text{cr}}} \right). \quad (1.4.5)$$

So the temperature dependence of the opacity already reveals the structure of the outflows; we expect a compact, geometrically thin envelope in hydrostatic equilibrium that gradually transitions into an extended region of gas as T and L_{cr} drop, allowing the photons to “push” the gas more effectively.

But when discussing this luminosity driven expansion of the atmosphere, we are actually talking about two possible regimes, which are illustrated in Fig. 1.5.1. The first, most well-known case, is the *super-Eddington wind* regime, which will inevitably occur if $L^\infty > L_{\text{Edd}}$. This inequality implies mass loss because the luminosity is greater than Eddington all the way out to infinity, meaning matter must be flowing outwards, all the way from the star. The excess photon energy must be used to unbind accreted material,

giving the approximate relation

$$\frac{dM}{dt} \approx \frac{L^\infty - L_{\text{Edd}}}{GM/R}. \quad (1.4.6)$$

Super-Eddington winds are ubiquitous in massive stars, where the main driving mechanism is kinetic energy deposition (see for reference Quataert et al. [2016]). These burst super-Eddington winds however are radiation pressure driven, i.e., it is the photons, trapped in the optically thick fluid, that transfer their energy as they diffuse through the gas. Therefore, these winds are extremely sensitive to the exact temperature dependent scattering opacity, which is not the case for massive stellar winds as per Quataert et al. [2016].

The wind regime has been studied extensively in the past. Many papers in the 1980's demonstrated calculations of steady-state wind solutions, starting with Ebisuzaki et al. [1983] and Kato [1983b], who solved time-independent Newtonian hydrodynamics and optically thick radiative transfer equations with different assumptions and approximations. Various improvements were made in later years, such as a transition into optically thin regions [Quinn and Paczynski, 1985], the inclusion of general relativity [Paczynski and Proszynski, 1986] and more detailed radiative transfer [Joss and Melia, 1987, Nobili et al., 1994]. More recently, Yu and Weinberg [2018] performed time-dependent calculations of winds for the first time, going back to Newtonian gravity and pure optically thick radiative transfer, but with a focus on tracking the composition of different elements over time and space. The different approximations made by these various papers are summarized in Table 1.1, which shows that there clearly needs to be more work done to include all of these different effects in the same calculation.

The second, less discussed regime, is the *expanded envelope* in hydrostatic equilibrium, which occurs when $L^\infty \lesssim L_{\text{Edd}}$. With a smaller luminosity, the surface temperature is smaller than in the wind case, such that L is in fact closer to L_{cr} , triggering expansion given the effective gravity in Eq. (1.4.5).

Table 1.1 – Previous work on burst super-Eddington winds

	General Relativity	Time- dependent	Radiative transfer
Ebisuzaki et al. (1983), Kato (1983)	×	×	Optically thick only
Quinn & Paczynski (1985)	×	×	Approximate transition from optically thick to thin
Paczynski & Proszynski (1986)	✓	×	Optically thick only
Joss & Melia (1987)	×	×	Separate treatment of optically thick and thin regions
Nobili et al. (1994)	✓	×	Full (frequency-integrated) radiative transfer
Yu & Weinberg (2018)	×	✓	Optically thick only
Herrera et al. (2020)	×	×	Optically thick only

Since there is no mass loss and no velocity, there is no net transfer of energy from the photons to the gas. Therefore, the luminosity L^∞ is a constant throughout the model. The local luminosity, however, is a function of radius, according to Eq. (1.4.3). The expansion will self-adjust such that $L \lesssim L_{\text{cr}}$ at every radius in order to maintain hydrostatic equilibrium. In fact, this expanded envelope regime is a general relativistic effect, as the redshift-dependent luminosity is a requirement for maintaining equilibrium. This was explained by Paczynski and Anderson [1986], the only paper in the literature discussing relativistic expanded envelopes in relation to PRE bursts. These authors pointed out that previous attempts to model envelopes without general relativity were incorrect, and that they could only produce very compact envelopes, not the extended ones that appear with the inclusion of redshift.

1.5 Outline

The objective of this work is to improve radius expansion models to help answer many of the questions that were presented in this introduction. We have created a sequence of fully consistent envelope and steady-state wind

models that can be linked to the state of the burning layer at any point during the burst evolution. These models can be used as an outer boundary condition in time-dependent codes simulating the burning layer, as well as guides to interpret data from the large number of catalogued observations. For the first time, we can also compare the two expansion regimes to each other and analyze the transition between the two in a real burst.

We begin with a derivation of the equations of radiation hydrodynamics used throughout this work in Chapter 2, then describe the numerical method and show the results for the wind models in Chapter 3, and expanded envelope models in Chapter 4. Finally, we compare the two regimes and make final remarks on the use of these stationary solutions to describe the dynamics of different parts of PRE bursts in Chapter 5.

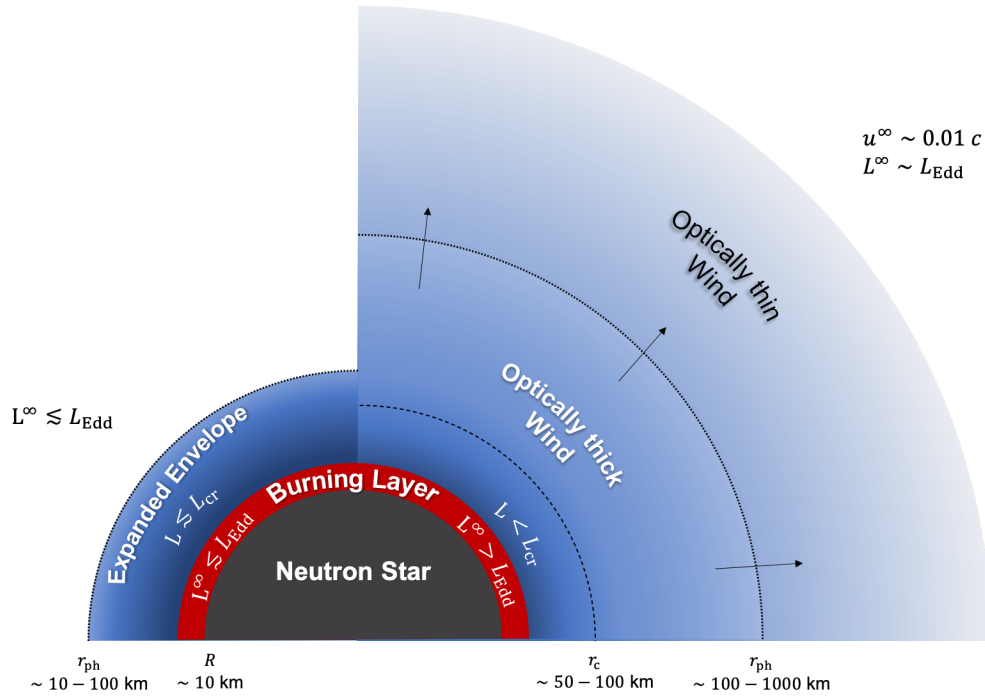


Figure 1.5.1 – Diagram summarizing the relevant quantities in the two PRE burst expansion regimes. We explain the definitions for the critical point r_c and photospheric radius r_{ph} and how to calculate solutions to these structures in Chapter 3 (winds) and Chapter 4 (envelopes).

Chapter 2

Prior on radiation hydrodynamics

The mathematical framework for the theory of radiation hydrodynamics relevant to this thesis is laid out here. The initial assumptions are that of a spherically symmetric problem around a slowly rotating neutron star, where the optically thick fluid is in local thermodynamic equilibrium. We start by writing down the main equations that dictate the physical processes at work and explain the main approximations that are to be applied to both the gas' dynamics and the radiative transfer. Then, we derive the four stationary equations of radiation hydrodynamics that describe any process taking place under our initial assumptions. These first sections of this chapter (§2.1-2.3) are a review of work done in these papers: Park [1993], Park [2006], Thorne et al. [1981], Flammang [1982]. Some of the longer and more involved derivations have been left out of this section for brevity and are instead included in Appendix D.

We then lay out the gas equation of state that relates the extensive variables for the fluid in §2.4 and conclude with the final equations of structures that are used throughout this project in §2.5.

2.1 General relativity

Since this work focuses on fluid dynamics above a compact object, it is expected that general relativistic effects might be important. We know this from a simple preliminary analysis of the Schwarzschild radius,

$$r_s = \frac{2GM}{c^2}. \quad (2.1.1)$$

For a typical neutron star with a mass of $1.4M_\odot$, r_s is of just over 4 km, while the stellar radius is somewhere in between 10 and 13 km. With a value of $\sim 2-3$, the ratio of these two radii is much lower than the Sun or the Earth, where it takes approximate values of 2×10^5 and 7×10^5 respectively. If Newtonian physics are generally appropriate to study these common objects, one has to expect corrections brought on by GR to be relevant in the case of neutron stars. These corrections include a higher effective surface gravity and critical luminosity, a redshift of outgoing radiation and of course time dilation, which requires careful treatment of fluid velocity.

We begin with the Schwarzschild metric, which describes the curvature of space-time around a spherical, non-rotating, central object, given by

$$ds^2 = g_{\mu\nu}dx^\mu dx^\nu = -\zeta^2 c^2 dt^2 + \zeta^{-2} dr^2 + r^2(d\theta^2 + \sin^2\theta d\phi^2), \quad (2.1.2)$$

where

$$\zeta = (1 - r_s/r)^{1/2} \quad (2.1.3)$$

is the curvature parameter. The metric $g_{\mu\nu}$ and its inverse $g^{\mu\nu}$ are used to lower and raise indices, according to the Einstein summation convention. In what follows, greek letters (μ, ν) will be used to denote the variables of the 4D space-time, and normal letters (i, j) 3D space. The four-velocity, defined as $U^\mu = dx^\mu/d\tau$ with τ being the proper time, has the normalization property $U_\mu U^\mu = -c^2$. This allows us to write the time (zeroth) component of the four-velocity in terms of its spatial components U^i and the curvature

parameter ζ . For purely radial motion ($U^\theta = U^\phi = 0$),

$$\Psi \equiv -U_t/c = \sqrt{\zeta^2 + (U^r/c)^2} \quad (2.1.4)$$

is often referred to as the energy parameter for the flow [Thorne et al., 1981].

Next, we define two bases, or *frames*, in this metric, which we will use to describe different fluid and radiation quantities. The **fixed frame** $x^{\hat{\mu}} = (ct, \hat{r}, \hat{\theta}, \hat{\phi})$ has no velocity with respect to the central object. For an observer in this frame, the fluid has a proper velocity $\mathbf{v} = (v^r, v^\theta, v^\phi)$. The subtle but important difference between the fixed frame and the coordinate (Schwarzschild) basis is that the fixed frame has an orthonormal basis and is locally inertial, such that every quantity within it can be defined as in a flat space-time. The radial velocity in the fixed frame is related to the radial component of the four-velocity in the coordinate basis via the energy parameter, with

$$v^r = U^r \Psi^{-1} \equiv u. \quad (2.1.5)$$

Putting this back into Eq. (2.1.4) gives a simple form for the Lorentz factor,

$$\gamma \equiv \left(1 - \frac{u^2}{c^2}\right)^{-1/2} = \frac{\Psi}{\zeta}. \quad (2.1.6)$$

Note that Eq. (2.1.5) gives the usual special relativity expression when $r \gg r_s$, i.e., the spatial component of the four-velocity is just $u\gamma$. The GR correction is to divide by a redshift factor.

The **comoving frame** $x_{\text{co}}^{\hat{\mu}} = (ct_{\text{co}}, \hat{r}_{\text{co}}, \hat{\theta}_{\text{co}}, \hat{\phi}_{\text{co}})$ is one that is fixed with respect to the moving fluid and moves with velocity \mathbf{u} with respect to the fixed frame. Therefore, a Lorentz transformation is used to link the two frames. The full details are left to the Appendix, but it is important to take note of the fact that $\partial/\partial x_{\text{co}}^{\hat{\mu}} \neq \partial/\partial x^{\hat{\mu}}$.

2.2 Stress-energy tensors

We start with the stress-energy tensor for the matter. For our purposes, we can assume the case of a perfect fluid or gas (can be fully described by its pressure P_g and rest-mass density ρ) in thermodynamic equilibrium. As such, we are ignoring effects of viscosity and heat conduction within the fluid. The stress-tensor in this case is

$$T^{\mu\nu} = \frac{\omega_g}{c^2} U^\mu U^\nu + P_g g^{\mu\nu}, \quad (2.2.1)$$

where

$$\omega_g = \rho c^2 + P_g + U_g \quad (2.2.2)$$

is the sum of the rest-mass energy and enthalpy of the gas, per unit proper volume. The gas internal energy U_g is some function of ρ and P_g , depending on the equation of state. For an ideal monatomic gas, $P_g = kT\rho/\mu m_p$ and $U_g = 3P_g/2$, where μ is the mean molecular weight of the particular gas. Note that this tensor is not expressed in either the fixed or comoving frame, but rather the initial coordinate frame $x^\mu = (ct, r, \theta, \phi)$.

A separate stress tensor is used to describe the radiation. We can define the moments in the usual way in either of our two inertial frames. The zeroth, first and second moments are respectively the radiation energy density E , the radiation flux F^i and the radiation pressure tensor P^{ij} , where $i, j = r, \theta, \phi$. We will use the symbols “ \rightarrow ” and “ $_{\text{co}}$ ” to differentiate between the two frames. In terms of the specific intensity $I_\nu(x^\mu, \mathbf{n})$, we have

$$\begin{aligned} \bar{E} &= \frac{1}{c} \iint \bar{I}_\nu d\bar{\nu} d\bar{\Omega} & E_{\text{co}} &= \frac{1}{c} \iint I_{\nu_{\text{co}}} d\nu_{\text{co}} d\Omega_{\text{co}} \\ \bar{F}^i &= \iint \bar{I}_\nu \bar{n}^i d\bar{\nu} d\bar{\Omega} & F_{\text{co}}^i &= \iint I_{\nu_{\text{co}}} n_{\text{co}}^i d\nu_{\text{co}} d\Omega_{\text{co}} \\ \bar{P}^{ij} &= \frac{1}{c} \iint \bar{I}_\nu \bar{n}^i \bar{n}^j d\bar{\nu} d\bar{\Omega} & P_{\text{co}}^{ij} &= \frac{1}{c} \iint I_{\nu_{\text{co}}} n_{\text{co}}^i n_{\text{co}}^j d\nu_{\text{co}} d\Omega_{\text{co}}, \end{aligned} \quad (2.2.3)$$

where ν is the photon frequency as measured in the frame, $d\Omega = \sin\theta d\theta d\phi$ is the solid angle element, p^α is the four-momentum and $n^i = p^i/h\nu$ is the projection along an axis. In any frame, the four-dimensional symmetric radiation stress-energy tensor is typically written as [Mihalas and Mihalas, 1984]:

$$\mathbf{R} = \begin{bmatrix} E & \mathbf{F}^T/c \\ \mathbf{F}/c & \mathbf{P} \end{bmatrix}. \quad (2.2.4)$$

For a spherically symmetric radiation field, the angular fluxes and pressure shears ($F^\theta, F^\phi, P^{r\theta}, P^{r\phi}, P^{\theta\phi}$) all vanish. Also, since this tensor is a particular case of the general electromagnetic stress-energy tensor¹, it has the property of being traceless ($R^\alpha_\alpha = \eta_{\alpha\beta} R^{\alpha\beta} = 0$ where $\eta_{\alpha\beta}$ is a flat metric with $(-, +, +, +)$ signature). We ensure this by writing

$$P^{\theta\theta} = P^{\phi\phi} = \frac{E - P^{rr}}{2}. \quad (2.2.5)$$

We can specify the comoving tensor knowing the nature and behavior of the radiation. First, since we consider the radiation to be purely thermal, the local energy density E_{co} is given by the classical Stefan-Boltzmann expression $aT^4 \equiv U_R$, where T is the local temperature of the gas. Also, in the optically thick approximation, we can say that the radiation in the comoving frame is mainly isotropic, with only a small anisotropic contribution that transports the flux outwards. Therefore, all components of the pressure diagonal in this frame are equal to a third of the energy density, that is

$$P_{\text{co}}^{rr} = P_{\text{co}}^{\theta\theta} = P_{\text{co}}^{\phi\phi} = \frac{U_R}{3}. \quad (2.2.6)$$

Finally, the comoving radial flux is just a function of the local luminosity L , with

$$F_{\text{co}}^r = L/4\pi r^2 \equiv F. \quad (2.2.7)$$

¹In CGS units : $T^{\mu\nu} = \frac{1}{4\pi} (F^{\mu\alpha} F_\alpha^\nu - \frac{1}{4} \eta^{\mu\nu} F_{\alpha\beta} F^{\alpha\beta})$, where $F^{\mu\nu}$ is the electromagnetic tensor. See Carroll [2004].

This is the same for the fixed flux which we write as \bar{F} . The radiation tensors can now be written as

$$\bar{\mathbf{R}} = \begin{bmatrix} \bar{E} & \bar{F}/c & 0 & 0 \\ \bar{F}/c & \bar{P} & 0 & 0 \\ 0 & 0 & (\bar{E} - \bar{P})/2 & 0 \\ 0 & 0 & 0 & (\bar{E} - \bar{P})/2 \end{bmatrix}, \quad (2.2.8)$$

$$\mathbf{R}_{\text{co}} = \begin{bmatrix} U_R & F/c & 0 & 0 \\ F/c & U_R/3 & 0 & 0 \\ 0 & 0 & U_R/3 & 0 \\ 0 & 0 & 0 & U_R/3 \end{bmatrix}. \quad (2.2.9)$$

The two tensors are related by a double Lorentz transform, leading to the following relations:

$$\bar{E} = \gamma^2 \left[\left(1 + \frac{1}{3} \frac{u^2}{c^2} \right) U_R + \frac{2u}{c^2} F \right], \quad (2.2.10)$$

$$\bar{F} = \gamma^2 \left[\frac{4}{3} u U_R + \left(1 + \frac{u^2}{c^2} \right) F \right], \quad (2.2.11)$$

$$\bar{P} = \gamma^2 \left[\left(\frac{u^2}{c^2} + \frac{1}{3} \right) U_R + \frac{2u}{c^2} F \right]. \quad (2.2.12)$$

Finally, we can find the radiation tensor in the coordinate frame:

$$\mathbf{R} = \begin{bmatrix} \zeta^{-2} \bar{E} & \bar{F}/c & 0 & 0 \\ \bar{F}/c & \zeta^2 \bar{P} & 0 & 0 \\ 0 & 0 & r^{-2}(\bar{E} - \bar{P})/2 & 0 \\ 0 & 0 & 0 & (r \sin \theta)^{-2}(\bar{E} - \bar{P})/2 \end{bmatrix}. \quad (2.2.13)$$

An essential condition that is to be respected is the vanishing of the divergence of the total stress-energy tensor,

$$(T^{\mu\nu} + R^{\mu\nu})_{;\nu} = 0, \quad (2.2.14)$$

where both tensors are in the coordinate frame (Eq. 2.2.1 and Eq. 2.2.13). The “;” notation is explained in Appendix D and Eq. (D.0.4). This condition ensures that there can be a solution to the Einstein field equations. Eq. (2.2.14) also implicitly describes the exchange of energy and momentum between the radiation field and the gas.

It is useful to separate Eq. (2.2.14) using the radiation four-force density, which in any frame is written as [Mihalas and Mihalas, 1984]

$$G^0 = c^{-1} \int d\nu \int d\Omega [\chi I_\nu(\mathbf{n}) - \eta(\mathbf{n})], \quad (2.2.15)$$

$$G^i = c^{-1} \int d\nu \int d\Omega [\chi I_\nu(\mathbf{n}) - \eta(\mathbf{n})] n^i, \quad (2.2.16)$$

where χ is the opacity (absorption plus scattering) per unit length and η is the emissivity per unit volume. This four-vector has the useful property

$$G^\mu \equiv -R_{;\nu}^{\mu\nu} = T_{;\nu}^{\mu\nu}. \quad (2.2.17)$$

G^0 represents the rate of energy input from the radiation into the gas, and G^i represents the rate of momentum input. These rates are best-interpreted in the comoving frame. We introduce the local heating and cooling functions

$$\Gamma_{\text{co}} = \frac{1}{c} \int d\nu_{\text{co}} \int d\Omega_{\text{co}} \chi_{\text{co}} I_{\nu_{\text{co}}}, \quad (2.2.18)$$

$$\Lambda_{\text{co}} = \frac{1}{c} \int d\nu_{\text{co}} \int d\Omega_{\text{co}} \eta_{\text{co}}. \quad (2.2.19)$$

The mean opacity coefficient is given by

$$\bar{\chi}_{\text{co}} F_{\text{co}}^i = \frac{1}{c} \int d\nu_{\text{co}} \int d\Omega_{\text{co}} \chi_{\text{co}} I_{\nu_{\text{co}}} n_{\text{co}}^i, \quad (2.2.20)$$

which leads to

$$G_{\text{co}}^{\hat{t}} = (\Gamma_{\text{co}} - \Lambda_{\text{co}})/c, \quad (2.2.21)$$

$$G_{\text{co}}^{\hat{i}} = \bar{\chi}_{\text{co}} F_{\text{co}}^i / c. \quad (2.2.22)$$

The latter comes from the assumption that the photons emitted or scattered in the comoving frame are isotropic, such that the angle averaged emissivity is zero. We will find later that we can get rid of the Γ_{co} and Λ_{co} functions to obtain our final stationary equations. Therefore, the microphysics describing the interaction between the matter and the radiation will be fully described by the mean opacity *coefficient* in the comoving frame $\bar{\chi}_{\text{co}}$. For familiarity, we will instead use the mean opacity

$$\kappa \equiv \frac{\bar{\chi}_{\text{co}}}{\rho}, \quad (2.2.23)$$

which has units of cross section per unit mass.

2.3 Hydrodynamics equations

It is straightforward to obtain the equation for conservation of mass from the universal covariant continuity equation

$$(nU^\mu)_{;\mu} = 0, \quad (2.3.1)$$

where n is the number density of particles. Applying the derivatives according to the Schwarzschild metric, we obtain

$$\frac{1}{\zeta^2} \frac{\partial}{\partial t} (n\Psi) + \frac{1}{r^2} \frac{\partial}{\partial r} (r^2 n u \Psi) = 0. \quad (2.3.2)$$

Then, we can obtain three more equations from the zero-divergence property of the stress tensor (Eq. 2.2.14), which has been re-written using the

radiation four-force density G^μ in the last section. From $T_{;\nu}^{\mu\nu} = G^\mu$, we can obtain the r -momentum and energy conservation equations using projection operators – details are in Appendix D. These equations are:

$$\frac{\Psi}{\zeta^2} \frac{\partial}{\partial t} (u\Psi) + \frac{1}{2} \frac{\partial}{\partial r} (u\Psi)^2 + \frac{GM}{r^2} + \frac{u\gamma^2}{\omega_g} \frac{\partial P_g}{\partial t} + \frac{c^2\Psi^2}{\omega_g} \frac{\partial P_g}{\partial r} = \frac{\Psi c}{\omega_g} \rho\kappa F, \quad (2.3.3)$$

$$\frac{n\Psi}{\zeta^2} \frac{\partial}{\partial t} \left(\frac{\omega_g}{n} \right) + nu\Psi \frac{\partial}{\partial r} \left(\frac{\omega_g}{n} \right) - \frac{\Psi}{\zeta^2} \frac{\partial P_g}{\partial t} - u\Psi \frac{\partial P_g}{\partial r} = \Gamma_{\text{co}} - \Lambda_{\text{co}}. \quad (2.3.4)$$

Finally, the radiation moment equations are to be found from $R_{;\nu}^{\mu\nu} = -G^\mu$. The zeroth moment, or energy equation, is $\mu = t$, while the first moment, or radiation force balance equation, is $\mu = r$:

$$\frac{1}{\zeta^2} \frac{\partial \bar{E}}{\partial t} + \frac{1}{\zeta^2 r^2} \frac{\partial}{\partial r} (r^2 \zeta^2 \bar{F}) = \frac{\gamma}{\zeta} \left(\Lambda_{\text{co}} - \Gamma_{\text{co}} - \frac{u}{c} \rho\kappa F \right), \quad (2.3.5)$$

$$\begin{aligned} \frac{\partial \bar{F}}{\partial t} + c^2 \zeta^2 \frac{\partial \bar{P}}{\partial r} + \frac{GM}{r^2} (\bar{E} + \bar{P}) + \frac{c^2 \zeta^2}{r} (3\bar{P} - \bar{E}) \\ = u\Psi (\Lambda_{\text{co}} - \Gamma_{\text{co}}) - \Psi c \rho\kappa F. \end{aligned} \quad (2.3.6)$$

Equations (2.3.2)-(2.3.6) fully describe the time-dependent evolution of the density, velocity, internal energy, radiative energy and flux of a spherically symmetric, optically thick fluid in thermodynamic equilibrium, in a Schwarzschild metric. The only missing piece is a set of equations to connect the gas' intensive variables (temperature, density, pressure). This piece is the equation of state (EOS), which we will describe in section 2.4.

But first, we can simplify the equations by removing the time-dependent terms, with the scope of this project being on steady-state solutions. With only derivatives with respect to r remaining, we will use the prime symbol ($'$) to denote derivatives. In Eq. (2.3.2), we can replace n by ρ and add a factor of 4π for spherical geometry such that the conserved quantity is the mass loss rate

$$\boxed{\dot{M} = 4\pi r^2 \rho u \Psi}. \quad (2.3.7)$$

The r -momentum equation (2.3.3) can be written as

$$\boxed{\omega_g(\ln \Psi)' + P'_g - \frac{1}{c\Psi}\rho\kappa F = 0} . \quad (2.3.8)$$

Combining Eq. (2.3.5) and (2.3.6) to remove the heating and cooling functions, we obtain an equation that describes the interchange between radiative energy, flux and pressure. In steady-state, this is

$$c^2\zeta^2\bar{P}' - \frac{u}{r^2}(r^2\zeta^2\bar{F})' + \frac{GM}{r^2}(\bar{E} + \bar{P}) + \frac{c^2\zeta^2}{r}(3\bar{P} - \bar{E}) + \frac{\zeta c}{\gamma}\rho\kappa F = 0 . \quad (2.3.9)$$

Transforming the fixed frame quantities to the comoving frame using Eq. (2.2.10)-(2.2.12) and assembling the derivatives, we get

$$\frac{(\Psi^4 U_R)'}{3\Psi^3} + \frac{(r^2 u^2 \Psi^2 F)'}{c^2 r^2 u \Psi} + \frac{\rho\kappa F}{c} = 0 . \quad (2.3.10)$$

We can simplify this equation even further using the optically thick approximation. In this regime, the flux is of order of magnitude $\tau^{-1}cU_R$, where τ is the optical depth which is larger than 1 [Thorne et al., 1981]. To make an order of magnitude comparison, let us set macroscopic length scale $\mathcal{L} \sim \tau/\rho\kappa$. Then :

$$\frac{(\Psi^4 U_R)'}{3\Psi^3} \sim \frac{U_R}{\mathcal{L}} \quad (2.3.11)$$

$$\frac{(r^2 u^2 \Psi^2 F)'}{c^2 r^2 u \Psi} \sim \frac{u}{c^2} \frac{cU_R}{\tau \mathcal{L}} \sim \frac{u}{c\tau} \frac{U_R}{\mathcal{L}} \quad (2.3.12)$$

$$\frac{\rho\kappa F}{c} \sim \frac{\tau}{\mathcal{L}c} \frac{cU_R}{\tau} \sim \frac{U_R}{\mathcal{L}} . \quad (2.3.13)$$

In this work, we will be dealing with non-relativistic fluids ($u \ll c$) which makes it evident that the middle term in Eq. (2.3.10) can be neglected, and we end up with a simple expression for the flux as a function of the energy

density gradient,

$$F = \frac{c}{3\kappa\rho} \frac{(\Psi^4 U_R)'}{\Psi^3}. \quad (2.3.14)$$

Since $U_R = aT^4$, we have recovered the standard photon diffusion equation, with some additional factors and derivatives of Ψ , which account for photon redshift and length contraction.

All that is left to be found is an energy equation. We once again combine equations to remove the heating and cooling functions, this time the two energy equations (2.3.4) and (2.3.5),

$$nu\Psi^2 \left(\frac{\omega_g}{n}\right)' + \frac{1}{r^2} (r^2 \zeta^2 \bar{F})' - u\Psi^2 P_g' + \frac{u\Psi}{c} \rho \kappa F = 0. \quad (2.3.15)$$

Adding $u\Psi^2$ times Eq. (2.3.8) gets rid of the P_g and F terms. We use mass conservation written as $(r^2 nu\Psi)' = 0$ to remove the n' term, giving

$$0 = \frac{1}{r^2} (r^2 \Psi^2 u \omega_g + r^2 \zeta^2 \bar{F})'. \quad (2.3.16)$$

We have arrived at a Bernoulli equation for the flow, where the energy in the steady-state is a balance of radiation (\bar{F}), and rest mass, gravitational, kinetic and internal energies ($\Psi\omega_g$). To see this, we can expand Ψ to first order:

$$\begin{aligned} \Psi\omega_g &\approx \left(1 - \frac{GM}{c^2 r}\right) \left(1 + \frac{1}{2} \frac{u^2}{c^2}\right) (\rho c^2 + P_g + U_g) \\ &\approx \rho \left(1 - \frac{GM}{c^2 r} + \frac{1}{2} \frac{u^2}{c^2}\right) \left(c^2 + \frac{P_g + U_g}{\rho}\right) \\ &\approx \rho \left(c^2 - \frac{GM}{r} + \frac{u^2}{2} + \frac{P_g + U_g}{\rho}\right), \end{aligned} \quad (2.3.17)$$

where we ignored cross-products of small terms. Notice that the quantity in parentheses in Eq. (2.3.17) is the usual non-relativistic Bernoulli's constant

for an ideal gas in a gravitational potential.

Now to obtain an integration constant, we integrate Eq. (2.3.16) and use the frame transformation for \bar{F} , giving

$$C = r^2 \Psi^2 u \rho \left(\frac{\omega_g + 4U_R/3}{\rho} \right) + \Psi^2 \left(1 + \frac{u^2}{c^2} \right) r^2 F. \quad (2.3.18)$$

Finally, we multiply by 4π and use the definitions for \dot{M} (2.3.7) and L^∞ (1.4.3) to obtain the final energy equation:

$$4\pi C = \boxed{\dot{M} \Psi \left(\frac{\omega_g + 4U_R/3}{\rho} \right) + \left(\frac{1 + u^2/c^2}{1 - u^2/c^2} \right) L^\infty = \dot{E}}. \quad (2.3.19)$$

It represents the fact that the total energy loss rate of the flow, which we defined as \dot{E} , is the rate of change of rest mass energy, enthalpy and radiative energy and pressure, plus the luminosity as seen by an observer at infinity, but boosted by a Doppler-like factor.

This is the end of the preliminary derivations, as we have derived our four equations to fully describe the steady-state flow: conservation equations for mass and energy (2.3.7, 2.3.19), the momentum equation (2.3.8) and the photon diffusion equation (2.3.14). All of the calculations in this thesis are founded on these four boxed equations.

2.4 Equation of state

This is where our first divergence from existing literature begins. Indeed, while previous work on expanded atmospheres and winds considered an ideal gas EOS, we are considering a more accurate one that includes degenerate electron corrections. These corrections become important at high densities and temperatures, conditions that we expect to reach close to the neutron star surface.

Our EOS is written as a partially-degenerate ionized gas pressure, with

contributions from ions (i) and both non-relativistic and relativistic electrons (e). For these, we use fitting formulas given by Paczynski [1983], which interpolate smoothly between the non-degenerate (nd), degenerate non-relativistic (dnr) and degenerate relativistic (dr) regimes of electron pressure:

$$P_i = \frac{kT\rho}{\mu_i m_H} \quad P_{\text{end}} = \frac{kT\rho}{\mu_e m_H} \quad P_{\text{ednr}} = K_{\text{nr}} \rho^{5/3} \quad P_{\text{edr}} = K_r \rho^{4/3} \quad (2.4.1)$$

where μ_i and μ_e are the mean molecular weight per ion and electron, m_H is the hydrogen mass and k is the Boltzmann constant. The electron pressure constants,

$$K_{\text{nr}} = 9.91 \times 10^{12} \mu_e^{-5/3} \quad K_r = 1.231 \times 10^{15} \mu_e^{-4/3}, \quad (2.4.2)$$

are taken from Paczynski [1983]. The interpolation formulas are

$$P_{\text{ed}} = (P_{\text{ednr}}^{-2} + P_{\text{edr}}^{-2})^{-1/2} \quad P_e = (P_{\text{end}}^2 + P_{\text{ed}}^2)^{1/2}. \quad (2.4.3)$$

The internal energy of the ions is the ideal gas formula $U_i = \frac{3}{2} P_i$, and we will define the internal energy of the electrons U_e later. The total gas pressure and internal energy are therefore:

$$P_g = P_i + P_e \quad U_g = U_i + U_e \quad (2.4.4)$$

Note that we define U as an energy density (per unit volume) rather than a specific energy (per unit mass) as in Paczynski [1983]. We also define the following pressure ratio parameters:

$$\begin{aligned} \beta_i &= \frac{P_i}{P_g + U_R/3} & \beta_e &= \frac{P_e}{P_g + U_R/3} & \alpha_1 &= \left(\frac{P_{\text{end}}}{P_e} \right)^2 & \alpha_2 &= \left(\frac{P_{\text{ed}}}{P_e} \right)^2 \\ f &= \frac{5}{3} \left(\frac{P_{\text{ed}}}{P_{\text{ednr}}} \right)^2 + \frac{4}{3} \left(\frac{P_{\text{ed}}}{P_{\text{edr}}} \right)^2. \end{aligned} \quad (2.4.5)$$

Note that we are using the common β parameter notation for ratios of specific pressure over the total (gas+radiation) pressure. The f parameter leads to the expression

$$U_e = \frac{P_e}{f - 1}, \quad (2.4.6)$$

as per Paczynski [1983]. The EOS will enter the models through the ω_g and P'_g terms in the hydrodynamic equations.

2.5 Structure equations

The last step is to combine the flow and radiation equations to the equation of state in order to obtain equations for the first derivatives of the temperature, density and velocity. These are the equations that will be numerically integrated to produce solutions for both winds and envelopes.

First, the temperature gradient equation can be obtained by expanding the photon diffusion equation (2.3.14), giving

$$\begin{aligned} \frac{1}{T} \frac{dT}{dr} &= \frac{3\kappa\rho F}{4acT^4\Psi} - \frac{1}{\Psi} \frac{d\Psi}{dr} \\ &= \frac{3\kappa\rho F}{4acT^4\Psi} - \frac{GM}{c^2 r^2 \zeta^2} - \frac{\gamma^2 v}{c^2} \frac{dv}{dr}. \end{aligned} \quad (2.5.1)$$

The velocity gradient equation will come from the momentum equation. This is also where the equation of state comes in with the P'_g term. For the ions, we simply have

$$\frac{dP_i}{dr} = \frac{P_i}{T} \frac{dT}{dr} + \frac{P_i}{\rho} \frac{d\rho}{dr}. \quad (2.5.2)$$

For the electrons, it is easier to use logarithm derivatives,

$$\frac{d \ln P_e}{dr} = \frac{\partial \ln P_e}{\partial \ln \rho} \frac{d \ln \rho}{dr} + \frac{\partial \ln P_e}{\partial \ln T} \frac{d \ln T}{dr}, \quad (2.5.3)$$

because the interpolation formulas (2.4.3) lead to

$$\frac{\partial \ln P_e}{\partial \ln \rho} = \alpha_1 + \alpha_2 f \quad \frac{\partial \ln P_e}{\partial \ln T} = \alpha_1. \quad (2.5.4)$$

The momentum equation now reads

$$\begin{aligned} 0 = & \left(\rho c^2 + \frac{5}{2} P_i + \frac{f}{f-1} P_e \right) \left(\frac{GM}{c^2 r^2 \zeta^2} + \frac{\gamma^2 v}{c^2} \frac{dv}{dr} \right) \\ & + \frac{P_i}{T} \frac{dT}{dr} + \frac{P_i}{\rho} \frac{d\rho}{dr} + P_e \left((\alpha_1 + \alpha_2 f) \frac{d \ln \rho}{dr} + \alpha_1 \frac{d \ln T}{dr} \right) \\ & - \frac{1}{c \Psi} \rho \kappa F. \end{aligned} \quad (2.5.5)$$

The temperature derivative terms can be replaced by Eq. (2.5.1), and by differentiating the conservation of mass equation (2.3.7) we can write

$$\frac{d \ln \rho}{dr} = -\frac{2}{r} - \frac{d \ln u}{dr} - \frac{d \ln \Psi}{dr}. \quad (2.5.6)$$

Then, dv/dr can be solved for in Eq. (2.5.5), and plugged back in to Eq. (2.5.6) to obtain $d\rho/dr$. After all of this work, the final equations of structure can be compactly written as

$$\frac{d \ln u}{d \ln r} = \frac{(GM/r\zeta^2)(A_e - B_e/c^2) - 2B_e - C_e}{\gamma^2(B_e - v^2 A_e)} \quad (2.5.7)$$

$$\frac{d \ln \rho}{d \ln r} = \frac{(2v^2 - GM/\Psi^2 r) A_e + C_e}{B_e - v^2 A_e} \quad (2.5.8)$$

$$\frac{d \ln T}{d \ln r} = -T^* - \frac{GM}{c^2 \zeta^2 r} - \frac{\gamma^2 v^2}{c^2} \frac{d \ln u}{d \ln r}, \quad (2.5.9)$$

where

$$\begin{aligned}
T^* &= \frac{3\kappa\rho r F}{4acT^4\Psi} = \frac{1}{\Psi} \frac{L}{L_{\text{Edd}}} \frac{\kappa}{\kappa_0} \frac{GM}{r} \frac{3\rho}{4U_R} \\
A_e &= 1 + \frac{3}{2} \frac{P_i}{\rho c^2} + \frac{P_e}{\rho c^2} \left(\frac{f}{f-1} - \alpha_1 \right) \\
B_e &= \frac{P_i}{\rho} + \frac{P_e}{\rho} (\alpha_1 + \alpha_2 f) \\
C_e &= \frac{1}{\Psi} \frac{L}{L_{\text{Edd}}} \frac{\kappa}{\kappa_0} \frac{GM}{4r} \left(\frac{4 - 3\beta_i - (4 - \alpha_1)\beta_e}{1 - \beta_i - \beta_e} \right). \tag{2.5.10}
\end{aligned}$$

This notation was chosen for a very specific reason. It is of interest to consider the non-degenerate limit of the gas, where the corrections applied to the electron pressure and internal energy are negligible, and the gas as a whole can be treated as an ideal gas. Going back to Eq. (2.4), this limit can be written as

$$f \rightarrow \frac{5}{3} \quad \alpha_1 \rightarrow 1 \quad \alpha_2 \rightarrow 0 \quad P_g \rightarrow \frac{kT\rho}{\mu m_H}, \tag{2.5.11}$$

where μ is the mean molecular weight of the gas as a whole. In this case, we write the A, B and C parameters, without the “e” subscript,

$$\begin{aligned}
A &= 1 + \frac{3}{2} \frac{c_s^2}{c^2} \\
B &= c_s^2 \\
C &= \frac{1}{\Psi} \frac{L}{L_{\text{Edd}}} \frac{\kappa}{\kappa_0} \frac{GM}{4r} \left(\frac{4 - 3\beta}{1 - \beta} \right), \tag{2.5.12}
\end{aligned}$$

where $\beta = \beta_i + \beta_e$ and

$$c_s = (P_g/\rho)^{1/2} \tag{2.5.13}$$

is the sound speed.

In the non-degenerate limit, the pressure is given by the ideal gas formula and the sound speed is a function of temperature only. With these

parameters, Eq. (2.5.7)-(2.5.9) are equivalent to those used in Paczynski and Proszynski [1986], who once again calculated stationary relativistic wind solutions, but with a pure ideal gas equation of state. This demonstrates that our equations are simply an extension of the ones shown in this important paper. At the high densities near the surface of the star and at the base of the winds, the degenerate electron corrections that we have included should help make our equations more physically accurate. This was the main objective in applying the Paczynski [1983] EOS to the outflow problem described by Paczynski and Proszynski [1986], and constitutes our main improvement over previous models in the literature.

Lastly, we note that the procedure of finding solutions to the equations of structure only needs to involve numerical integration of two of the three ODEs or equations of structure². In the outflowing case ($u \neq 0$), at any point r , if two variables among (u, T, ρ, L) are known, the other two can be found from the equations of conservation of mass (2.3.7) and energy (2.3.19). This of course implies that \dot{M} and \dot{E} must have been set previously and are free parameters of the solution. The third equation of structure could also be integrated simultaneously, but it would be redundant and increase computing time. In the static case ($u = 0$), L is a function of r and the constant L^∞ , as was explained in Chapter 1. So again, only two equations of structure need to be integrated, $d\rho/dr$ and dT/dr .

²There are technically four ODEs; dL/dr , which can be found by differentiating the equation for \dot{E} , was omitted.

Chapter 3

Winds

We set out to find continuous and monotonic solutions to the equations of structure (2.5.7)-(2.5.9) for a neutron star of mass $M = 1.4M_{\odot}$ and radius $R = 12$ km. In these winds, the velocity u should be small near the star's surface and accelerate outward against gravity, representing a progressive transfer of energy from gas enthalpy and radiation into kinetic energy. Each solution to the equations is characterized by a unique set of two free parameters, the mass and energy loss rates \dot{M} and \dot{E} .

Not every solution will be physically acceptable as a neutron star wind. Thus, boundary/initial conditions will have to be enforced. One will come from attaching the wind base to the surface of the star, another from the thermal definition of the photosphere. A third condition will appear from the requirement of a continuously accelerating solution, and follow naturally from a topological feature of the equations of structure. We begin this chapter by explaining this third condition in §3.1, then describe our numerical method along with the two other boundary conditions in §3.2. We then explain the root-finding method which leads to the final wind models in §3.3, which we show and analyze in §3.4. Lastly, we discuss how our models relate to observations in terms of photospheric radii and spectral shifts in §3.5.

3.1 The critical point

In the winds, as the velocity monotonically increases outward to infinity, the sound speed decreases with the square root of the temperature (see Eq. 2.5.13). This means that the velocity will necessarily go from being subsonic to supersonic at some point. This point is the *critical point*, located at $r = r_c$.

The critical point, sometimes also called sonic point, has been a universal feature of stellar wind modeling since the first solar wind paper by Parker [1958]. It is notable because it always appears as a singularity in the velocity gradient equation, no matter the choice of equation of state. In our case, for Eq. (2.5.7), the singularity occurs at the critical velocity $u = u_c \equiv \sqrt{B/A}$, with the determinant going to zero. Note that this is very close to the sound speed but not exactly it ($A \gtrsim 1$ because of GR corrections). In order for the velocity to smoothly pass through r_c , its derivative must be finite. This can only be possible if the numerator of Eq. (2.5.7) is also exactly zero at the critical point, giving the constraint

$$\left[\frac{GM}{r\zeta^2} \left(A - \frac{B}{c^2} \right) - 2B - C \right]_{r=r_c, u=u_c} = 0. \quad (3.1.1)$$

There will be numerical divergences in the vicinity of the critical point because both the numerator and denominator of du/dr are close to zero and change sign exactly at r_c . Considering GR, this is even more of a problem because the velocity gradient also appears in the temperature gradient equation (2.5.9). There have been several proposed methods for dealing with these instabilities. For example, Paczynski and Proszynski [1986] approximated $d \ln u / d \ln r \approx 1$ and $d \ln T / d \ln r \approx -1$ near r_c , and used these values to integrate away from the critical point until du/dr became stable. Zytkov [1972], Kato [1983b] and Quinn and Paczynski [1985] used analytical expansion formulas for du/dr that would become very involved in the GR case. Joss and Melia [1987] introduced a novel change of variables which immedi-

ately cancels the singular denominator, which is arguably the simplest and most elegant solution to the singularity problem. We introduce here a GR analog to the Joss and Melia [1987]’s Φ variable,

$$\Phi = A^{1/2}\mathcal{M} + \frac{1}{A^{1/2}\mathcal{M}}, \quad (3.1.2)$$

where $\mathcal{M} = u/B^{1/2}$ is the usual mach number. Φ has a value of exactly 2 at $r = r_c$. Since the non-degenerate parameters A, B, C are functions of temperature only, the gradient takes the simple form

$$\frac{d\Phi}{dr} = \frac{(A\mathcal{M}^2 - 1)(3B - 2Ac^2)}{4\mathcal{M}A^{3/2}c^2r} \frac{d\ln T}{d\ln r} - \frac{B - Av^2}{vr\sqrt{AB}} \frac{d\ln u}{d\ln r}. \quad (3.1.3)$$

By substituting in equation (2.5.7) into the second term, we see that the denominator at the critical point cancels, and so we may use this expression to smoothly integrate around and through r_c . As for the temperature gradient Eq. (2.5.9), the last term containing du/dr (and therefore also the singularity) is small and may be ignored, as it will be shown that $u \sim 0.01c$ at most in the winds.

3.2 Numerical integration and boundary conditions

To calculate wind solutions, we use an approach similar to Paczynski and Proszynski [1986] in that we start at the critical point and integrate outward to the photosphere and inward to the star’s surface, checking if the boundary conditions are met at both ends and changing the free parameters until they are. Table 3.1 summarizes the conditions that are applied at the three locations, which we will explain in detail in this section. We apply the same procedure for every mass-loss rate \dot{M} in order to have a single wind model for each value. All integrations are done using fully implicit ODE solvers

provided by the *SciPy* numerical package [Virtanen et al., 2020].

The critical point is first found based on a trial value for its temperature T_c by finding the unique root to Eq. (3.1.1). Not all values of r_c are acceptable. For instance, if T_c is too high, the critical point can be located at $r < R$, below the surface of the star, such that the wind would start off supersonic at the base - we do not accept solutions of this kind.

We then integrate equations (2.5.9) and (3.1.3) for T and Φ , with initial values of T_c and 2, outward until reaching a *photosphere* at $r = r_{\text{ph}}$. We define the photosphere as the location where the *optical depth parameter*

$$\tau^* \equiv \rho \kappa r \quad (3.2.1)$$

reaches a value of 3. This is only an approximation of the photosphere. It must be made because our treatment of radiative transfer is done under a pure optically thick approximation. But this use of τ^* as a proxy for the true optical depth can and has been justified, e.g. by Quinn and Paczynski [1985]¹. If our equations did allow integration past the photosphere and into the optically thin regions to any distance, we could calculate this true optical depth

$$\tau(r) = \int_r^\infty \rho(r') \kappa(r') \frac{dr'}{\zeta(r')} \quad (3.2.2)$$

At large distances, $\kappa \approx \kappa_0$, $\zeta \approx 1$, and u is nearly constant such that ρ can be approximated as a power law

$$\rho = \dot{M} / (4\pi r^2 u \Psi) \approx C r^{-n}, \quad (3.2.3)$$

with $n \gtrsim 2$. Then, at the photosphere we have

$$\tau(r_{\text{ph}}) \approx \kappa_0 C \int_{r_{\text{ph}}}^\infty \frac{dr'}{(r')^n} = \frac{\kappa_0 C r_{\text{ph}}^{-(n-1)}}{n-1} = \frac{\tau^*(r_{\text{ph}})}{n-1}, \quad (3.2.4)$$

¹See also Mihalas [1978, Chapter 7.6] for a more extensive discussion on spherically symmetric grey atmospheres.

showing that the use of τ^* close to the photosphere is appropriate for these winds.

Another condition for the photosphere is that the flux escaping it locally should reflect what is observed spectrally at infinity. For a thermally emitting region with effective temperature T_{eff} , the bolometric flux is $F_{\text{bol}} = \sigma T_{\text{eff}}^4$. Our photosphere should therefore also have the thermal condition $T_{\text{ph}} \equiv T(r_{\text{ph}}) = T_{\text{eff}}$. Combining both definitions leads to our outer boundary condition:

$$L_{\text{ph}} = 4\pi r_{\text{ph}}^2 \sigma T_{\text{ph}}^4 \quad , \quad r_{\text{ph}} = r(\tau^* = 3) . \quad (3.2.5)$$

This condition will not be satisfied in general, as we are simply “shooting” from the critical point, rather than enforcing it. When reaching r_{ph} , we register the *outer boundary error* as $L_{\text{ph}} - 4\pi r_{\text{ph}}^2 \sigma T_{\text{ph}}^4$ for the root-finding procedure. Note that $\tau^* = 3$ is used because Quinn and Paczynski [1985] (Newtonian wind models that also treat optically thin regions) showed that $T = T_{\text{eff}}$ was always satisfied for $3 < \tau^* < 5$. Then, Paczynski and Proszynski [1986] showed that either value (3 or 5) led to similar results in their GR wind models. One can also see from Eq. (3.2.4) that $\tau^* = 3$ corresponds to τ of order unity, which is indeed what we usually expect for the photosphere of stellar atmospheres. Further, we found that it was not generally possible to reach smaller values of τ^* without diverging, which seems to be a limitation of the optically thick approximation.

Then, we go back to the critical point, this time to integrate inwards. We do this in two parts. Firstly, we once again integrate T and Φ but only until we reach $r = 0.95r_c$. The point of this is simply to step off of the critical point, using Φ to avoid any numerical problems. But then, we want to consider degenerate electron corrections to calculate the inner part of the wind, which Φ is not set up to do. So, we then switch to integrating r and T with ρ as the independent variable, all the way down to the surface of the star, constructing equations for $dr/d\rho$ and $dT/d\rho$ from Eq. (2.5.8) and (2.5.9). We use ρ as the independent variable instead of r at this stage because the

inner part of the wind, near the surface, is in hydrostatic equilibrium and is geometrically thin. Integrating with r , a variable which changes very little while the others change by many orders of magnitude, would be less stable numerically. We stop the integration once we reach the base of the wind r_b , which we define as the location where the column depth y reaches a value of 10^8 g cm^{-2} . The column depth,

$$y(r) \equiv \int_r^\infty \rho \frac{dr'}{\zeta(r')}, \quad (3.2.6)$$

is a mass coordinate which is given by the integrated density above a particular point r , factoring in length contraction for the given metric.

Having performed time-dependent cooling calculations of the burning layers in Type I X-ray bursts using the *burstcool* code [Cumming and Macbeth, 2004, Cumming et al., 2006], we were able to identify this particular value of 10^8 g cm^{-2} for the column depth as a sensible and consistent location for the beginning of the outflows, or base of the wind. It is small enough that the pure helium assumption remains valid. At higher depths, we would expect a significant fraction of heavy elements as products of nuclear burning. But it is also large enough that the gas should not be in a radiation pressure dominated regime at the base. We will re-visit the validity of this statement when analyzing the results further.

In hydrostatic equilibrium, the total pressure must compensate the gravitational pressure of all of the material above, which can be compactly written as

$$P = gy, \quad (3.2.7)$$

where

$$g = \frac{GM}{R^2\zeta(R)} = \frac{GM}{R^2} \left(1 - \frac{r_s}{R}\right)^{-1/2} \quad (3.2.8)$$

is the effective surface gravity of the star. This allows us to calculate the column depth from the pressure. Our inner boundary condition is simply to

require that the wind base be located at the surface of the star, that is

$$r_b \equiv r(P/g = 10^8) = R. \quad (3.2.9)$$

The point of this boundary condition is mainly to fix the wind to the surface to properly compare different solutions, and to restrict the free parameters in order to have a single wind solution per value of \dot{M} . It is not too different from the inner boundary condition of Paczynski and Proszynski [1986], who required a fixed temperature of $10^{9.7}$ K at the surface. Once again, this boundary condition will not be satisfied in general, so we record the *inner boundary error* as $r_b - R$.

Table 3.1 – Locations and conditions in the wind model

r	Name	Condition
r_b	Wind base radius	Matching to stellar radius (Eq. 3.2.9)
r_c	Critical radius	Regularity constraint (Eq. 3.1.1)
r_{ph}	Photospheric radius	Thermal constraint (Eq. 3.2.5)

3.3 Root-finding

An exact wind solution, respecting the inner and outer boundary conditions, is found for each value of \dot{M} by performing a Newton-Raphson root-finding algorithm on the (\dot{E}, T_c) parameter space. Figure 3.3.1 shows this parameter space for $\log \dot{M} = 18.5$. The white lines indicate the minima of the errors on the boundary conditions. For this value of $\log \dot{M}$, we can see that the root, located at the intersection of the two lines, is $\dot{E} \approx 9.11 L_{\text{Edd}}$, $T_c \approx 10^{7.2}$ K.

In order to automatically find the roots at every \dot{M} without having to fully calculate the errors on the parameter space as in Fig. 3.3.1, we implemented a custom Newton-Raphson searching algorithm, which essentially does a two-dimensional gradient descent towards the global minimum, with

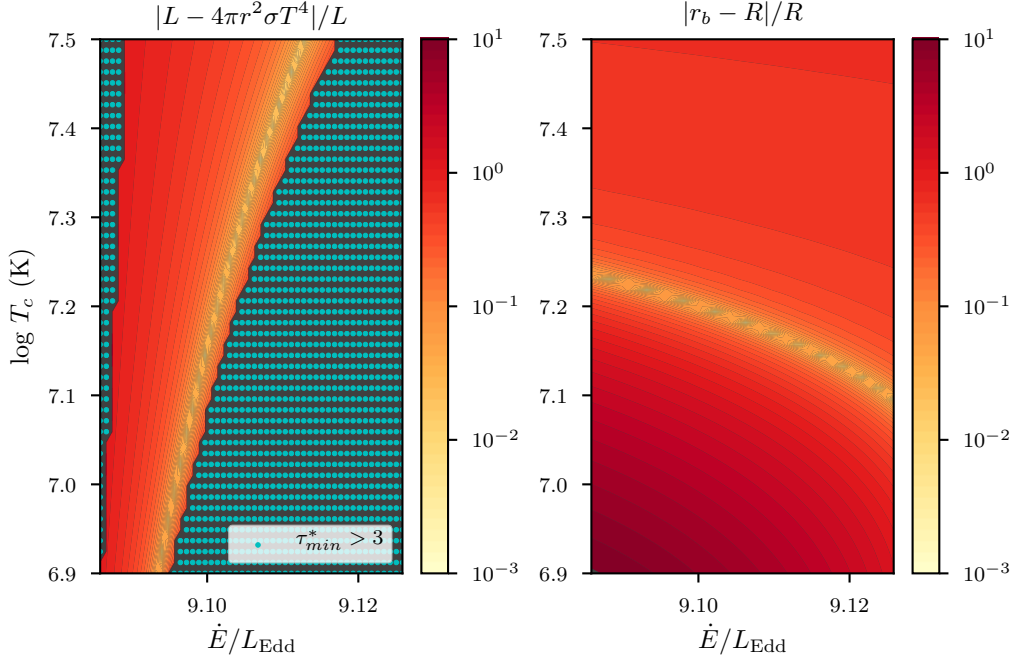


Figure 3.3.1 – Boundary condition errors on the (\dot{E}, T_c) parameter space for $\log \dot{M} = 18.5$. *Left*: Outer boundary error of Eq. (3.2.5) (“ph” subscripts omitted in the subplot title). *Right*: Inner boundary error of Eq. (3.2.9). The absolute value of the normalized errors are shown for clarity. Blue points represent free parameter values for which integration to the photosphere was not possible due to τ^* rising before reaching a value of 3.

back-tracking and numerical error catching when approaching regions of divergence, such as the blue dotted region in Fig. 3.3.1 (see figure caption for explanation). We encountered other types of divergence at lower values of \dot{M} , which we show along with other parameter spaces in Appendix B.

The result of the root-finding method are shown in figure 3.3.2. One striking feature of the root curve is the turnover in T_c at low \dot{M} . Indeed, instead of the critical point temperature continuing to increase as \dot{M} decreases, it starts to decrease at $\dot{M} \lesssim 10^{18}$ g/s. This causes the critical point to become further from the surface and closer to the photosphere as

\dot{M} decreases. At even lower values of \dot{M} , the critical point would eventually go past the photosphere, and our method would not allow the calculation of these models. A similar behavior of the critical point was obtained by Paczynski and Proszynski [1986].

In the left panel of Fig. 3.3.2, we represented the \dot{E} free parameter as $\dot{E} - \dot{M}c^2$ to look at the energy loss rate without the rest mass contribution. What we see is that the remaining contributions to the energy loss rates are roughly constant and just above L_{Edd} . To explain this, we can take the energy conservation equation (2.3.19) and evaluate it at infinity:

$$\begin{aligned} \dot{E} &= \dot{M}\Psi_{\infty} \left(\frac{\omega_{g,\infty} + 4/3U_{R,\infty}}{\rho_{\infty}} \right) + \left(\frac{1 + u_{\infty}^2/c^2}{1 - u_{\infty}^2/c^2} \right) L^{\infty} \\ \dot{E} - \dot{M}c^2 &\approx \dot{M}c^2(\gamma_{\infty} - 1) + \dot{M}\gamma_{\infty} \left(\frac{5kT_{\infty}}{2\mu m_H} + \frac{4aT_{\infty}^4}{3\rho_{\infty}} \right) \\ &\quad + \gamma_{\infty}^2(1 + u_{\infty}^2/c^2)L^{\infty}, \end{aligned} \quad (3.3.1)$$

where γ_{∞} is the Lorentz factor for u_{∞} . The second expression shows that u_{∞} essentially dictates the small variance of the $\dot{E} - \dot{M}c^2$ values in Fig.3.3.2. Indeed, the second term can be neglected since, naturally, $T_{\infty} \rightarrow 0$. In the third term, the comoving luminosity just happens to be the constant L_{Edd} , as we will see and explain in the next section. All that is left is terms of u_{∞} . Paczynski and Proszynski [1986] give the following estimate for the velocity at infinity,

$$u_{\infty}^2 \approx u_{\text{ph}}^2 - \frac{GM}{r_{\text{ph}}} \left(1 - \frac{L_{\text{ph}}}{L_{\text{cr}}} \right), \quad (3.3.2)$$

saying that past the photosphere, kinetic energy will be lost in order to escape the effective gravitational pull of the star. Fig. 3.3.3 shows u_{∞} as a function of \dot{M} according to Eq. (3.3.2). We see that it peaks in between $\dot{M} = 10^{18}$ and $10^{18.5} \text{ g s}^{-1}$, which is consistent with our Eq. (3.3.1) and Fig. 3.3.2.

Lastly, the bottom right panel of Fig. 3.3.2 shows that the base luminosity, redshifted to infinity, levels off at high \dot{M} . This is the first indication that

the high mass-loss rate models are not valid. Indeed, it is a strange and likely non-physical conclusion that by increasing the base luminosity by only a few percent, the mass-loss rate could more than triple. A possible explanation is that for these models, the wind base is too shallow at $y = 10^8 \text{ g cm}^{-2}$, and should instead be deeper into the burning layer where the luminosity could keep increasing and follow the natural progression of the L_b^∞ curve in Fig. 3.3.2. We will analyze in more detail in the next section if these high \dot{M} winds are in the same regime near the base as the others.

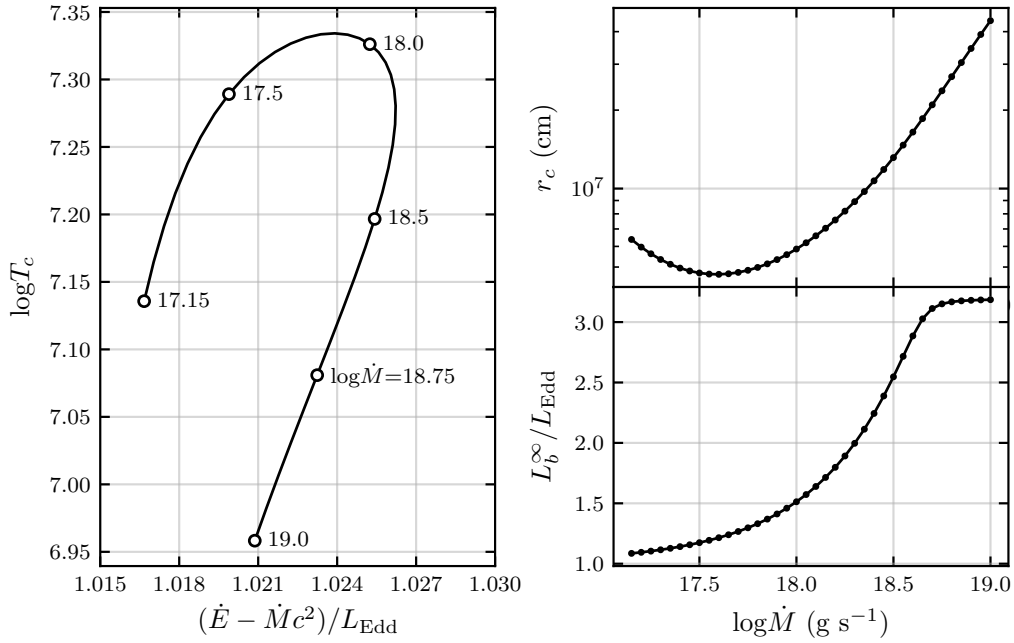


Figure 3.3.2 – Roots of the wind models. *Left*: (\dot{E}, T_c) parameter space, with sample values of $\log \dot{M}$ labelled along the root curve. *Right*: Critical point radius and base luminosity seen at infinity as a function of $\log \dot{M}$, with each dot representing one of the computed models.

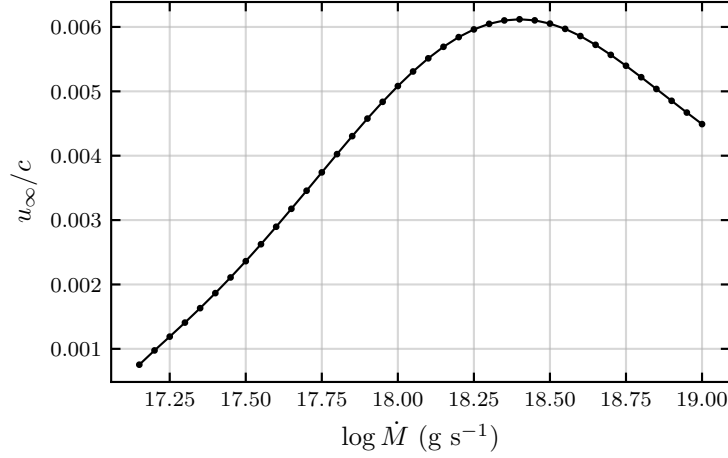


Figure 3.3.3 – Velocity at infinity according to Eq. (3.3.2).

3.4 Dependence of the wind models on \dot{M}

We calculated wind models with the method described in Section 3.2, using the roots found in Section 3.3. Figure 3.4.1 shows the radial profiles of the winds for eight \dot{M} values. In all models, the wind base $r_b = 12$ km has a high temperature and density. The inner part of the wind has very small velocities in all models. Since the sound speed scales with temperature, the mach numbers at the base are all smaller than 10^{-6} , which justifies our assumption of hydrostatic equilibrium for the inner part of the wind.

Near the surface, the flux seen at infinity is strongly super-Eddington, but rapidly decreases as the velocity increases, until it becomes only slightly higher than the Eddington luminosity (dotted line in the luminosity panel). This demonstrates how the super-Eddington flux is transferred to the gas in order to accelerate it. At large distances from the star, the gas stops being accelerated as it decouples from the radiation, and the luminosity remains just slightly super-Eddington simply through conservation of energy. This is also consistent with the fact that PRE bursts usually have a constant luminosity during the expansion phase.

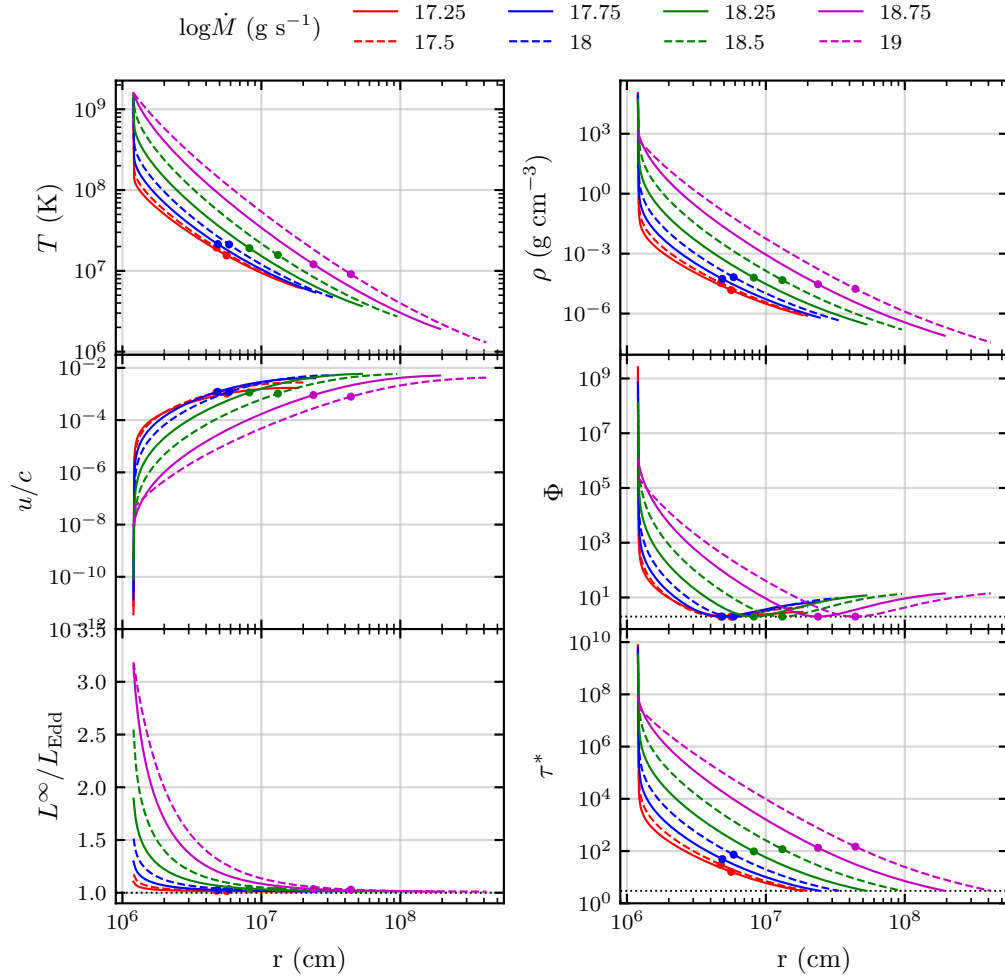


Figure 3.4.1 – Wind profiles for different \dot{M} , from the base r_b to the photosphere r_{ph} . From left to right, up to down : temperature T , density ρ , velocity u/c , velocity parameter Φ , luminosity L/L_{Edd} , optical depth parameter τ^* . The dots indicate the location of the critical point.

Since the inner part of the wind is geometrically thin, it is useful to plot certain quantities as a function of density in order to analyze it more clearly. First, as we discussed in the introduction, while the flux seen at infinity can be strongly super-Eddington at the base, the local flux can be

sub-critical, which explains the slow rise of the wind. This can clearly be seen in Fig. 3.4.2. Only the highest \dot{M} models start off nearly critical at the base, which is consistent with their higher starting velocities. Past r_c and at r_{ph} , the luminosities are less than 1% off from L_{cr} .

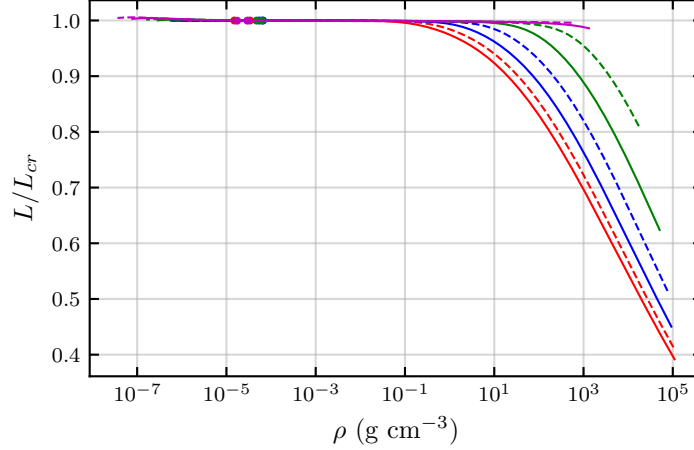


Figure 3.4.2 – Ratios of local luminosity to critical luminosity as a function of density in the wind models. The colors refer to the same legend as Fig. 3.4.1.

Figure 3.4.3 shows the temperature as a function of density. As was noted by Paczynski and Proszynski [1986], the extended regions of the winds are completely radiation pressure dominated, and they start to transition to a gas pressure dominated regime near the surface as the density increases. The highest \dot{M} models however do not transition and remain in the radiation pressure dominated regime. As these authors pointed out, this means that the specific entropy the gas, which sharply drops when going to the gas pressure dominated regime, stays at a high level for the high \dot{M} models. Too high, in fact, for any nuclear reaction network to produce enough energy to match to these wind models. Looking at Fig. 3.4.3, it is clear that the transition to the gas pressure dominated regime simply occurs at a higher density than the other models. Based on this and the discussion on L_b^∞ in the previous section, it seems that a simple solution to these high \dot{M} problems

would be to change the inner boundary condition (Eq. 3.2.9) such that the wind base be defined as having a larger column depth than 10^8 g cm^{-2} . We tried this with 10^9 g cm^{-2} , and realized that non-acceptable wind models still existed, but started at slightly larger values of \dot{M} . But for this small gain of a larger number of acceptable wind models, the assumption of a pure helium composition becomes less accurate. Indeed, past $y \sim 10^8 \text{ g cm}^{-2}$, we start to approach nuclear burning regions, where elements such as carbon are expected to be present with significant abundances. In the end, we decided to keep the original boundary condition, and simply declare our models with $\dot{M} \gtrsim 10^{18.5} \text{ g s}^{-1}$ to be physically non-acceptable².

Finally, it appears from Fig. 3.4.3 that degenerate electron corrections are not important for our wind models, even near the base. If we matched to a higher column depth as discussed in the previous paragraph, perhaps they would. So, overall, our wind models agree very well with those of Paczynski and Proszynski [1986], which validates our different numerical method and boundary conditions.

3.5 Photospheric radii and spectral shifts

In Chapter 1, we discussed a recent paper by Strohmayer et al. [2019] which found clear emission and absorption lines in four PRE bursts observed with *NICER*. The lines from the stronger bursts were systematically blueshifted relative to the ones from the weaker bursts, which the authors argued could be caused by a combination of gravitational redshift and wind velocity blueshift. Our models can be used to discuss this claim.

First, let us note that our wind models cannot reproduce the inferred photospheric radii of 72 to 103 km found by Strohmayer et al. [2019] – all of our models have $r_{\text{ph}} > 100 \text{ km}$. This suggests that the PRE phases of

²Note that Paczynski and Proszynski [1986] rejected models with $\dot{M} \geq 10^{19} \text{ g s}^{-1}$ for the same reasons. They had more acceptable models (larger \dot{M} range) because they matched to a higher temperature at the base.

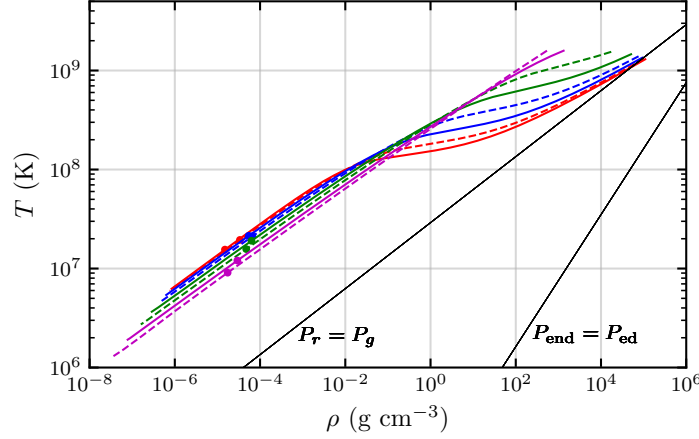


Figure 3.4.3 – Temperature-density profiles in the wind models. The colors refer to the same legend as Fig. 3.4.1. The black lines separate the space in three different pressure regimes. From left to right, pressure is dominated by radiation pressure ($P_r = aT^4/3$), non-degenerate gas pressure (P_g), and degenerate gas pressure (P_{ed}).

these bursts were not caused by a wind, but rather by a series of expanded envelopes (Chapter 4), in which case there is no blueshift. However, a caveat here is that these radii are derived from blackbody fits. It is known (e.g. Galloway and Keek [2017]) that the blackbody temperature of these fits is subject to a color correction factor $f_c \equiv T_{\text{BB}}/T_{\text{eff}}$ that can reach values as high as 2, which would make the color-corrected photospheric radius four times larger. The uncertainty around f_c , especially in the PRE case, makes it difficult to accurately determine r_{ph} from observations.

To make sure that our 100 km limit is not a consequence of the neutron star parameters, we computed other wind models with different M and R . In Fig. 3.5.1, we show the range of photospheric radii in these models as a function of the base luminosity. We see that the minimum value of r_{ph} depends mostly on M , and that even for very light neutron stars, winds have photospheres of over 100 km.

We may still investigate the behavior of spectral shifts, as a function of r

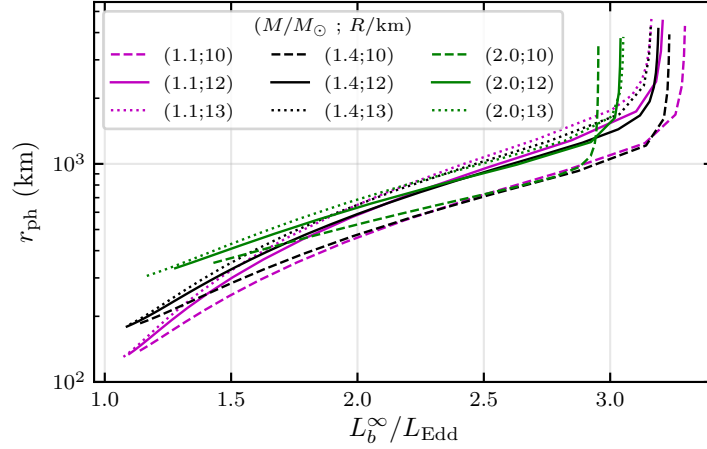


Figure 3.5.1 – Photospheric radii for different neutron star masses and radii, as a function of the base luminosity seen by observers at infinity. The solid black line corresponds to the models used throughout this thesis.

for fixed \dot{M} , and vice-versa. Redshift comes from relativistic curvature,

$$1 + \frac{\Delta\lambda_{\text{red}}}{\lambda_0} = \left(1 - \frac{r_s}{r_0}\right)^{-1/2} = \frac{1}{\zeta}, \quad (3.5.1)$$

where r_0 is the emission radius and λ_0 is the emission wavelength, while blueshift comes from the special relativistic Doppler effect,

$$1 + \frac{\Delta\lambda_{\text{blue}}}{\lambda_0} = \sqrt{\frac{1 - u_0/c}{1 + u_0/c}}, \quad (3.5.2)$$

where u_0 is the gas velocity at r_0 . In the top panel of Fig. 3.5.2, we see that redshift dominates everywhere before the critical point, where it can reach values of several percents. After the critical point and approaching the photosphere, redshift and blueshift become comparable to the point where the total spectral shift is close to zero. We can see from the bottom panel of Fig. 3.5.2 that for every wind model, the total shift at the photosphere is of less than 1%. This is not enough to produce the relative line shift of 1.046 in

Strohmayer et al. [2019]. It is interesting to note the changing sign of $\Delta\lambda$ at high \dot{M} , as both velocities and photospheric radii increase, although being able observing such small shifts is unlikely.

We must also note that there is no guarantee that the emission radius of spectral lines is at the Helium photosphere. Heavier elements that are thought to be ejected have more complex interactions with radiation, and absorption/emission lines themselves are not a continuum effect, which is how radiation is treated in our model. Our wind models can describe the relative importances of redshift and blueshift, but true predictions on spectral lines will require a more sophisticated treatment of radiative transfer.

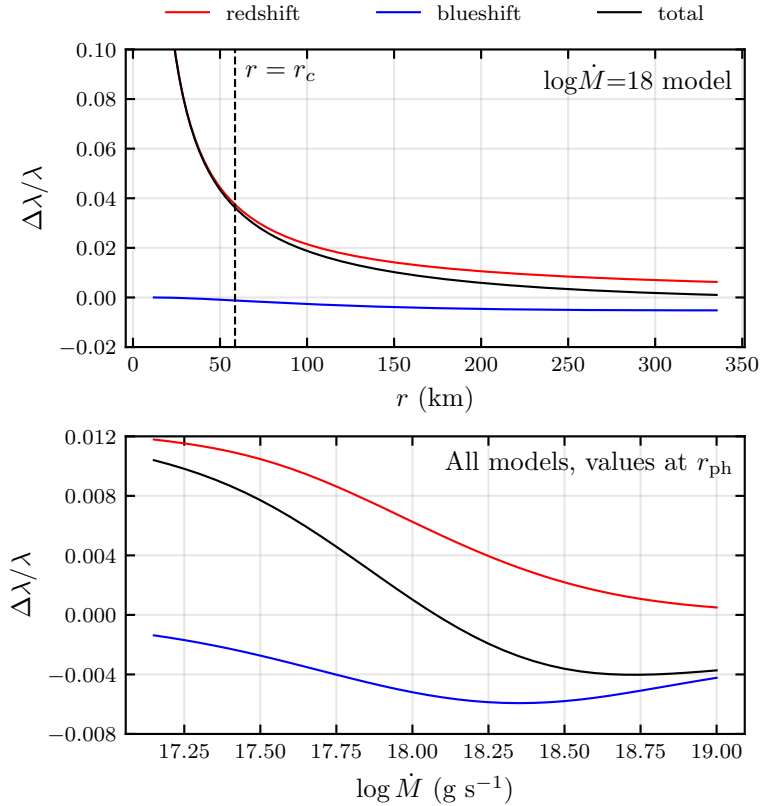


Figure 3.5.2 – Wind spectral shifts, as a function of radii for the $\log \dot{M} = 18$ model (*top*), and as a function of \dot{M} at the photosphere (*bottom*).

Chapter 4

Expanded envelopes

For the same neutron star of mass $M = 1.4M_{\odot}$ and radius $R = 12$ km, we now search for solutions to the equations of structure with $u = 0$. The resulting profiles will represent expanded static envelopes where hydrostatic balance is sustained by the luminosity. As explained in the introduction, the local luminosity is a function of redshift (Eq. 1.4.3), with the luminosity at infinity L^{∞} being a constant of each model. The other free parameter which will determine the model is the photospheric radius r_{ph} , which we will define in a slightly different way than in the wind models. The boundary condition at the surface will be the same as in the wind models, so that we will be able to link burning layer conditions to either regime.

As in the wind case, we integrate the equations of structure derived in Chapter 2. However, it is worth mentioning that in the static ($u = 0$) case, these equations can be re-written in a way that is perhaps more intuitive to

understand. Indeed, we can write

$$\frac{dP}{dr} = -\frac{GM\rho}{r^2\zeta^2} \left[1 + \left(4 - \frac{3}{2}\beta_i - \frac{3f-4}{f-1}\beta_e \right) \frac{P}{\rho c^2} \right] \quad (4.0.1)$$

$$\frac{d\rho}{dr} = \frac{\rho}{P} \frac{dP}{dr} \frac{[1 - (4 - 3\beta_i - (4 - \alpha_1)\beta_e)\nabla_{\text{rad}}]}{\beta_i + \beta_e(\alpha_1 + \alpha_2 f)} \quad (4.0.2)$$

$$\frac{dT}{dr} = \frac{T}{\rho} \frac{dP}{dr} \nabla_{\text{rad}}, \quad (4.0.3)$$

where

$$\begin{aligned} \nabla_{\text{rad}} = & \left[\frac{\zeta\kappa L_\infty}{16\pi GMc(1 - \beta_i - \beta_e)} + \frac{P}{\rho c^2} \right] \\ & \times \left[1 + \left(4 - \frac{3}{2}\beta_i - \left(\frac{3f-4}{f-1} \right) \beta_e \right) \frac{P}{\rho c^2} \right]^{-1} \end{aligned} \quad (4.0.4)$$

is the radiative gradient. In the non-degenerate limit, these equations are the same as those written by Paczynski and Anderson [1986] for an ideal gas plus radiation EOS. Eq. 4.0.1 is just the statement of hydrostatic equilibrium, with the proper GR and degenerate EOS corrections, Eq. (4.0.2) can be directly derived from Eq. (4.0.1), and Eq. 4.0.3 is another way to write the photon diffusion equation (2.3.14). Writing these equations in terms of the radiative gradient is relevant, because in order for heat to be transported by radiation rather than convection, the following condition must be respected at every point:

$$\nabla_{\text{rad}} < \nabla_{\text{ad}}, \quad (4.0.5)$$

where

$$\nabla_{\text{ad}} \equiv \left(\frac{\partial \ln T}{\partial \ln P} \right)_s \quad (4.0.6)$$

is the adiabatic gradient. The “ s ” subscript indicates a derivative with constant entropy. If ∇_{ad} becomes the smaller gradient, then the envelopes will become convective [Paczynski and Anderson, 1986]. We are ignoring convection in our model, so we must verify that Eq. (4.0.5) is true at every point

in the envelopes.

We present our numerical method for calculating envelope models in §4.1 and analyze the results in §4.2. In §4.3, we discuss the errors that can be made on the neutron star radius if one of these envelopes is present at touchdown.

4.1 Numerical integration and boundary conditions

Similar to the method used by Paczynski and Anderson [1986], we look for envelope solutions for every value of r_{ph} by setting trial values for L_{ph} , then integrate inwards to see how far the envelope base is from the neutron star surface, then adjust L_{ph} accordingly. We explain the details of this process and the method for constructing the final solution in what follows.

As explained in Chapter 1, envelopes are sustained by a luminosity that is only slightly sub-critical everywhere. We define the luminosity parameter

$$q \equiv 1 - \frac{L}{L_{\text{cr}}}, \quad (4.1.1)$$

which we expect to be very close to zero everywhere, but always positive. To find the envelope model for a given r_{ph} , we begin by adopting a trial value for $\log_{10} q_{\text{ph}}$, which we know to be between -4 and -3.5 from the work of Paczynski and Anderson [1986]. Then, we initialize the variables ρ and T based on the outer boundary condition which defines the photosphere. For temperature, we assert that $T_{\text{ph}} = T_{\text{eff}}$, just like in the wind case. This implies

$$T_{\text{ph}}^4 = \frac{L_{\text{ph}}}{4\pi r_{\text{ph}}^2 \sigma} = \frac{L_{\text{cr}}(1 - q_{\text{ph}})}{4\pi r_{\text{ph}}^2 \sigma}, \quad (4.1.2)$$

where L_{cr} itself depends on the temperature via the opacity $\kappa(T)$ (Eq. 1.4.4).

Therefore, we re-write Eq. (4.1.2),

$$0 = \kappa(T_{\text{ph}})T_{\text{ph}}^4 - \frac{GMc(1 - q_{\text{ph}})}{r_{\text{ph}}^2 \sigma} \left(1 - \frac{r_s}{r_{\text{ph}}}\right)^{-1/2}, \quad (4.1.3)$$

such that T_{ph} can be found with a simple one-dimensional root-finding algorithm. The luminosity at infinity can now be found with

$$L^\infty = L_{\text{Edd}} \frac{\kappa_0}{\kappa(T_{\text{ph}})} (1 - q_{\text{ph}}) \left(1 - \frac{r_s}{r_{\text{ph}}}\right)^{1/2} \quad (4.1.4)$$

To find the initial density, we start by making use of the fact that $u = du/dr = 0$ to re-write the initial momentum equation,

$$\omega_g \frac{d \ln \Psi}{dr} + P'_g - \frac{1}{c\Psi} \rho \kappa F = 0, \quad (4.1.5)$$

as

$$\frac{dP_g}{dr} = -\frac{g\rho}{\zeta} \left(1 + \frac{5}{2} \frac{kT}{\mu m_p c^2} - \frac{L}{L_{\text{cr}}}\right), \quad (4.1.6)$$

where we used the ideal gas EOS for ω_g , since degenerate corrections will not matter near the photosphere. In any case, we can neglect the gas term since $kT/m_p \ll c^2$. Further, we can use the differential form of the definition for the true optical depth (Eq. 3.2.2),

$$d\tau = -\rho \kappa \frac{dr}{\zeta}, \quad (4.1.7)$$

in order to finally rewrite the pressure gradient as ¹

$$\frac{dP_g}{d\tau} = \frac{gq}{\kappa}. \quad (4.1.8)$$

We can integrate this equation from infinity ($\tau = 0$) until the photosphere.

¹Do note that Eq. (4.1.8) is only valid under the approximations of hydrostatic equilibrium and negligible gas pressure.

This time, we can set a boundary value for the true optical depth, instead of τ^* like in the wind case. For stellar grey atmospheres, the value $\tau = 2/3$ defines the photosphere when the Eddington approximation² is taken [Mihalas, 1978]. Assuming zero gas pressure at infinity and that L, L_{cr} and κ are approximately constant everywhere beyond $\tau = 2/3$, we get the condition for the density at the photosphere:

$$\rho_{\text{ph}} = \frac{2}{3} \frac{gq}{\kappa(T_{\text{ph}})} \frac{\mu m_p}{k T_{\text{ph}}} . \quad (4.1.9)$$

This boundary condition given by equations (4.1.2) and (4.1.9) was also used by Paczynski and Anderson [1986].

We integrate T and ρ from these initial values using equations (2.5.9) and (2.5.8), and stop once we hit the base radius $r_b = r(y = P/g = 10^8)$. The inner boundary condition for matching to the surface,

$$r_b = R , \quad (4.1.10)$$

is the same as in the wind case. Ideally, we would simply iterate on q_{ph} until Eq. (4.1.10) is satisfied. However, we found that this was not generally possible, as it would require us to increase the number of digits of q_{ph} and decrease the numerical routine tolerances beyond reasonable. In other words, there does exist an exact value of q_{ph} that results in an envelope which follows the inner boundary condition Eq. (4.1.10), but calculating this envelope from a simple shooting method is not feasible numerically. Instead, we proceed with a stepwise bisection-like method. First, we find two nearby values of q_{ph} for which the inwards integrations land on either side of the stellar radius, i.e., one has $r_b < R$ and the other has $r_b > R$. This way, we know the “true” value of q_{ph} to be in between these two values. Then, we identify the first point of divergence in the integration, i.e., where the values of T or ρ of the

²Radiation pressure equals a third of the radiation energy density. We already made use of this approximation in Chapter 2.

two envelopes differ by more than the chosen relative tolerance of 10^{-4} . At this point, we interpolate the values for the two variables (take the middle value) to initialize a new envelope, which is bound by the initial two envelopes in both ρ and T . We look at which side of R this new envelope lands, and discard the initial envelope which lands on that same side. We then repeat the interpolation procedure at the next point of divergence, and so on until we have a solution which satisfies the boundary condition. Fig. 4.1.1 shows a visual demonstration of our method.

After having constructed an envelope, we verified that we had truly found a solution to the equations of structure by interpolating a polynomial and comparing its derivatives at every r to the ones prescribed by equations (2.5.9) and (2.5.8).

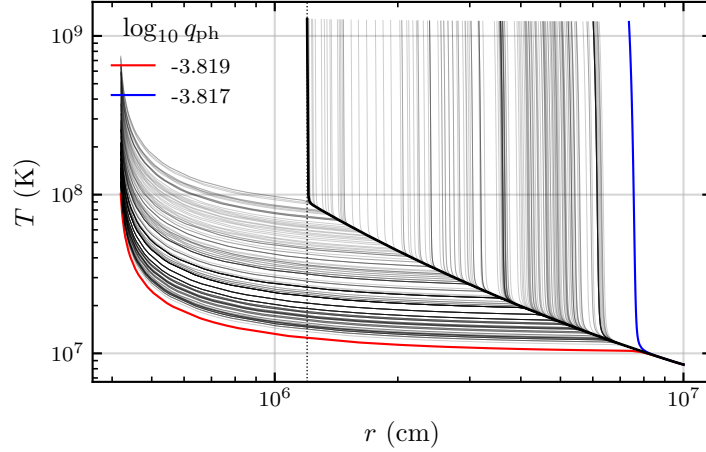


Figure 4.1.1 – Method for finding envelope solutions. Shown is a demonstration of the $r_{\text{ph}} = 100$ km envelope. The blue and red lines are the two initial solutions, the thick black line is the final solution. The thin black lines are the intermediate solutions which start at every point of divergence in the inwards integration. The dashed vertical line marks the $r = R$ line. See text for more details.

4.2 Dependence of the envelope models on r_{ph}

We calculated envelope models with the method described in the previous sections for very small photospheric radii just above the neutron star radius, all the way to very large values in the hundreds to one thousand kilometres. Fig. 4.2.1 shows radial profiles of the temperature, density, and luminosity parameter q for eight different envelope models. Just like in the wind case, most the the mass is stored in a compact region of only a few kilometres above the surface. After a drop in temperature and density of several orders of magnitude, the envelope transitions to an extended region which is still in hydrostatic equilibrium and can span hundreds of km. The bottom panel of Fig. 4.2.1 confirms the statement made in section 1.4 that $L \lesssim L_{\text{cr}}$ at every r . This allows for a significant reduction of the effective gravity, allowing large expansion, while preventing outflows, thus maintaining equilibrium.

Figure 4.2.2 shows the temperature profiles as a function of density. All envelopes transition to the same radiation-dominated regime at low density. As was noted by Paczynski and Anderson [1986], this final state is independent of the base temperature. The envelopes are gas pressure dominated at the base, but they are too hot to be dominated by degenerate electrons. It is interesting to note that even with sub-Eddington luminosities, bursts can easily generate large enough temperatures to lift all degeneracies, at least at the depths with which we are concerned. It is easy to see that the degenerate regime could be reached by extending the curves in Fig. 4.2.2 to larger densities.

As was mentioned at the beginning of this chapter, we need to make sure that these envelopes are not convective, by verifying that $\nabla_{\text{rad}} < \nabla_{\text{ad}}$ everywhere. Since we found that degenerate electron corrections were not important, we can take the ideal gas plus radiation equation of state for the adiabatic gradient, for which the expression

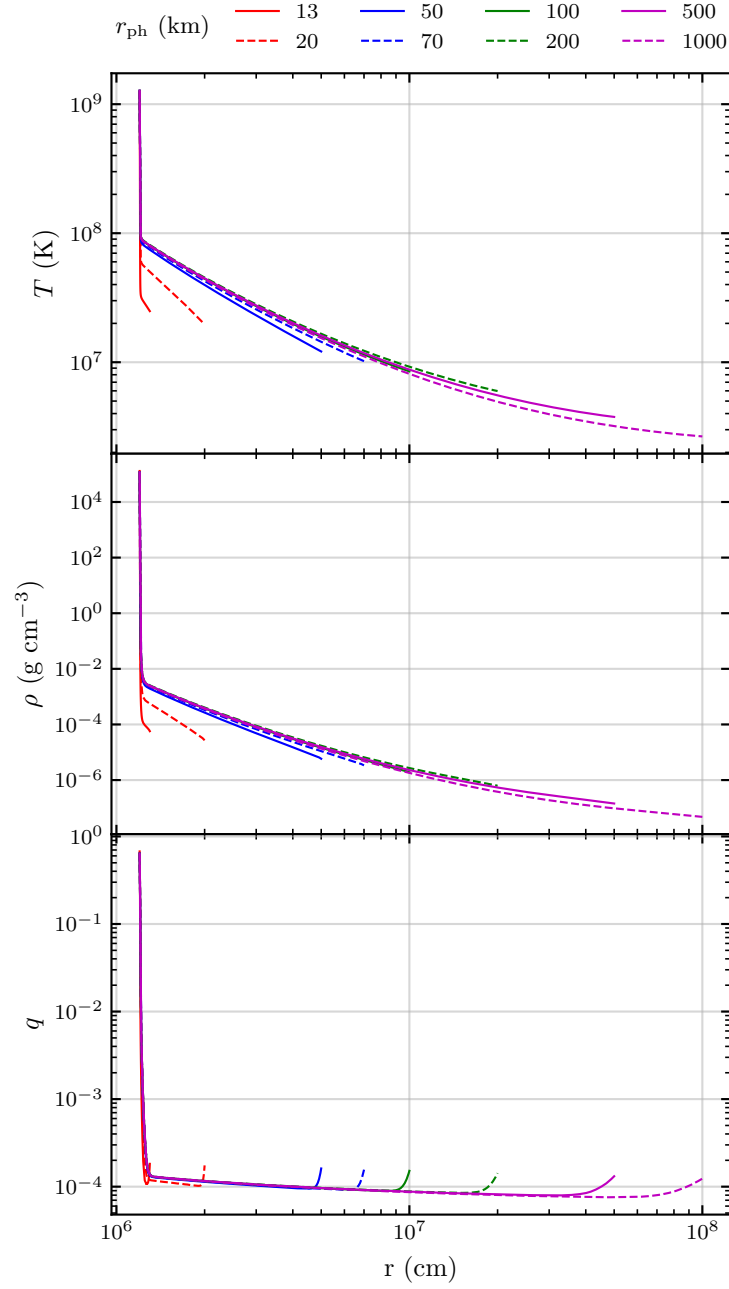


Figure 4.2.1 – Envelopes profiles from the base r_b to the photosphere r_{ph} . Top to bottom: temperature, density, luminosity parameter q (Eq. 4.1.1)

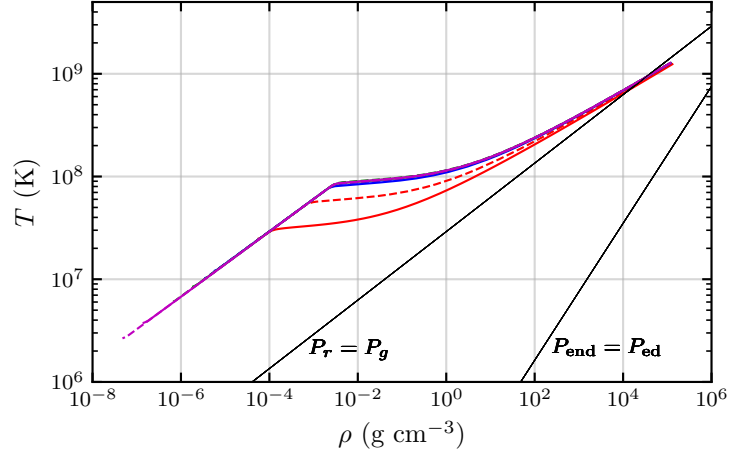


Figure 4.2.2 – Temperature-density profiles for the envelope. The colors refer to the same legend as Fig. 4.2.1. The black lines are explained in the caption of Fig. 3.4.3.

$$\nabla_{\text{ad}} = \frac{8 - 6\beta}{32 - 24\beta - 3\beta^2} \quad (4.2.1)$$

is given in Hansen and Kawaler [1994]. Fig. 4.2.3 demonstrates that our models are indeed radiative everywhere. However, it does appear that the extended regions of the envelopes are right on the verge of becoming convective, as the radiative gradient is only very slightly smaller than the adiabatic gradient. It could be relevant that the profiles of $1 - \nabla_{\text{rad}}/\nabla_{\text{ad}}$ are similar to those of q , meaning the critical luminosity could be related to the onset of convection. There have been studies in the past of the relation between L , L_{cr} and radiative and convective regimes in stellar interiors (e.g. Joss et al. [1973]). The X-ray burst scenario is different in many ways to stellar interiors; in particular, we know from the work of Paczynski and Anderson [1986] that general relativistic corrections to the critical luminosity are important for allowing very extended solutions. This warrants more investigation into the stability of our radiative envelope solutions, but is beyond the scope of this work.

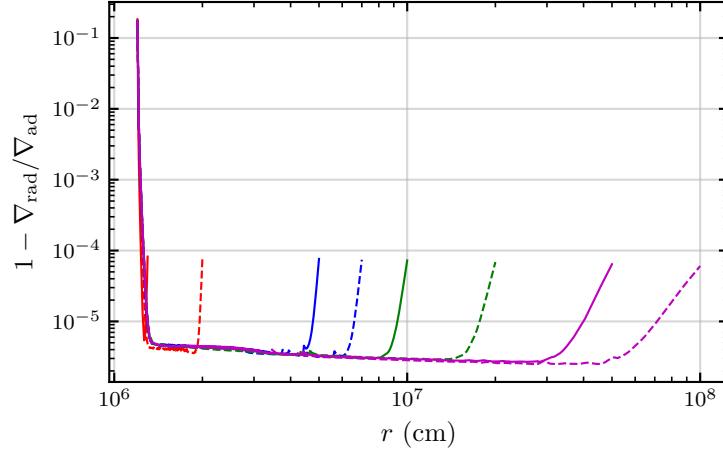


Figure 4.2.3 – Ratio of radiative gradient (Eq. 4.0.4) to adiabatic gradient (Eq. 4.2.1).

Lastly, we discuss our results for the main observable, L^∞ for these envelope models, which is shown as a function of r_{ph} in Fig. 4.2.4. Whereas Paczynski and Anderson [1986] found that their envelope models had $0.7 < L^\infty/L_{\text{Edd}} < 1$, our models have $0.85 < L^\infty/L_{\text{Edd}} \lesssim 1.02$. Indeed, the most extended photospheres are in fact slightly super-Eddington, even if no wind is driven, though only by a few percent. This can be explained by looking at Eq. (4.1.4), which shows that L^∞/L_{Edd} is determined by three factors of order unity: the opacity ratio, luminosity parameter and redshift, all taken at the photosphere. Paczynski and Anderson [1986] incorrectly took the first two factors as being equal to unity, saying that $\kappa \approx \kappa_0$ and $L \approx L_{\text{cr}}$ at the photosphere, such that the redshift is the only parameter which determines L^∞ . These are, of course, sensible approximations in a general sense. However, in the context of Eq. (4.1.4), they result in missing some subtlety. For small r_{ph} , the temperature is large enough (see Fig. 4.2.1) that $\kappa(T_{\text{ph}})$ is significantly smaller than κ_0 – this explains our lower bound of 0.85 on L^∞/L_{Edd} , instead of Paczynski and Anderson’s 0.7. For large r_{ph} , the redshift term is very small, and so is $1 - q_{\text{ph}}$, as shown by the blue curve in Fig. 4.2.4.

While T_{ph} is smaller than in the small r_{ph} models, it is still large enough that the opacity ratio can “win” over the other two, resulting in super-Eddington luminosities. These are important details as they change our interpretation of the observations. To our knowledge, the fact that super-Eddington luminosities can lead to static, non-outflowing, envelopes³ has not been discussed in the literature before.

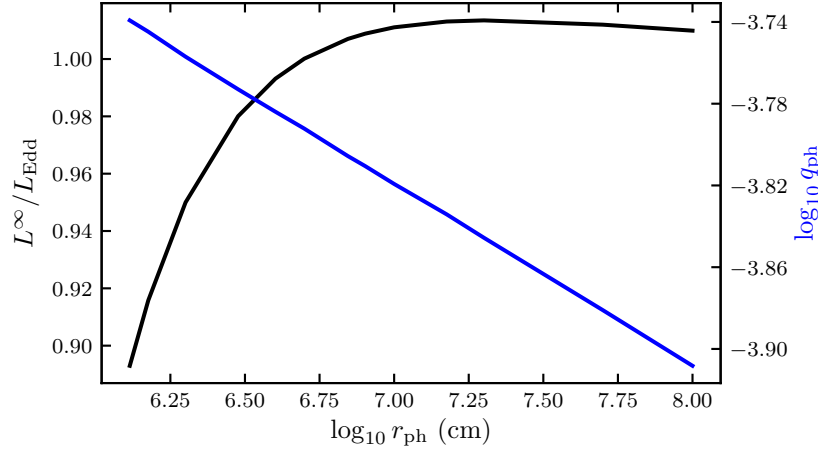


Figure 4.2.4 – Luminosity parameters for all envelope models labelled by r_{ph} . Left axis, black line: luminosity at infinity, Eddington normalized. Right axis, blue line: luminosity parameter q at the photosphere.

4.3 Compact envelopes and touchdown radius

We discussed in Chapter 1 the common technique of finding the neutron star radius based on the touchdown radius, i.e. the blackbody radius when the temperature peaks and the photosphere presumably touches back down to

³We have only shown that static envelopes with slightly super-Eddington luminosities and very large photospheres are possible in theory, at least under the set of approximations (spherically symmetric, optically thick) that we made. Whether or not these can actually be formed during Type I X-ray bursts is a separate question, which we will discuss in the next chapter.

the surface following the PRE phase of the burst. But if the luminosity at the touchdown point is still near-Eddington, we have shown in this chapter that an expanded envelope could be present, which means that the photospheric (touchdown) radius is not the neutron star radius. We investigate in this section how important this error might be based on the observed parameters. To do this, we have extended our calculation of envelopes to very compact ones with photospheres less than 1 km above the neutron star surface.

The top panel of Fig. 4.3.1 shows that the range of luminosities that would cause a significant difference between the touchdown and neutron star radius (say more than 100 m) is quite narrow, from $\sim 0.85L_{\text{Edd}}$ to $\gtrsim L_{\text{Edd}}$, but not inconceivable. Notice also that this problem only appears when factoring in general relativity, as Newtonian envelopes can only be very compact. In the bottom panel, if we look at T_{eff} , the effective temperature of the envelope (redshifted to infinity with $T^\infty = \zeta T$), we see that the peak of the temperature curve is very flat along r_{ph} . This means there is automatically uncertainty in the touchdown radius when inferring it from the temperature. For example, if the measured peak temperature is of 1.8 ± 0.1 keV (an uncertainty of 5%, which is generous if we look back to the errorbars in Fig. 1.2.1), then Fig. 4.3.1 shows that the photospheric radius could be anywhere from just a few tens of meters to kilometres above the stellar surface. These results should motivate a more careful examination of the neutron star radii determined using the touchdown point.

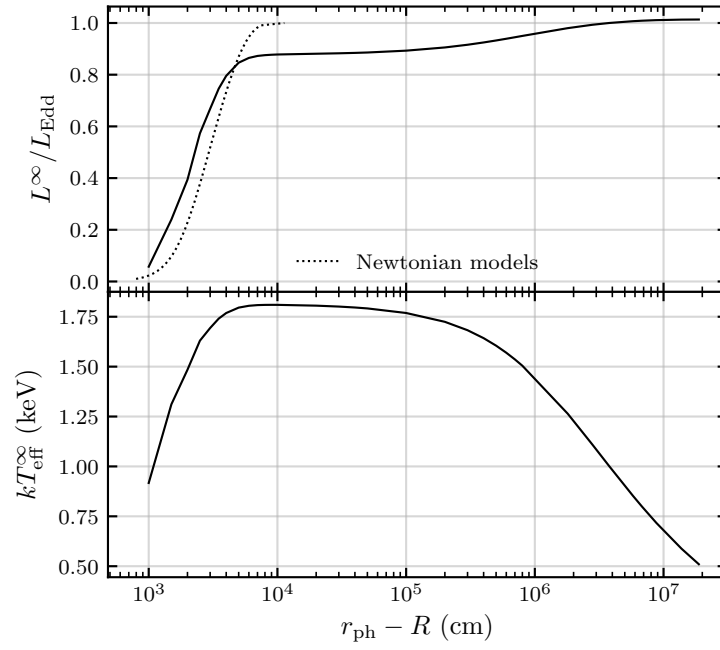


Figure 4.3.1 – Difference between the photospheric (touchdown) radius based on the luminosity (*top*) and observed effective temperature (*bottom*). The dotted line in the top panel represents Newtonian atmospheres, for which we derive an analytical formula in Appendix C.

Chapter 5

The stationary solution space

In this final chapter, we take the solutions for wind and expanded envelopes from the previous two chapters and combine them to analyze the total solution space of PRE bursts. We are interested in the qualitative differences between the profiles of the solutions (§5.1), and quantitative differences in the observables, mainly the luminosities and photospheric radii. In §5.2, we establish timescales for the solutions to determine if steady-state solutions are truly appropriate for describing the evolution of PRE bursts. We conclude in §5.3 by analyzing how the different definitions for the photosphere for winds and envelopes might affect our results.

5.1 Profiles

While we have already shown radial profiles of winds in Chapter 3 and envelopes Chapter 4, it is instructive to plot some of them together to analyze the general differences between the two regimes.

In Fig. 5.1.1, we show the temperature and density profiles for a few wind and envelope models. Close to the surface, the sharp drop in temperature is associated to a drop density in both regimes. This region corresponds to a thin layer in hydrostatic equilibrium, even in the winds where the velocities

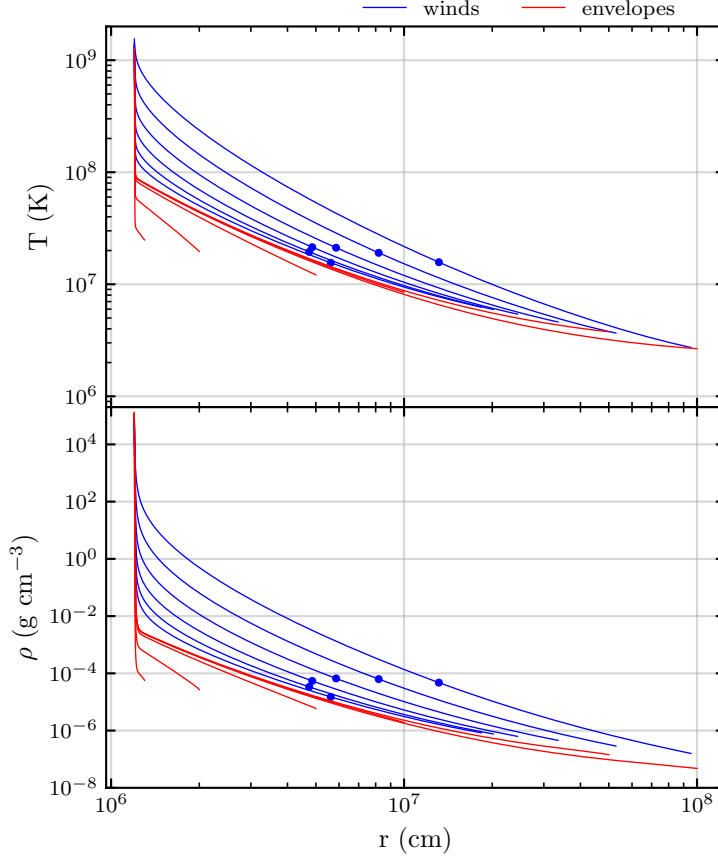


Figure 5.1.1 – Temperature and density radial profiles for wind and envelope models. Dots indicate the position of the wind critical points. The mass-loss rates for the winds are $\log \dot{M} = 19.0, 18.5, 18.0, 17.5 \text{ g s}^{-1}$, and the photospheric radii for the envelopes are $r_{\text{ph}} = 13, 20, 50, 100, 500, 1000 \text{ km}$.

are initially very low. This suggests a natural transition mechanism between the two regimes. At the onset of the burst, while the luminosity is rising towards the L_{Edd} , the envelope could expand hydrostatically, and only start to outflow from the upper layers as L_b^∞ eventually crosses L_{Edd} , pushing the photosphere from tens to hundreds of km. The opposite could happen at

the end of the PRE phase of the burst, where the wind could eject its upper layers before dying out, leaving behind the still-expanded static envelope.

We can also see in Fig. 5.1.1 that there are degeneracies between the static envelope and outflowing wind cases in terms of the radius of the photosphere and its temperature. For instance, the $\dot{M} = 10^{18.5} \text{ g s}^{-1}$ wind and $r_{\text{ph}} = 1000 \text{ km}$ envelope have photospheres at similar radii and temperatures (but different densities). This suggests that there could be confusion from an observer's standpoint on which expansion regime is truly being observed. However, we will show later in this chapter that the timescales of these very extended envelopes and the narrow range of base luminosities that produce them make them unlikely to form during bursts.

Figure 5.1.2 shows the solution space in the density-temperature space. We have already analyzed these thoroughly in previous chapters, but it is interesting to note that the transition to a gas pressure dominated regime happens at much smaller densities for the envelopes than for the winds. This can be explained by the smaller luminosity, requiring a bigger contribution from the gas in order to hold up the envelope.

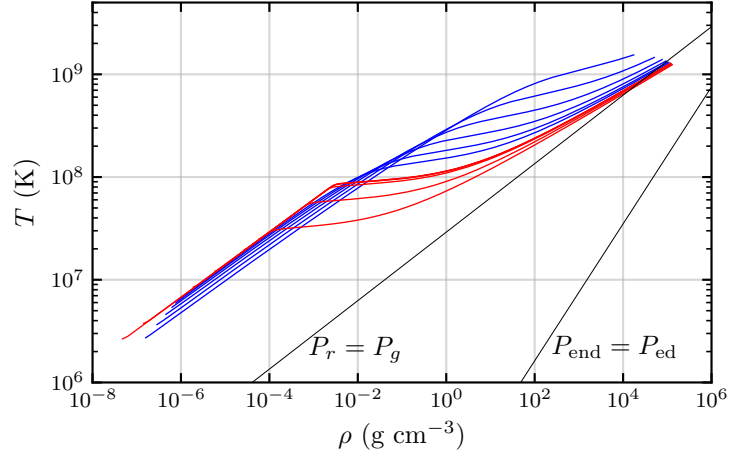


Figure 5.1.2 – Temperature-density profiles for wind and envelope models. The models are the same as in Fig. 5.1.1

5.2 Base luminosity

This section revolves around Fig. 5.2.1, which is the main result of this work. By looking at various quantities from both regimes as a function of the base luminosity, we can assess the transition between the both regimes more clearly, as it is this parameter which connects the evolution of the burning layer throughout the burst to the extended structures.

In the first panel, we plot the base temperature. As a reminder, this *base* is defined in the same way for both winds and envelopes, where a fixed column depth (or equivalently pressure) is set at the stellar radius. In this way, we are truly comparing the state of the base at the same point. We see that the envelopes only represent a tiny portion of the flux-temperature profile at the base. There is also a gap in flux between the two regimes. For reasons that were explained in Chapter 3, we were not able to compute wind models with mass-loss rates lower than $10^{17.15} \text{ g s}^{-1}$. But looking at the behavior of the curves, it is natural to think that if we were able to improve our numerical method, then the envelope and wind models would join up smoothly at the base. In fact, this is completely expected, since the base is in hydrostatic equilibrium in both regimes, so that the flux-temperature profile is essentially just a direct consequence of the chosen EOS. Lastly, we see that winds with high mass-loss rates approach the radiation temperature limit, which is the temperature for which all of the pressure, a constant $P = gy$ because of the boundary condition 3.2.9, is equal to the radiation pressure $U_R/3$, meaning that the gas is in a completely radiation pressure dominated regime. This temperature can be written as

$$T_{\text{rad}} = 1.5 \times 10^9 \text{ K} \left(\frac{M}{1.4M_{\odot}} \right)^{1/4} \left(\frac{R}{12 \text{ km}} \right)^{-1/2} \left(\frac{y}{10^8 \text{ g cm}^{-2}} \right)^{1/4} \left[1 - 0.35 \left(\frac{M}{1.4M_{\odot}} \right) \left(\frac{12 \text{ km}}{R} \right) \right]^{-1/8}, \quad (5.2.1)$$

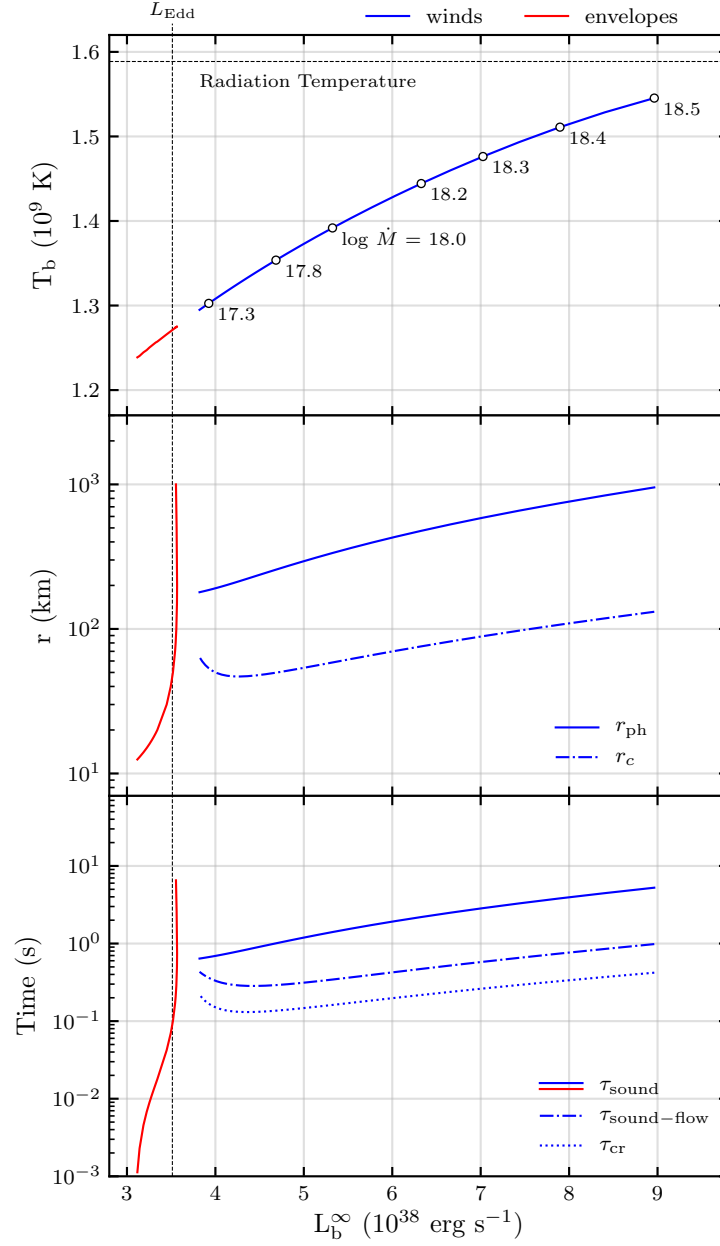


Figure 5.2.1 – Solution space for the base luminosity as seen by observers at infinity, for both winds (blue) and envelopes (red). Eddington luminosity is marked by the vertical black dashed line. *Top*: Temperature at the base. Mass-loss rates are indicated at various points for the winds. *Middle*: Photospheric and critical point radii. *Bottom*: Characteristic timescales of the solutions from the base to the photosphere (see text).

where y is the chosen fixed column depth at the base of the wind. This shows that the radiation temperature is not very high in this context, and that any calculation of wind models is bound to approach this limit at high \dot{M} , even with different neutron star parameters or inner boundary condition.

While the static to outflowing transition seems to be smooth when looking at the base, it clearly is not if we study the extended regions, and in particular the photosphere, as can be seen in the second panel of Fig. 5.2.1. Indeed, there is a clear discontinuity just above L_{Edd} , since envelope models with near-Eddington luminosities shoot up in terms of photospheric radius, instead of leveling off to the values of low \dot{M} wind models. This indicates that it is not possible to transition from one regime to the other in a quasi-static way, i.e by going from one stationary solution to the other when changing the base flux. While both regimes may exist for some time if the base flux remains close to constant, the transition can only be modelled by fully time-dependent hydrodynamical calculations.

Furthermore, while our models are all analytic solutions to stationary equations, we must ensure that the luminosity evolves slowly enough that the system is in fact able to reach a steady-state, and progress from one solution to the next. We look at characteristic timescales in the third panel of figure 5.2.1 to determine if this could be the case. The natural timescale for static structures is the sound crossing time

$$\tau_{\text{sound}} = \int_R^{r_{\text{ph}}} c_s^{-1} dr, \quad (5.2.2)$$

which gives the time taken for a sound wave to travel the structure, from the base to the photosphere. For winds, other natural timescales are the sound crossing time for one critical point

$$\tau_{\text{cr}} = \frac{r_c}{c_s(r_c)}, \quad (5.2.3)$$

and the flow crossing time

$$\tau_{\text{flow}} = \int_R^{r_{\text{ph}}} u^{-1} dr. \quad (5.2.4)$$

The problem with the latter is that the velocity is so small near the surface that the flow time is dominated by these regions, and therefore not representative of the whole solution. Instead, we take a timescale that combines the sound crossing time of hydrostatic regions, up to the critical point, followed by the flow crossing time in the outflowing regions of the wind, up to the photosphere:

$$\tau_{\text{sound-flow}} = \int_R^{r_c} c_s^{-1} dr + \int_{r_c}^{r_{\text{ph}}} u^{-1} dr. \quad (5.2.5)$$

Fig. 5.2.1 shows that these wind timescales have similar values and progressions with L_b , except for low mass-loss rates where the increase in critical point radii results in larger crossing times.

In every model, by looking at the bottom two panels in Fig. 5.2.1, it is clear that it is the photospheric radius which largely dictates the timescales. This means that more extended structures take longer to form, and that they cannot exist under a rapidly varying luminosity. Typical bursts have a rising phase of ~ 1 s, a super-Eddington or PRE phase of ~ 10 s and a decaying phase of ~ 1 min. Since the rising phase is so fast in transitioning from sub to super-Eddington luminosities, it is clear that our stationary solutions are not appropriate for describing its dynamics. However, the timescales would allow for PRE and decaying phase to be reasonably be modelled by stationary winds and envelopes respectively, except for the transition from super to sub-Eddington luminosities in the decay. Finally, the largest static atmospheres with slightly super-Eddington fluxes are unlikely to occur, or at least to remain stable, as their timescales are very long.

We have established that the transition between the static envelope and wind regimes is fundamentally time-dependent due to the r_{ph} discontinuity. We can gain more insight into this transition by examining the total amount

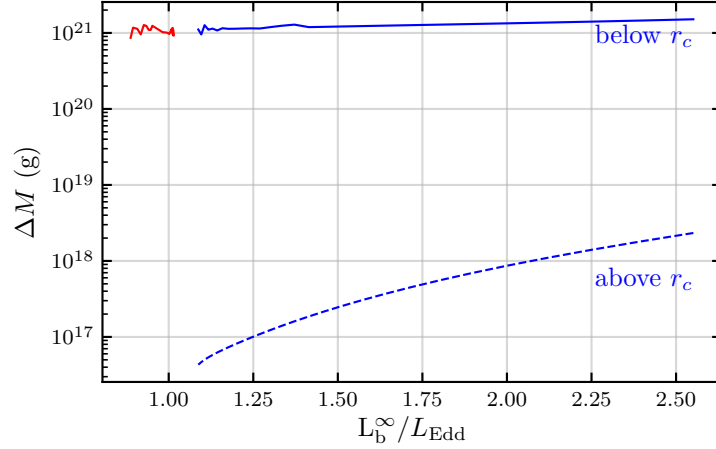


Figure 5.2.2 – Amount of mass stored in the envelopes (red) and the winds (blue), as a function of the base luminosity. For winds, we show the mass below (solid) and above (dashed) the critical point separately. The wiggle of the curves can be attributed to numerical interpolation & integration errors.

of mass stored in these solutions, which we calculate with

$$\Delta M = 4\pi \int \rho(r) r^2 dr, \quad (5.2.6)$$

to which we apply the appropriate integration bounds, e.g. r_b and r_{ph} to get the total amount of mass in the envelope/wind. Fig. 5.2.2 shows that the mass stored in the envelopes is nearly constant, which is expected since the boundary condition at the surface forces a specific column depth, a proxy for the total mass. This transitions smoothly into the winds, where the same mass remains stored in the quasi-hydrostatic regions below the critical point, while only a fraction of it is located between r_c and r_{ph} . The values of ΔM above r_c are in the same range as those of \dot{M} , which means that these extended regions are being fully replenished by fresh gas roughly every second, which is consistent with the wind timescales discussed previously.

5.3 On the definition of the photosphere

A limitation of our work is the pure optically thick approximation. While this approach, which consists of transporting heat under a diffusion equation (Eq. 2.3.14), is completely valid in the inner layers of the extended structures, it becomes less so as we approach regions of low densities and temperatures, where the photons are no longer scattering purely isotropically but are instead, on average, increasingly beamed outwards. This is why we do not integrate our models past the photosphere, where the gas is becoming optically thin. In a pure optically thick treatment of radiation, this photosphere is hard to define. For expanded envelopes, hydrostatic equilibrium allows us to define a precise photosphere with a commonly used optical depth $\tau = 2/3$. However in the outflowing wind case, we must resort to using a proxy for the true optical depth.

In this work, we followed Paczynski and Proszynski [1986] by using the optical depth parameter value $\tau^* = \kappa \rho r = 3$ to define the wind photosphere. Since we are making direct comparisons of the photospheric radii for the two regimes in Fig. 5.2.1, we must ask whether or not these different definitions of photospheres are similar to each other. We cannot compute the location of $\tau = 2/3$ in the wind models, but we can calculate τ^* in the envelopes, which we show in Fig. 5.3.1. The first thing we notice is the important difference between the most compact envelopes and the most extended ones. The compact envelopes have τ^* values larger than 3 at the photosphere. The extended ones have very small values of τ^* , even before the photosphere, which calls into question the validity of the optically thick approximation for these models. In any case, we already determined that these models were unlikely to be stable and exist in bursts, with their sound crossing times being so long.

For the compact envelope models that are likely to exist at some point before or after the PRE phase, Fig. 5.3.1 suggests that their photosphere, should the wind definition be taken instead of $\tau = 2/3$, would be slightly

larger than indicated in Fig. 5.2.1. However, this would not change the fact that the transition between the two regimes is not smooth at the photosphere, and our conclusion that the transition is time-dependent remains valid.

With Fig. 5.3.1 showing that there is a considerable difference between τ and τ^* at the photosphere, there is a concern that the photospheres for some (or all) wind models is incorrectly defined. The only way to verify and fix this would be to add a transition to optically thin in our model and calculate new winds.

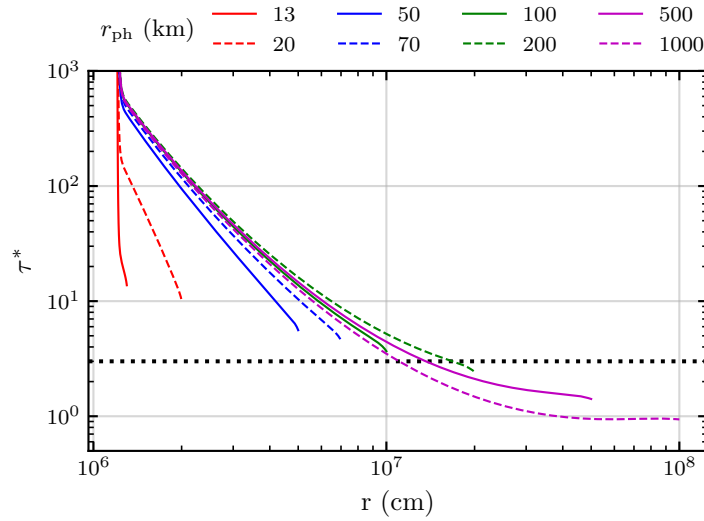


Figure 5.3.1 – The optical depth parameter as a function of radius in the envelope models. The dotted black line marks the $\tau^* = 3$ value used to define the wind photospheres.

Chapter 6

Summary and conclusions

We constructed a sequence of fully consistent static expanded envelopes and winds resulting from near or super-Eddington luminosities in X-ray bursts. We considered a neutron star with a mass of $1.4M_{\odot}$ and radius of 12 km, and pure helium composition. These and other parameters relating to the base and photospheric boundary conditions can easily be changed to calculate new models, with the codes made publicly available on *Github*¹.

For winds (Chapter 3), we found that high mass-loss rate models were bound to reach a limit where the solution is radiation pressure dominated at the base. For our parameters, this happened at $\dot{M} \gtrsim 10^{18.5} \text{ g s}^{-1}$. We rejected these models because they could not be properly matched to the static burning layer. The remaining models still cover a wide range of base luminosities redshifted to infinity, of $\sim L_{\text{Edd}}$ to $\sim 2.5L_{\text{Edd}}$. In all cases, the excess luminosity is completely transferred to the gas in order to accelerate it and escape the gravitational attraction of the star, such that every model is only slightly super-Eddington at the photosphere. This is in line with what is usually assumed by observers for PRE bursts. We found that the photospheric radii of these wind models was always large (over 100 km),

¹<https://github.com/simonguichandut/GR-wind>
<https://github.com/simonguichandut/GR-envelope>

even for neutron stars with different masses and radii. According to this, the bursts from 4U 1820-30 presented by Strohmayer et al. [2019] and discussed in Chapter 1 had PRE phases driven static envelopes and not winds. It would be interesting to verify if this result holds in multi-dimensional calculations, since factors such as rotation and ignition asymmetry could make the photospheric radius dependent on angle. We also looked at spectral shift and determined that, although small, blueshifts from wind velocities could completely counteract gravitational redshift at large radii, making the total shift of the line nearly zero. We do not expect spectral shifts larger than 1%, which cannot reproduce the relative line shift result of over 4% in Strohmayer et al. [2019]. A possible explanation is that absorption and emission lines are produced earlier than the continuum photosphere, something that can only be properly accounted for by models with detailed, frequency-dependent radiative transfer.

For envelopes (Chapter 4), we found that the luminosity was only slightly sub-critical in the extended region of every model, indicating a fragile balance between gravity and radiation pressure for these envelopes to remain static. This could be related to the fact that these regions are nearly convective. We found that very extended models, with photospheric radii of $\sim 100 - 1000$ km, have slightly super-Eddington luminosities, showing that these luminosities do not automatically imply outflows. Lastly, we showed that the method of using the PRE touchdown radius to infer the neutron star radius was prone to errors of hundreds of meters or more if the luminosity is large enough at touchdown and an expanded envelope is still present.

In comparing the two radius expansion regimes (Chapter 5), it is clear that envelopes and winds are in the same hydrostatic regime near the surface, an expected result for using the same equation of state. However, the transition in the extended zones is discontinuous, which is evident from the photospheric radii profiles in Fig. 5.2.1. Thus, the transition from sub to super-Eddington in the burst rise, and vice-versa in the burst decay, cannot

be properly modelled quasi-statically, i.e. with stationary solutions; time-dependent calculations are required. However, the timescales for the compact envelopes and the winds are small enough that these models can be used to interpret data during and after the PRE phase of the burst. One clear improvement that could be made is the implementation an optically thick to thin transition in the wind models, as the definition of the photosphere in a pure optically thick model is imprecise. At the moment of writing this thesis, this is something that we are working on and plan to publish in the near future.

Our takeaway from this work is that these burst expansion regimes, which are to this day relatively unexplored in the literature, still have many aspects that are not well understood, and that there are many caveats in using them to interpret burst observations. There needs to be more work done to improve these models and understand their properties better. The most pressing issue is to do time-dependent, general relativistic simulations of high luminosity bursts in order to understand the transition from static envelopes to winds, and vice-versa. These could then be connected to a stellar evolution code in order to follow the evolving composition of the outflows and predict spectral line effects. This was done by Yu and Weinberg [2018], but with only one set of burst parameters and without general relativity which is, as it turns out, a crucial aspect of this problem. Then, this problem should eventually be studied with multi-dimensional simulations to see the impact of effects such as rotation, magnetic fields and ignition asymmetry on the observational signature of these bursts. In Table 6.1, we summarize what constitutes, in our view, the most important improvements that must be made to burst models in order to properly answer questions about photospheric radius expansion, including those discussed in Chapter 1. These improvements will be the primary focus of my (*the author's*) doctorate research project, set to begin in September 2020.

Table 6.1 – Future work

Model Improvements	Plans
Steady-state models of this thesis, with the addition of a transition to optically thin for a more consistent description of the photosphere	To be submitted to scientific journal in 2020
Time-dependent simulations (1D) and coupling to stellar evolution code <i>Objective:</i> To understand the transition from atmospheres to winds and study the ejection of heavy elements.	Short term (PhD priority)
Multi-dimensional simulations <i>Objective:</i> To understand the impact of rotation, magnetic fields and ignition asymmetry.	Long term

Let us close on the note that the equations for radiation hydrodynamics derived in Chapter 2 (and Appendix D), and the numerical methods presented in chapters 3-4 can be used to model other astrophysical phenomena in which high luminosities drive stellar outflows. In particular, classical novae are thermonuclear bursts on accreting white dwarfs that result in bright X-ray flashes, very similar to X-ray bursts. Super-Eddington luminosities are attained as well, resulting in mass ejection from optically thick winds [Kato, 1983a]. But in these events, 10 to 90% of the accreted mass can be ejected [Lewin and van der Klis, 2006], much more than in the neutron star case where the strong surface gravity allows no more than $\sim 1\%$ to be unbinded. As a result, classical novae are very different observationally, mainly due to the fact the X-ray flash lasts for months rather than minutes. Nevertheless, the radiation hydrodynamics principles are the same, which should motivate collaboration between theorists in both fields.

Appendices

Appendix A

Index of constants, variables and parameters

Table A.1 – Physical constants

Symbol	Name	Value	CGS units
G	Gravitational constant	6.6726×10^{-8}	$\text{cm}^3 \text{g}^{-1} \text{s}^{-2}$
c	Speed of light in a vacuum	2.9979×10^{10}	cm s^{-1}
k	Boltzmann constant	1.3807×10^{-16}	erg K^{-1}
m_p	Proton mass	1.6726×10^{-24}	g
σ	Stefan-Boltzmann constant	5.6705×10^{-5}	$\text{erg cm}^{-2} \text{K}^{-4} \text{s}^{-1}$
a	Radiation constant	7.5646×10^{-15}	$\text{erg cm}^{-3} \text{K}^{-4}$
M_\odot	Solar mass	1.99×10^{33}	g
		(↓ values for He)	
κ_0	Thomson scattering opacity	0.2	$\text{cm}^2 \text{g}^{-1}$
μ_1, μ_e, μ	Ion, electron, gas mean molecular weights	4, 2, 4/3	-

Table A.2 – Variables

Variable	Description	CGS units
r	Radial distance from stellar center	cm
$T(r)$	Local temperature	K
$\rho(r)$	Rest-mass density	g cm^{-3}
$u(r)$	Fluid velocity in radial direction	cm s^{-1}
$F(r)$	Local flux	$\text{erg s}^{-1} \text{ cm}^{-2}$
$L(r)$	Local luminosity	erg s^{-1}
$\kappa(T)$	Corrected electron scattering opacity	$\text{cm}^2 \text{ g}^{-1}$
$c_s(r, T)$	Sound speed	cm s^{-1}
$U_R(r, T)$	Radiation energy density	erg cm^{-3}
$P_g(\rho, T)$	Gas pressure	erg cm^{-3}
$U_g(\rho, T)$	Gas internal energy	erg cm^{-3}

Table A.3 – Parameters

Parameter	Name	Equation	CGS units
ζ	Curvature parameter	(2.1.3)	-
γ	Lorentz factor	(2.1.6)	-
Ψ	Energy parameter	(2.1.4)	-
L_{Edd}	Eddington luminosity	(1.4.1)	erg s ⁻¹
L_{cr}	Local critical luminosity	(1.4.2)	erg s ⁻¹
L^∞	Luminosity seen at infinity	(1.4.3)	erg s ⁻¹
g	Local gravitational acceleration	(3.2.8)	cm s ⁻²
ω_g	Rest-mass energy plus enthalpy	(2.2.2)	erg cm ⁻³
\dot{M}	Mass-loss rate	(2.3.7)	g s ⁻¹
\dot{E}	Energy-loss rate	(2.3.19)	erg s ⁻¹
r_c	Critical point radius	(3.1.1)	cm
r_{ph}	Photospheric radius	(3.2.5)*	cm
r_b	Wind/envelope base radius	(3.2.9)	cm
Φ	Velocity parameter	(3.1.2)	-
τ	Optical depth	(3.2.2)	-
τ^*	Optical depth parameter	(3.2.1)	-
y	Column depth	(3.2.6)	g cm ⁻²
∇_{rad}	Radiative gradient	(4.0.4)	-
∇_{ad}	Adiabatic gradient	(4.2.1)	-
T_{rad}	Radiation temperature	(5.2.1)	K
$\beta_{\text{I}}, \beta_{\text{e}}$ α_1, α_2, f	Pressure parameters	(2.4)	-
T^*			-
A_{e}, A	Paczynski and Proszynski [1986]	(2.5.10)	-
B_{e}, B	structure equations parameters	(2.5.12)	cm ² s ⁻²
C_{e}, C			cm ² s ⁻²

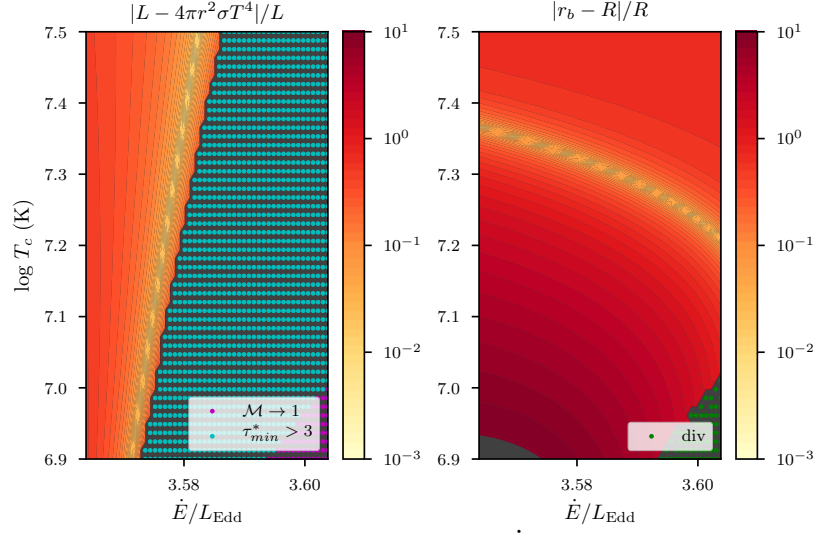
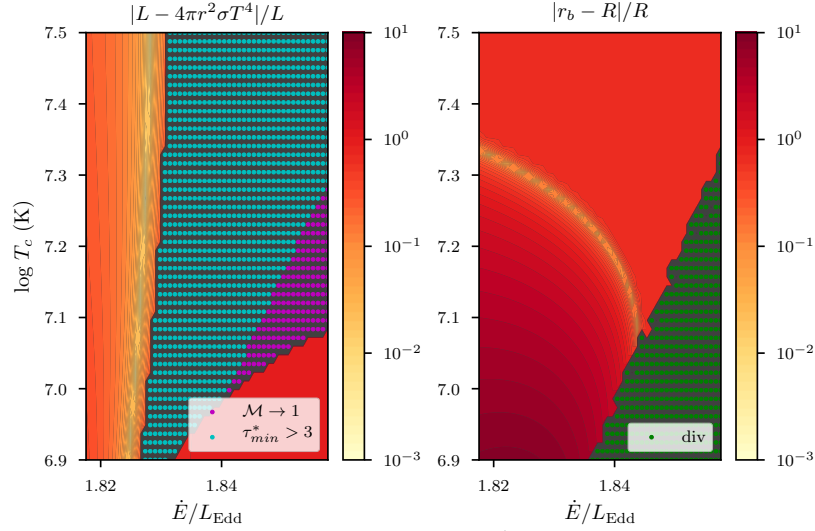
Appendix B

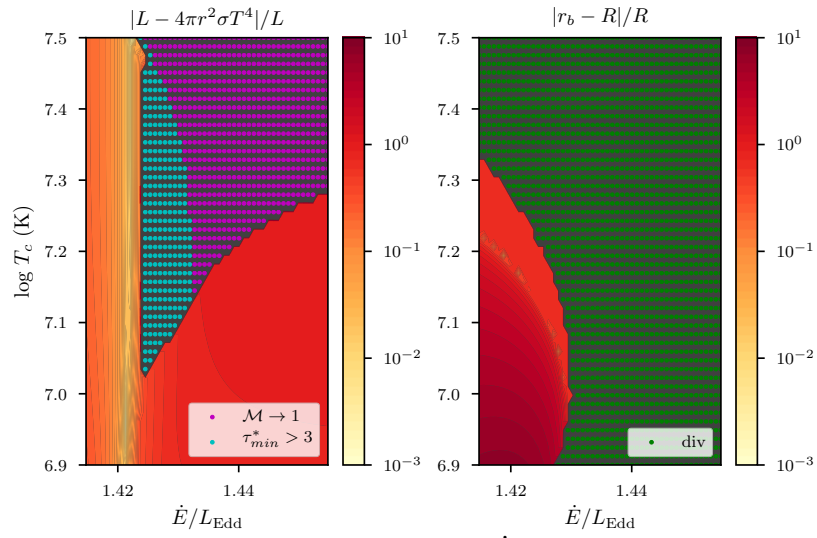
Wind parameter spaces

In Section 3.3, we showed the boundary condition errors on the (\dot{E}, T_c) parameter space for the $\dot{M} = 10^{18.5} \text{ g s}^{-1}$ wind. It is useful for potential future work to examine these parameter spaces at other values of the mass-loss rate.

Starting at 10^{18} g s^{-1} , we often encountered an interesting problem in the outer integration, represented by the purple dots in the figures below. Before approaching a photosphere, the velocity of the gas began decreasing and eventually approached the sound speed. This causes divergences in our equations, so we had to stop the integrations. Concurrent with the decreasing velocity, the density of the gas increased outward, indicating the formation of a shell. Investigating these solutions would require improvements in the model and more flexible boundary conditions. Most likely however, a proper analysis would involve time-dependent calculations.

In the inwards integration, we found that for large regions of the parameter space, shown by the green dots in the figures below, we could never hit the required column depth of 10^8 g cm^{-2} for the boundary condition, as the integration would strongly diverge at lower pressures. We were not able to find a physical explanation for these divergences.

Boundary condition errors on the $\log \dot{M} = 18$ parameter space.Boundary condition errors on the $\log \dot{M} = 17.5$ parameter space.



Boundary condition errors on the $\log \dot{M} = 17.2$ parameter space.

Appendix C

Analytical Newtonian envelopes

Paczynski and Anderson [1986] demonstrate a simple calculation for the most extended envelope in Newtonian gravity, one for which the luminosity ratio $\Gamma \equiv L/L_{\text{Edd}} = 1$. Here we extend this calculation to the general case $\Gamma \leq 1$.

With no general relativistic corrections, the hydrostatic balance and photon diffusion equations are simply written as

$$\frac{dP}{dr} = -\frac{GM\rho}{r^2} \quad (\text{C.0.1})$$

$$\frac{dP_R}{dr} = -\frac{\rho\kappa L}{4\pi r^2 c}, \quad (\text{C.0.2})$$

where $P_R = aT^4/3$ is the radiation pressure. This leads to

$$\frac{dP_R}{dP} = \frac{L}{L_{\text{cr}}} = \Gamma \frac{\kappa}{\kappa_0} = \Gamma \left[1 + \left(\frac{T}{T_0} \right)^\alpha \right]^{-1}, \quad (\text{C.0.3})$$

where $T_0 = 4.5 \times 10^8$ K and $\alpha = 0.86$ are from the opacity formula Eq. (1.4.4). We may re-write Eq. (C.0.3) as

$$dP = \frac{1}{\Gamma} \frac{4a}{3} \left[1 + \left(\frac{T}{T_0} \right)^\alpha \right] T^3 dT \quad (\text{C.0.4})$$

which we integrate from the photosphere r_{ph} where we assume $T \approx 0$ and

thus $P \approx 0$, giving the general expression

$$P(T) = \frac{1}{\Gamma} \frac{aT^4}{3} \left[1 + \frac{4}{4+\alpha} \left(\frac{T}{T_0} \right)^\alpha \right]. \quad (\text{C.0.5})$$

This also leads to an expression for the density, since $P_g = P - P_R = kT\rho/\mu m_p$, such that

$$\rho(T) = \frac{1}{\Gamma} \frac{\mu m_p}{k} \frac{aT^3}{3} \left[1 - \Gamma + \frac{4}{4+\alpha} \left(\frac{T}{T_0} \right)^\alpha \right] \quad (\text{C.0.6})$$

Putting this back into Eq. (C.0.2), we obtain a differential equation for T ,

$$\left[1 + \left(\frac{T}{T_0} \right)^\alpha \right] \left[1 - \Gamma + \frac{4}{4+\alpha} \left(\frac{T}{T_0} \right)^\alpha \right]^{-1} dT = -\frac{1}{4} \frac{\mu m_p}{k} \frac{GM}{r^2} dr. \quad (\text{C.0.7})$$

This can be integrated from the photosphere. The $\Gamma = 1$ case is straightforward and leads to the expression in Paczynski and Anderson [1986],

$$\frac{GM}{r} \frac{\mu m_p}{kT} \frac{1}{4+\alpha} \left(1 - \frac{r}{r_{\text{ph}}} \right) = 1 + \frac{1}{1-\alpha} \left(\frac{T_0}{T} \right)^\alpha. \quad (\text{C.0.8})$$

If $\Gamma < 1$, we instead have

$$\begin{aligned} & \frac{GM}{r} \frac{\mu m_p}{kT} \frac{1}{4+\alpha} \left(1 - \frac{r}{r_{\text{ph}}} \right) \\ &= 1 - \left(1 - \frac{4}{(4+\alpha)(1-\Gamma)} \right) {}_2F_1 \left(1, \frac{1}{\alpha}; 1 + \frac{1}{\alpha}; \frac{-4(T/T_0)^\alpha}{(4+\alpha)(1-\Gamma)} \right), \end{aligned} \quad (\text{C.0.9})$$

where ${}_2F_1$ is the hypergeometric function. All that is required to find r_{ph} for a given Γ is to have a known pair (r, T) somewhere in the envelope. For example, Paczynski and Anderson [1986] assumed a constant $T = 2 \times 10^9$ K at $r = R$. For consistency, we use our boundary condition $P = gy_b = 10^8 g$ at $r = R$, which we can easily solve for T since we have $\rho = \rho(T)$. This is how we computed the envelope models shown in Fig. 4.3.1.

Appendix D

Additional derivations

In Chapter 2, we presented the general approach to deriving equations of radiation hydrodynamics under the specific set of approximations relevant to this work. However, we left out most of the algebraic calculations for brevity. We write them down in this appendix for future reference, since many of these derivations are non-trivial. What follows is a combination and extended explanation of derivations done in these four papers: Park [1993], Park [2006], Thorne et al. [1981], Flammang [1982]. The notation for general relativity largely follows Carroll [2004].

GR essentials

We use the Schwarzschild metric,

$$ds^2 = g_{\mu\nu}dx^\mu dx^\nu = -\zeta^2 c^2 dt^2 + \zeta^{-2} dr^2 + r^2(d\theta^2 + \sin^2\theta d\phi^2), \quad (\text{D.0.1})$$

to describe the space-time $x^\mu = (ct, r, \theta, \phi)$ around a spherical and non-rotating central object. We define the neutron star mass parameter

$$m \equiv GM/c^2 \quad (\text{D.0.2})$$

to simplify the notation. The curvature parameter is $\zeta = (1 - 2m/r)^{1/2}$, which is equivalent to Eq. (2.1.3). The metric $g_{\mu\nu}$ and its inverse $g^{\mu\nu}$ can be used to lower and raise indices. For example, $v^\mu = g^{\mu\alpha}v_\alpha$ contains only one term since the metric has no off-diagonal terms (we use the usual Einstein summation convention where repeated top and bottom indices are summed over).

The four-velocity, defined as $U^\mu = dx^\mu/d\tau$, where τ is the proper time, has the normalization property $U_\mu U^\mu = -c^2$. For purely radial motion ($U^\theta = U^\phi = 0$), we have:

$$\begin{aligned}
 -c^2 &= U_t U^t + U_r U^r \\
 &= g_{t\alpha} U^\alpha U^t + g_{r\alpha} U^\alpha U^r \\
 &= -\zeta^2 (U^t)^2 + \zeta^{-2} (U^r)^2 \\
 \Rightarrow U^t &= \sqrt{c^2 \zeta^{-2} + \zeta^{-4} (U^r)^2} \\
 \Rightarrow U_t &= g_{t\alpha} U^\alpha = -\sqrt{c^2 \zeta^2 + (U^r)^2}
 \end{aligned} \tag{D.0.3}$$

We kept the positive root for U^t so that particles move forward in time ($dt/d\tau > 0$). The energy parameter of Eq. 2.1.4 is defined as $\Psi \equiv -U_t/c = \sqrt{\zeta^2 + (U^r/c)^2}$.

The non-zero Christoffel symbols of the Schwarzschild metric are:

$$\begin{aligned}
 \Gamma_{tt}^r &= m\zeta^2 r^{-2} & \Gamma_{rr}^r &= -m\zeta^{-2} r^{-2} & \Gamma_{tr}^t &= m\zeta^{-2} r^{-2} \\
 \Gamma_{\theta r}^\theta &= r^{-1} & \Gamma_{\phi r}^\phi &= r^{-1} & \Gamma_{\phi\theta}^\phi &= \cot \theta \\
 \Gamma_{\theta\theta}^r &= -r\zeta^2 & \Gamma_{\phi\phi}^r &= -r\zeta^2 \sin^2 \theta & \Gamma_{\phi\phi}^\theta &= -\sin \theta \cos \theta
 \end{aligned}$$

The usual symbols " , " and " ; " are used for regular and covariant derivatives respectively. The covariant derivative of an arbitrary tensor is given

by

$$\begin{aligned}
T^{\mu_1 \dots \mu_k}_{\nu_1 \dots \nu_l; \alpha} &= \partial_\alpha T^{\mu_1 \dots \mu_k}_{\nu_1 \dots \nu_l} \\
&+ \Gamma_{\alpha\sigma}^{\mu_1} T^{\sigma \dots \mu_k}_{\nu_1 \dots \nu_l} + \dots + \Gamma_{\alpha\sigma}^{\mu_k} T^{\mu_1 \dots \sigma}_{\nu_1 \dots \nu_l} \\
&- \Gamma_{\alpha\nu_1}^\sigma T^{\mu_1 \dots \mu_k}_{\sigma \dots \nu_l} - \dots - \Gamma_{\alpha\nu_k}^\sigma T^{\mu_1 \dots \mu_k}_{\nu_1 \dots \sigma}, \quad (D.0.4)
\end{aligned}$$

where $\partial_\alpha \equiv \partial/\partial x^\alpha$.

There are two fundamental principles in this tensor formalism that need to be respected. First, the continuity equation represents the conservation of particle proper number density (per unit volume), and is given by $(nU^\mu)_{;\mu} = 0$. Second, the divergence of the total stress tensor of the system $T_{\text{tot}}^{\mu\nu}$ has to be zero ($T_{\text{tot};\nu}^{\mu\nu} = 0$) so that there can be a solution to the Einstein field equations.

Fixed and comoving frames

We now give a more extensive explanation of the two frames introduced to describe the fluid and radiation quantities in Section 2.1.

For the **fixed frame**, we construct an orthonormal basis $e_{\hat{\mu}} = \partial/\partial x^{\hat{\mu}}$. This frame is locally inertial, so we can use the flat (Minkowski) metric $\eta_{\mu\nu}$ to manipulate vectors. In terms of the coordinate basis $\partial/\partial x^\mu$,

$$\frac{\partial}{\partial \hat{t}} = \frac{1}{\zeta} \frac{\partial}{\partial t}, \quad \frac{\partial}{\partial \hat{r}} = \zeta \frac{\partial}{\partial r}, \quad \frac{\partial}{\partial \hat{\theta}} = \frac{1}{r} \frac{\partial}{\partial \theta}, \quad \frac{\partial}{\partial \hat{\phi}} = \frac{1}{r \sin \theta} \frac{\partial}{\partial \phi}. \quad (D.0.5)$$

It is easy to verify that the base is indeed orthonormal, i.e., $e_{\hat{\mu}} \cdot e^{\hat{\nu}} = \delta_{\hat{\mu}}^{\hat{\nu}}$ ¹, the kronecker delta. An observer in this frame sees matter moving with proper

¹Use $e^{\hat{j}} = \eta^{\hat{j}\hat{k}} e_{\hat{k}}$ and $\partial_i \cdot \partial_j = g_{jk} \partial_i \cdot \partial^k = g_{jk} \delta_i^k$

velocity \mathbf{v} , which in one spatial dimension is given by

$$v^r = \frac{U^{\hat{r}}}{U^{\hat{t}}} = \frac{U_\alpha e_{\hat{r}}^\alpha}{-U_\alpha e_{\hat{t}}^\alpha} = \frac{U_r \zeta}{-U_t \zeta^{-1}} = \frac{U^r \zeta^{-1}}{\Psi \zeta^{-1}} = U^r \Psi^{-1}. \quad (\text{D.0.6})$$

The fluid velocity is $u \equiv v^r = U^r/\Psi$. Putting this back into the definition for the energy parameter, $\Psi = \sqrt{\zeta^2 + (u\Psi/c)^2}$ gives

$$\Psi = \zeta \left(1 - \frac{u^2}{c^2}\right)^{-1/2} = \zeta \gamma, \quad (\text{D.0.7})$$

where γ is the Lorentz factor.

The **comoving frame** moves with velocity u with respect to the fixed frame. A Lorentz transformation $\partial/\partial x_{\text{co}}^{\hat{\mu}} = \Lambda_{\hat{\mu}}^{\hat{\alpha}} \partial/\partial x^{\hat{\alpha}}$ is used to link the two. The 1-D picture is straightforward as we can use the classic Lorentz transformation from special relativity, where

$$c\hat{t} = \gamma (c\hat{t}_{\text{co}} + u\hat{r}_{\text{co}}/c) \quad , \quad \hat{r} = \gamma (\hat{r}_{\text{co}} + u\hat{t}_{\text{co}}) \quad , \quad (\text{D.0.8})$$

leading to

$$\Lambda_{\hat{\mu}}^{\hat{\alpha}} = \begin{bmatrix} \gamma & \gamma u/c \\ \gamma u/c & \gamma \end{bmatrix}. \quad (\text{D.0.9})$$

Using (D.0.5) and (D.0.9), we can write the comoving derivatives in terms of the coordinates:

$$\frac{\partial}{\partial(c\hat{t}_{\text{co}})} = \Lambda_{\hat{t}}^{\hat{\alpha}} \frac{\partial}{\partial x^{\hat{\alpha}}} = \Lambda_{\hat{t}}^{\hat{t}} \frac{\partial}{\partial(c\hat{t})} + \Lambda_{\hat{t}}^{\hat{r}} \frac{\partial}{\partial \hat{r}} = \frac{\gamma}{\zeta} \frac{\partial}{\partial(ct)} + \frac{u\Psi}{c} \frac{\partial}{\partial r}, \quad (\text{D.0.10})$$

$$\frac{\partial}{\partial \hat{r}_{\text{co}}} = \Lambda_{\hat{r}}^{\hat{\alpha}} \frac{\partial}{\partial x^{\hat{\alpha}}} = \Lambda_{\hat{r}}^{\hat{t}} \frac{\partial}{\partial(c\hat{t})} + \Lambda_{\hat{r}}^{\hat{r}} \frac{\partial}{\partial \hat{r}} = \frac{u\gamma}{c\zeta} \frac{\partial}{\partial(ct)} + \Psi \frac{\partial}{\partial r}.$$

There is no angular Lorentz boost, so $\partial/\partial \hat{\theta}_{\text{co}} = \partial/\partial \hat{\theta}$ and $\partial/\partial \hat{\phi}_{\text{co}} = \partial/\partial \hat{\phi}$. Obtaining the inverse transformations is just a matter of inverting $\Lambda_{\hat{\mu}}^{\hat{\alpha}}$.

Matter and Radiation stress-energy tensors

We showed in Section 2.2 the origin for the radiation stress-tensors,

$$\bar{\mathbf{R}} = \begin{bmatrix} \bar{E} & \bar{F}/c & 0 & 0 \\ \bar{F}/c & \bar{P} & 0 & 0 \\ 0 & 0 & (\bar{E} - \bar{P})/2 & 0 \\ 0 & 0 & 0 & (\bar{E} - \bar{P})/2 \end{bmatrix} \quad (\text{D.0.11})$$

$$\mathbf{R}_{\text{co}} = \begin{bmatrix} U_R & F/c & 0 & 0 \\ F/c & U_R/3 & 0 & 0 \\ 0 & 0 & U_R/3 & 0 \\ 0 & 0 & 0 & U_R/3 \end{bmatrix}. \quad (\text{D.0.12})$$

The two tensors are related to each other by the previously defined Lorentz boost $\Lambda_{\hat{\mu}}^{\hat{\alpha}}$. Indeed, the transformation rule for tensors is

$$\bar{R}^{\hat{\alpha}\hat{\beta}} = \frac{\partial x^{\hat{\alpha}}}{\partial x_{\text{co}}^{\hat{\mu}}} \frac{\partial x^{\hat{\beta}}}{\partial x_{\text{co}}^{\hat{\nu}}} R_{\text{co}}^{\hat{\mu}\hat{\nu}} = \Lambda_{\hat{\mu}}^{\hat{\alpha}} \Lambda_{\hat{\nu}}^{\hat{\beta}} R_{\text{co}}^{\hat{\mu}\hat{\nu}} \quad (\text{D.0.13})$$

In the four-dimensional picture, the Lorentz matrix is completed by 2x2 identity matrix in the (θ, ϕ) block, i.e., $\Lambda_{\hat{\theta}}^{\hat{\theta}} = \Lambda_{\hat{\phi}}^{\hat{\phi}} = 1$, $\Lambda_{\hat{\phi}}^{\hat{\theta}} = \Lambda_{\hat{\theta}}^{\hat{\phi}} = 0$. Using this, we can write the components of energy, flux and pressure in the fixed frame as a function of the comoving quantities:

$$\begin{aligned} \bar{E} = \bar{R}^{\hat{t}\hat{t}} &= \Lambda_{\hat{\mu}}^{\hat{t}} \Lambda_{\hat{\nu}}^{\hat{t}} R_{\text{co}}^{\hat{\mu}\hat{\nu}} \\ &= \Lambda_{\hat{t}}^{\hat{t}} (\Lambda_{\hat{t}}^{\hat{t}} R_{\text{co}}^{\hat{t}\hat{t}} + \Lambda_{\hat{r}}^{\hat{t}} R_{\text{co}}^{\hat{t}\hat{r}}) + \Lambda_{\hat{r}}^{\hat{t}} (\Lambda_{\hat{t}}^{\hat{t}} R_{\text{co}}^{\hat{r}\hat{t}} + \Lambda_{\hat{r}}^{\hat{t}} R_{\text{co}}^{\hat{r}\hat{r}}) \\ &= (\Lambda_{\hat{t}}^{\hat{t}})^2 R_{\text{co}}^{\hat{t}\hat{t}} + 2\Lambda_{\hat{t}}^{\hat{t}} \Lambda_{\hat{r}}^{\hat{t}} R_{\text{co}}^{\hat{t}\hat{r}} + (\Lambda_{\hat{r}}^{\hat{t}})^2 R_{\text{co}}^{\hat{r}\hat{r}} \\ &= \gamma^2 \left[\left(1 + \frac{1}{3} \frac{u^2}{c^2} \right) U_R + \frac{2u}{c^2} F \right], \end{aligned} \quad (\text{D.0.14})$$

$$\bar{F} = c\bar{R}^{\hat{t}\hat{r}} = \gamma^2 \left[\frac{4}{3} u U_R + \left(1 + \frac{u^2}{c^2} \right) F \right], \quad (\text{D.0.15})$$

$$\bar{P} = \bar{R}^{\hat{r}\hat{r}} = \gamma^2 \left[\left(\frac{u^2}{c^2} + \frac{1}{3} \right) U_R + \frac{2u}{c^2} F \right]. \quad (\text{D.0.16})$$

To find the radiation tensor in the coordinate basis, we can use the transformations given by Eq. (D.0.5) in

$$R^{\mu\nu} = \frac{\partial x^\mu}{\partial x^{\hat{\alpha}}} \frac{\partial x^\nu}{\partial x^{\hat{\beta}}} \bar{R}^{\hat{\alpha}\hat{\beta}}. \quad (\text{D.0.17})$$

Since the transformation has no off-diagonal terms, we easily get

$$R^{\mu\nu} = \begin{bmatrix} \zeta^{-2} \bar{E} & \bar{F}/c & 0 & 0 \\ \bar{F}/c & \zeta^2 \bar{P} & 0 & 0 \\ 0 & 0 & r^{-2}(\bar{E} - \bar{P})/2 & 0 \\ 0 & 0 & 0 & (r \sin \theta)^{-2}(\bar{E} - \bar{P})/2 \end{bmatrix}. \quad (\text{D.0.18})$$

We also introduced the radiation four-force density tensor G^α , and specified it in terms of the local and cooling functions and the opacity in the comoving frame (Eq. 2.2.21-2.2.22). We will need its components in the coordinate frame when deriving the hydrodynamics and radiation equations. With

$$G^\alpha = \frac{\partial x^\alpha}{\partial x_{\text{co}}^{\hat{\beta}}} G_{\text{co}}^{\hat{\beta}} \quad (\text{D.0.19})$$

and the transformation given by Eq. (D.0.10), we obtain

$$G^t = \frac{\gamma}{\zeta} \left(G_{\text{co}}^t + \frac{u}{c} G_{\text{co}}^{\hat{r}} \right), \quad (\text{D.0.20})$$

$$G^r = \Psi \left(\frac{u}{c} G_{\text{co}}^t + G_{\text{co}}^{\hat{r}} \right). \quad (\text{D.0.21})$$

We have made the assumption of a purely radial flux here, i.e., the angular components of F_{co}^i , and as a result those of G_{co}^i and G^i , are all zero.

Continuity equation

The general relativistic mass conservation equation comes from the covariant continuity equation. Considering spherical symmetry ($U^\theta = U^\phi = 0$),

$$\begin{aligned}
0 &= (nU^\mu)_{;\mu} \\
&= \partial_t(nU^t) + \partial_r(nU^r) + n(\Gamma_{t\alpha}^t U^\alpha + \Gamma_{r\alpha}^r U^\alpha + \Gamma_{\theta\alpha}^\theta U^\alpha + \Gamma_{\phi\alpha}^\phi U^\alpha) \\
&= \partial_t(n\zeta^{-2}\Psi c) + \partial_r(nu\Psi) + \frac{2}{r}nu\Psi \\
\Rightarrow 0 &= \frac{1}{\zeta^2} \frac{\partial}{\partial t} (n\Psi) + \frac{1}{r^2} \frac{\partial}{\partial r} (r^2 nu\Psi)
\end{aligned} \tag{D.0.22}$$

We used $U^t = g^{t\alpha}U_\alpha = \zeta^{-2}\Psi c$, $U^r = u\Psi$ and $\partial_t = \partial/\partial(ct)$. This is the same as Eq. (2.3.2), in units of number density per unit time [$\text{cm}^{-3} \text{ s}^{-1}$].

Momentum equation

Our general relativistic formulation of the Euler equation that describes the balance of forces and momenta in the system, including radiation, comes from $T^{\mu\nu}_{;\nu} = G^\mu$, to which we apply the projection operator

$$P_\alpha{}^\beta = \delta_\alpha^\beta + \frac{U_\alpha U^\beta}{c^2}, \tag{D.0.23}$$

so that the equation to write down is $P_\alpha{}^\beta T^{\alpha\lambda}_{;\lambda} = P_\alpha{}^\beta G^\alpha = G^\beta + U_\alpha U^\beta G^\alpha / c^2$. Before expanding, let us note three important identities:

1. $g^{\mu\nu}_{;\lambda} = g_{\mu\nu;\lambda} = 0$, by definition of the Christoffel symbols.
2. $\delta^\nu_{\mu;\lambda} = (g_{\mu\alpha} g^{\alpha\nu})_{;\lambda} = 0$. This allows us to use the kronecker delta in this useful way:

$$\delta^\nu_{\mu;\lambda} w^\mu = (\delta^\nu_{\mu} w^\mu)_{;\lambda} - \delta^\nu_{\mu;\lambda} w^\mu = w^\nu_{;\lambda}$$

3. $U_\mu U^\mu_{;\lambda} = 0$. We can prove this using the property $U_\mu U^\mu = -c^2$:

$$\begin{aligned}
0 &= (U_\mu U^\mu)_{;\lambda} \\
&= U_{\mu;\lambda} U^\mu + U_\mu U^\mu_{;\lambda} \\
&= (g_{\mu\alpha} U^\alpha)_{;\lambda} g^{\mu\beta} U_\beta + U_\mu U^\mu_{;\lambda} \\
&= \delta^\beta_\alpha U^\alpha_{;\lambda} U_\beta + U_\mu U^\mu_{;\lambda} \quad \text{using the first identity} \\
&= U^\beta_{;\lambda} U_\beta + U_\mu U^\mu_{;\lambda} \quad \text{using the second identity} \\
&= 2U_\mu U^\mu_{;\lambda} \\
\Rightarrow U_\mu U^\mu_{;\lambda} &= \frac{1}{2}(U_\mu U^\mu)_{;\lambda} = 0 \quad \blacksquare
\end{aligned}$$

With these simplifications, the following derivation is straightforward:

$$\begin{aligned}
P_\alpha{}^\beta T^{\alpha\lambda}_{;\lambda} &= c^{-2} [\delta^\beta_\alpha + c^{-2} U_\alpha U^\beta] \\
&\quad [\omega_{g,\lambda} U^\alpha U^\lambda + \omega_g U^\alpha_{;\lambda} U^\lambda + \omega_g U^\alpha U^\lambda_{;\lambda} + c^2 P_{g,\lambda} g^{\alpha\lambda}] \\
&= c^{-2} (\omega_{g,\lambda} U^\beta U^\lambda + \omega_g U^\beta_{;\lambda} U^\lambda + \omega_g U^\beta U^\lambda_{;\lambda}) + P_{g,\lambda} g^{\beta\lambda} \\
&\quad - c^{-2} (\omega_{g,\lambda} U^\beta U^\lambda + \omega_g U^\beta U^\lambda_{;\lambda}) + c^{-2} P_{g,\lambda} U^\lambda U^\beta \\
&= c^{-2} \omega_g U^\beta_{;\lambda} U^\lambda + (g^{\beta\lambda} + c^{-2} U^\lambda U^\beta) P_{g,\lambda} \quad (\text{D.0.24})
\end{aligned}$$

Multiplying both sides by c^2 , the Euler equation is then

$$\omega_g U^\beta_{;\lambda} U^\lambda + (c^2 g^{\beta\lambda} + U^\lambda U^\beta) P_{g,\lambda} = c^2 G^\beta + U_\alpha U^\beta G^\alpha. \quad (\text{D.0.25})$$

The radial equation is obtained by fixing $\beta = r$, that is

$$\begin{aligned}
\omega_g U^r_{;\lambda} U^\lambda + (c^2 g^{r\lambda} + U^\lambda U^r) P_{g,\lambda} &= c^2 G^r + U_\alpha U^r G^\alpha \\
&= G^r (c^2 + \zeta^{-2} (U^r)^2) - c \Psi U^r G^t. \quad (\text{D.0.26})
\end{aligned}$$

Expanding the left-hand side:

$$\begin{aligned}
& \omega_g(\partial_t U^r + \Gamma_{t\sigma}^r U^\sigma)U^t + \omega_g(\partial_r U^r + \Gamma_{r\sigma}^r U^\sigma)U^r \\
& \quad + U^r U^t \partial_t P_g + (c^2 c g^{rr} + (U^r)^2) \partial_r P_g \\
& = \omega_g(U^t \partial_t U^r + U^r \partial_r U^r + m r^{-2}(\zeta^2 (U^t)^2 - \zeta^{-2} (U^r)^2)) \\
& \quad + U^r U^t \partial_t P_g + c^2 \Psi^2 \partial_r P_g \\
& = \omega_g \left(\frac{\Psi}{\zeta^2} \frac{\partial}{\partial t} (u\Psi) + u\Psi \frac{\partial}{\partial r} (u\Psi) + m r^{-2} (c^2 \gamma^2 - u^2 \gamma^2) \right) \\
& \quad + \frac{u\Psi^2}{\zeta^2} \frac{\partial P_g}{\partial t} + c^2 \Psi^2 \frac{\partial P_g}{\partial r} \\
& = \omega_g \left(\frac{\Psi}{\zeta^2} \frac{\partial}{\partial t} (u\Psi) + \frac{1}{2} \frac{\partial}{\partial r} (u\Psi)^2 + \frac{mc^2}{r^2} \right) + u\gamma^2 \frac{\partial P_g}{\partial t} + c^2 \Psi^2 \frac{\partial P_g}{\partial r}
\end{aligned}$$

Expanding the right-hand side:

$$\begin{aligned}
G^r(c^2 + \zeta^{-2}(U^r)^2) - c\Psi U^r G^t & = \Psi \left(\frac{u}{c} G_{\text{co}}^t + G_{\text{co}}^{\hat{r}} \right) (c^2 + u^2 \gamma^2) \\
& \quad - u c \Psi^2 \frac{\gamma}{\zeta} \left(G_{\text{co}}^t + \frac{u}{c} G_{\text{co}}^{\hat{r}} \right) \\
& = c^2 \Psi G_{\text{co}}^{\hat{r}} = c\Psi \rho \kappa F
\end{aligned}$$

In the last line, we used our definitions $\kappa \equiv \bar{\chi}_{\text{co}}/\rho$ and $F \equiv F_{\text{co}}^r$. Dividing both sides by ω_g , the momentum equation (Eq. 2.3.3),

$$\frac{\Psi}{\zeta^2} \frac{\partial}{\partial t} (u\Psi) + \frac{1}{2} \frac{\partial}{\partial r} (u\Psi)^2 + \frac{GM}{r^2} + \frac{u\gamma^2}{\omega_g} \frac{\partial P_g}{\partial t} + \frac{c^2 \Psi^2}{\omega_g} \frac{\partial P_g}{\partial r} = \frac{\Psi c}{\omega_g} \rho \kappa F, \quad (\text{D.0.27})$$

has units of acceleration $[\text{cm s}^{-2}]$.

Energy equation

For the energy equation, we project using the velocity, $U_\alpha T^{\alpha\beta}_{;\beta} = U_\alpha G^\alpha$.

Left-hand side:

$$\begin{aligned}
U_\alpha T^{\alpha\beta}_{;\beta} &= c^{-2} U_\alpha (\omega_{g,\beta} U^\alpha U^\beta + \omega_g U^\alpha_{;\beta} U^\beta + \omega_g U^\alpha U^\beta_{;\beta} + c^2 P_{g,\beta} g^{\alpha\beta}) \\
&= -\omega_{g,\beta} U^\beta - \omega_g U^\beta_{;\beta} + P_{g,\beta} U^\beta \\
&= -(\omega_g U^\beta)_{;\beta} + P_{g,\beta} U^\beta \\
&= -\left(\frac{\omega_g}{n} n U^\beta\right)_{;\beta} + P_{g,\beta} U^\beta \\
&= -\left(\frac{\omega_g}{n}\right)_{;\beta} n U^\beta + P_{g,\beta} U^\beta \quad (\text{using the continuity equation}) \\
&= -\frac{n\Psi}{\zeta^2} \frac{\partial}{\partial t} \left(\frac{\omega_g}{n}\right) - nu\Psi \frac{\partial}{\partial r} \left(\frac{\omega_g}{n}\right) + \frac{\Psi}{\zeta^2} \frac{\partial P_g}{\partial t} + u\Psi \frac{\partial P_g}{\partial r}
\end{aligned}$$

Right-hand side:

$$\begin{aligned}
U_\alpha G^\alpha &= -c\Psi G^t + \frac{u\Psi}{\zeta^2} G^r \\
&= -c\gamma^2 \left(G_{\text{co}}^{\hat{t}} + \frac{u}{c} G_{\text{co}}^{\hat{r}}\right) + u\gamma^2 \left(\frac{u}{c} G_{\text{co}}^{\hat{t}} + G_{\text{co}}^{\hat{r}}\right) = -cG_{\text{co}}^{\hat{t}}
\end{aligned}$$

Multiplying both sides by -1 gives the energy equation (Eq. 2.3.4),

$$\frac{n\Psi}{\zeta^2} \frac{\partial}{\partial t} \left(\frac{\omega_g}{n}\right) + nu\Psi \frac{\partial}{\partial r} \left(\frac{\omega_g}{n}\right) - \frac{\Psi}{\zeta^2} \frac{\partial P_g}{\partial t} - u\Psi \frac{\partial P_g}{\partial r} = \Gamma_{\text{co}} - \Lambda_{\text{co}}, \quad (\text{D.0.28})$$

in units of energy density per unit time [$\text{erg cm}^{-3} \text{ s}^{-1}$].

We may re-write this equation in more intuitive ways. We replace n by ρ and remove a term in the derivative of ω_g since $\omega_g/\rho = c^2 + (P_g + U_g)/c^2$. Then,

$$\frac{\Psi}{\zeta^2} \left(\rho \frac{\partial}{\partial t} \left(\frac{\omega_g}{\rho} \right) - \frac{\partial P_g}{\partial t} \right) = \frac{\Psi}{\zeta^2} \frac{\partial U_g}{\partial t} + \frac{U_g + P_g}{\rho} \left(\frac{\rho}{\zeta^2} \frac{\partial \Psi}{\partial t} + \frac{1}{r^2} \frac{\partial}{\partial r} (r^2 \rho u \Psi) \right),$$

and

$$u\Psi \left(\rho \frac{\partial}{\partial r} \left(\frac{\omega_g}{\rho} \right) - \frac{\partial P_g}{\partial r} \right) = u\Psi \left(\frac{\partial U_g}{\partial r} - \frac{U_g + P_g}{\rho} \frac{\partial \rho}{\partial r} \right),$$

so that we end up with

$$\frac{\Psi}{\zeta^2} \frac{\partial U_g}{\partial t} + \frac{U_g + P_g}{\zeta^2} \frac{\partial \Psi}{\partial t} + u\Psi \frac{\partial U_g}{\partial r} + \frac{U_g + P_g}{r^2} \frac{\partial}{\partial r} (r^2 u\Psi) = \Gamma_{\text{co}} - \Lambda_{\text{co}} \quad (\text{D.0.29})$$

We can also write this in terms of the specific internal energy $\varepsilon_g \equiv U_g/\rho$.

This gives

$$\frac{\Psi}{\zeta^2} \frac{\partial \varepsilon_g}{\partial t} + u\Psi \frac{\partial \varepsilon_g}{\partial r} + \frac{P_g}{\rho \zeta^2} \frac{\partial \Psi}{\partial t} + \frac{P_g}{\rho r^2} \frac{\partial}{\partial r} (r^2 u\Psi) = \frac{\Gamma_{\text{co}} - \Lambda_{\text{co}}}{\rho}. \quad (\text{D.0.30})$$

It could be argued that the $\partial \Psi / \partial t$ term can be ignored. Then, with only one time derivative, this equation would be very suitable for a hydrodynamics calculation.

Radiation moment equations

The radiation equations are $R^{\alpha\beta}_{;\beta} = -G^\alpha$. The moment equation is $\alpha = t$.

Left-hand side:

$$\begin{aligned} R^{t\beta}_{;\beta} &= \partial_\beta R^{t\beta} + \Gamma_{\beta\sigma}^t R^{\sigma\beta} + \Gamma_{\beta\sigma}^\beta R^{t\sigma} \\ &= \partial_\beta R^{t\beta} + (3\Gamma_{tr}^t + \Gamma_{rr}^r + \Gamma_{\theta r}^\theta + \Gamma_{\phi r}^\phi) R^{tr} \\ &= \partial_t R^{tt} + \partial_r R^{tr} + \left(\frac{2m}{r^2 \zeta^2} + \frac{2}{r} \right) R^{tr} \\ &= \frac{\partial R^{tt}}{\partial(ct)} + \frac{1}{r^2 \zeta^2} \frac{\partial}{\partial r} (r^2 \zeta^2 R^{tr}) \\ &= \frac{1}{c \zeta^2} \frac{\partial \bar{E}}{\partial t} + \frac{1}{c r^2 \zeta^2} \frac{\partial}{\partial r} (r^2 \zeta^2 \bar{F}) \end{aligned}$$

Multiplying both sides by c gives the radiation energy balance equation (Eq. 2.3.5),

$$\frac{1}{\zeta^2} \frac{\partial \bar{E}}{\partial t} + \frac{1}{\zeta^2 r^2} \frac{\partial}{\partial r} (r^2 \zeta^2 \bar{F}) = \frac{\gamma}{\zeta} \left(\Lambda_{\text{co}} - \Gamma_{\text{co}} - \frac{u}{c} \rho \kappa F \right) \quad (\text{D.0.31})$$

in units of energy density per unit time [erg cm⁻³ s⁻¹].

The first moment equation is $\alpha = r$.

Left-hand side:

$$\begin{aligned} R^{r\beta}{}_{;\beta} &= \partial_\beta R^{r\beta} + \Gamma_{\beta\sigma}^r R^{\sigma\beta} + \Gamma_{\beta\sigma}^\beta R^{r\sigma} \\ &= \partial_\beta R^{r\beta} + \Gamma_{tt}^r R^{tt} + (2\Gamma_{rr}^r + \Gamma_{tr}^t + \Gamma_{\theta r}^\theta + \Gamma_{\phi r}^\phi) R^{rr} + \Gamma_{\theta\theta}^r R^{\theta\theta} + \Gamma_{\phi\phi}^r R^{\phi\phi} \\ &= \partial_t R^{rt} + \partial_r R^{rr} + \frac{m}{r^2} \zeta^2 R^{tt} + \left(\frac{2}{r} - \frac{m}{r^2 \zeta^2} \right) R^{rr} - r \zeta^2 (R^{\theta\theta} + \sin^2 \theta R^{\phi\phi}) \\ &= \frac{1}{c^2} \frac{\partial \bar{F}}{\partial t} + \frac{\partial}{\partial r} (\zeta^2 \bar{P}) + \frac{m}{r^2} \bar{E} + \left(\frac{2\zeta^2}{r} - \frac{m}{r^2} \right) \bar{P} - \frac{\zeta^2}{r} (\bar{E} - \bar{P}) \\ &= \frac{1}{c^2} \frac{\partial \bar{F}}{\partial t} + \zeta^2 \frac{\partial \bar{P}}{\partial r} + \frac{m}{r^2} (\bar{E} + \bar{P}) + \frac{\zeta^2}{r} (3\bar{P} - \bar{E}) \end{aligned}$$

Multiplying both sides by c^2 gives the radiation force balance equation (Eq. 2.3.6),

$$\frac{\partial \bar{F}}{\partial t} + c^2 \zeta^2 \frac{\partial \bar{P}}{\partial r} + \frac{GM}{r^2} (\bar{E} + \bar{P}) + \frac{c^2 \zeta^2}{r} (3\bar{P} - \bar{E}) = u \Psi (\Lambda_{\text{co}} - \Gamma_{\text{co}}) - \Psi c \rho \kappa F, \quad (\text{D.0.32})$$

in units of energy flux per unit time [erg cm⁻² s⁻²].

Non-relativistic limit

Let us now convince the reader that the hydrodynamics equations that we derived from first principles, i.e., $(nU^\mu)_{;\mu} = 0$ and $T_{\text{tot};\nu}^{\mu\nu} = 0$, converge to familiar textbook equations in the non-relativistic limit. In this limit, we take $\zeta = \gamma = \Psi = 1$ and $P_g \ll \rho c^2$. For familiarity, we restore the ∇

operators for gradients and divergences and \mathbf{u} and \mathbf{F} as vectors. For radiation, there is no frame transformation so that the fixed frame quantities are equal to their comoving frame counterpart ($\bar{E} = U_R$, $\bar{F} = F$, $\bar{P} = U_R/3$, $\Lambda_{\text{co}} - \Gamma_{\text{co}} = \Lambda - \Gamma$). We can also freely replace n with ρ in all of the equations.

The conservation of mass equation trivially becomes

$$\frac{\partial \rho}{\partial t} + \nabla \cdot (\rho \mathbf{u}) = 0. \quad (\text{D.0.33})$$

For the conservation of momentum, we can easily neglect the $\partial P_g / \partial t$ term since it is smaller than the rest by a factor c^2 . With the gravitationnal acceleration \mathbf{g} ,

$$\frac{\partial \mathbf{u}}{\partial t} + (\mathbf{u} \cdot \nabla) \mathbf{u} = -\frac{\nabla P_g}{\rho} + \mathbf{g} + \frac{\kappa \mathbf{F}}{c} \quad (\text{D.0.34})$$

For the energy equation, we take the one written in terms of the specific internal energy ε_g , Eq. (D.0.30), which straightforwardly becomes

$$\frac{\partial \varepsilon}{\partial t} + \mathbf{u} \cdot \nabla \varepsilon = -\frac{P_g}{\rho} \nabla \cdot \mathbf{u} + \frac{\Lambda - \Gamma}{\rho} \quad (\text{D.0.35})$$

For the radiation moment equations, we only have to note that $3\bar{P} - \bar{E} = 0$ because there is no frame transformation. We obtain

$$\frac{\partial U_R}{\partial t} + \nabla \cdot \mathbf{F} = \Lambda - \Gamma - \frac{u}{c} \rho \kappa |\mathbf{F}|, \quad (\text{D.0.36})$$

$$\frac{\partial \mathbf{F}}{\partial t} + c^2 \nabla \left(\frac{U_R}{3} \right) = \mathbf{u}(\Lambda - \Gamma) - \frac{4U_R}{3} \mathbf{a} - \rho \kappa c \mathbf{F}. \quad (\text{D.0.37})$$

Bibliography

- B. P. Abbott, others (LIGO Scientific Collaboration, and Virgo Collaboration). GW170817: Observation of Gravitational Waves from a Binary Neutron Star Inspiral. *Physical Review Letters*, 119(16):161101, 2017.
- J. R. Buchler and W. R. Yueh. Compton scattering opacities in a partially degenerate electron plasma at high temperatures. *The Astrophysical Journal*, 210:440–446, 1976.
- Sean M. Carroll. *Spacetime and geometry. An introduction to general relativity*. 2004.
- Andrew Cumming and Jared Macbeth. The Thermal Evolution following a Superburst on an Accreting Neutron Star. *The Astrophysical Journal Letters*, 603(1):L37–L40, 2004.
- Andrew Cumming, Jared Macbeth, J J M Zand, and Dany Page. Long Type I X-ray bursts and neutron star interior physics. *The Astrophysical Journal*, 646:429–451, 2006.
- Toshikazu Ebisuzaki, Tomoyuki Hanawa, and Daiichirio Sugimoto. Mass loss from neutron stars associated with X-ray bursts. *Publications of the Astronomical Society of Japan*, 35:17–32, 1983.
- Richard A. Flammang. Stationary spherical accretion into black holes - II. Theory of optically thick accretion. *Monthly Notices of the Royal Astronomical Society*, 199:833–867, 1982.

- Duncan K. Galloway and Laurens Keek. Thermonuclear X-ray bursts. art. arXiv:1712.06227, 2017.
- Duncan K. Galloway, Michael P. Muno, Jacob M. Hartman, Dimitrios Psaltis, and Deepto Chakrabarty. *Thermonuclear (type-I) X-ray bursts observed by the Rossi X-ray Timing Explorer*, volume 179. 2008.
- Keith Gendreau and Zaven Arzoumanian. Searching for a pulse. *Nature Astronomy*, 1:895, 2017.
- J.E. Grindlay, H. Gursky, H. Schnopper, D.R. Parsignault, J. Heise, A.C. Brinkman, and J. Schrijver. Discovery of intense X-ray bursts from the globular cluster NGC 6624. *The Astrophysical Journal*, 205:L127–L130, 1976.
- Carl J. Hansen and Steven D. Kawaler. *Stellar Interiors. Physical Principles, Structure, and Evolution*. 1994. doi: 10.1007/978-1-4419-9110-2.
- Yago Herrera, Gloria Sala, and Jordi José. Simulations of stellar winds from X-ray bursts. Characterization of solutions and observable variables. *Astronomy & Astrophysics*, 638:A107, 2020.
- A. Hewish, S. J. Bell, J. D H Pilkington, P. F. Scott, and R. A. Collins. Observation of a rapidly pulsating radio source. *Nature*, 217(5130):709–713, 1968.
- J. J. M. in ’t Zand and N. N. Weinberg. Evidence of heavy-element ashes in thermonuclear X-ray bursts with photospheric superexpansion. *Astronomy & Astrophysics*, 520:A81, 2010.
- P. C. Joss, E. E. Salpeter, and J. P. Ostriker. On the “Critical Luminosity” in Stellar Interiors and Stellar Surface Boundary Conditions. *The Astrophysical Journal*, 181:429–438, 1973.

- Paul C. Joss and Fulvio Melia. Quasi-static winds from neutron stars. *The Astrophysical Journal*, 312:700, 1987.
- J. J. E. Kajava, J. Nättilä, J. Poutanen, A. Cumming, V. Suleimanov, and E. Kuulkers. Detection of burning ashes from thermonuclear X-ray bursts. *Monthly Notices of the Royal Astronomical Society*, 464(1):L6–L10, 2017.
- Mariko Kato. Optically Thick Winds and Nova Outbursts. *Publ. Astron. Soc. Japan*, 35:507–519, 1983a.
- Mariko Kato. Neutron Star Wind. *Publications of the Astronomical Society of Japan*, 35(1):33–46, 1983b.
- L. Keek, Z. Arzoumanian, D. Chakrabarty, J. Chenevez, K. C. Gendreau, S. Guillot, T. Güver, J. Homan, G. K. Jaisawal, B. LaMarr, F. K. Lamb, S. Mahmoodifar, C. B. Markwardt, T. Okajima, T. E. Strohmayer, and J. J. M. in ’t Zand. NICER Detection of Strong Photospheric Expansion during a Thermonuclear X-Ray Burst from 4U 1820-30. *The Astrophysical Journal Letters*, 856(2):L37, 2018.
- E. Kuulkers, P. R. den Hartog, J. J. M. in’t Zand, F. W. M. Verbunt, W. E. Harris, and M. Cocchi. Photospheric radius expansion X-ray bursts as standard candles. *Astronomy & Astrophysics*, 399:663–680, 2003.
- Walter H. G. Lewin and Michiel van der Klis. *Compact Stellar X-ray Sources*, volume 39. 2006.
- Walter H. G. Lewin, Jan van Paradijs, and Ronald E. Taam. X-Ray Bursts. *Space Science Reviews*, 62(3-4):223–389, 1993.
- D. Mihalas and B. W. Mihalas. *Foundations of radiation hydrodynamics*. 1984.
- Dimitri Mihalas. *Stellar atmospheres*. 1978.

- M. C. Miller, F. K. Lamb, A. J. Dittmann, S. Bogdanov, Z. Arzoumanian, K. C. Gendreau, S. Guillot, A. K. Harding, W. C. G. Ho, J. M. Lattimer, R. M. Ludlam, S. Mahmoodifar, S. M. Morsink, P. S. Ray, T. E. Strohmayer, K. S. Wood, T. Enoto, R. Foster, T. Okajima, G. Prigozhin, and Y. Soong. PSR J0030+0451 Mass and Radius from NICER Data and Implications for the Properties of Neutron Star Matter. 887(1):L24, 2019.
- Luciano Nobili, Roberto Turolla, and Iosif Lapidus. Winds from Neutron Stars and Strong Type I X-Ray Bursts. *The Astrophysical Journal*, 433: 276, 1994.
- Feryal Özel and Paulo Freire. Masses, Radii, and the Equation of State of Neutron Stars. *Annual Review of Astronomy & Astrophysics*, 54(1): 401–440, 2016.
- Bohdan Paczynski. Models of X-ray bursters with radius expansion. *The Astrophysical Journal*, 267:315–321, 1983.
- Bohdan Paczynski and Nels Anderson. Models of extended relativistic envelopes of neutron stars. *The Astrophysical Journal*, 302:1–10, 1986.
- Bohdan Paczynski and M. Proszynski. Models of radiation-driven winds from general relativistic neutron stars. *The Astrophysical Journal*, 302:519–529, 1986.
- Myeong G. Park. Relativistic theory of radiative transfer: time-dependent radiation moment equations. *Astronomy & Astrophysics*, 274:642–646, 1993.
- Myeong G. Park. Equations of general relativistic radiation hydrodynamics from a tensor formalism. *Monthly Notices of the Royal Astronomical Society*, 367:1739–1745, 2006.
- E. Parker. Dynamics of the interplanetary gas and magnetic fields. *ApJ*, 128: 664, 1958.

- Eliot Quataert, Rodrigo Fernandez, Daniel Kasen, Hannah Klion, and Bill Paxton. Super-Eddington stellar winds driven by near-surface energy deposition. *Monthly Notices of the Royal Astronomical Society*, 458:1214–1233, 2016.
- Thomas Quinn and Bohdan Paczynski. Stellar winds driven by super-Eddington luminosities. *The Astrophysical Journal*, 289:634–643, 1985.
- Hendrik Schatz, Lars Bildsten, Andrew Cumming, and Michael Wiescher. The Rapid Proton Process Ashes from Stable Nuclear Burning on an Accreting Neutron Star. *The Astrophysical Journal*, 524(2):1014–1029, 1999.
- I.S Shklovsky. On the nature of the source of x-ray emission of SCO XR-1. *The Astrophysical Journal*, 148:1–4, 1967.
- Andrew W. Steiner, James M. Lattimer, and Edward F. Brown. The Equation of State from Observed Masses and Radii of Neutron Stars. *The Astrophysical Journal*, 722:33–54, 2010.
- T. E. Strohmayer, D. Altamirano, Z. Arzoumanian, P. M. Bult, D. Chakrabarty, J. Chenevez, A. C. Fabian, K. C. Gendreau, S. Guillot, J. J. M. in 't Zand, G. K. Jaisawal, L. Keek, P. Kosec, R. M. Ludlam, S. Mahmoodifar, Christian Malacaria, and J. M. Miller. NICER Discovers Spectral Lines during Photospheric Radius Expansion Bursts from 4U 1820-30: Evidence for Burst-driven Winds. *The Astrophysical Journal Letters*, 878:L27, 2019.
- Kip S. Thorne, Richard A. Flammang, and Anna N. Zytkow. Stationary spherical accretion into black holes - I. Equations of structure. *Monthly Notices of the Royal Astronomical Society*, 194:475–484, 1981.
- Pauli Virtanen, Ralf Gommers, Travis E. Oliphant, Matt Haberland, Tyler Reddy, David Cournapeau, Evgeni Burovski, Pearu Peterson, Warren Weckesser, Jonathan Bright, Stéfan J. van der Walt, Matthew Brett,

- Joshua Wilson, K. Jarrod Millman, Nikolay Mayorov, Andrew R. J. Nelson, Eric Jones, Robert Kern, Eric Larson, CJ Carey, İlhan Polat, Yu Feng, Eric W. Moore, Jake VanderPlas, Denis Laxalde, Josef Perktold, Robert Cimrman, Ian Henriksen, E. A. Quintero, Charles R. Harris, Anne M. Archibald, Antônio H. Ribeiro, Fabian Pedregosa, Paul van Mulbregt, and SciPy 1.0 Contributors. SciPy 1.0: Fundamental Algorithms for Scientific Computing in Python. *Nature Methods*, 17:261–272, 2020.
- Hang Yu and Nevin N. Weinberg. Super-Eddington Winds from Type I X-Ray Bursts. *The Astrophysical Journal*, 863:53, 2018.
- Anna N. Zytkov. On the Stationary Mass Outflow from Stars I. The Computational Method and the Results for 1 Msun Star. *Acta Astronomica*, 22:103–139, 1972.